Influence of Landscape Weathering and Fire on Soil Contaminant Reactivity in Western Oregon

by

Chelsea Sabrina Obeidy

A dissertation accepted and approved in partial fulfillment of the

requirements for the degree of

Doctor of Philosophy

in Earth Sciences

Dissertation Committee:

Dr. Matthew Polizzotto, Advisor and Chair

Dr. Qusheng Jin, Core Member

Dr. Joshua Roering, Core Member

Dr. Sarah Cooley, Institutional Representative

University of Oregon

Spring 2024

© 2024 CHELSEA SABRINA OBEIDY

This work is licensed under CC BY-NC-ND 4.0

DISSERTATION ABSTRACT

Chelsea Sabrina Obeidy

Doctor of Philosophy in Earth Sciences

Title: Influence of Landscape Weathering and Fire on Soil Contaminant Reactivity in Western Oregon

Soil and water quality are global concerns that significantly impact human health and the environment. As the demand for soil and water resources increases, it is essential to understand the reactions that govern the fate of contaminants in the environment. Contaminants like arsenic (As), chromium (Cr), nickel (Ni), and manganese (Mn) can pose significant threats to soil and water quality, and complex landscape-scale processes influence their fate. However, understanding how these processes impact soil contaminant reactivity can be complicated due to the inherent spatial and temporal heterogeneity of earth surface processes. For example, soil weathering controls the pedogenic minerals that can react with contaminants and can release metals from parent materials into soils - processes that ultimately occur at the molecular scale but play out across landscapes over large time scales. External perturbations to soil systems, such as wildfires, can further influence soil and water quality by impacting soil contaminant cycling and the minerals governing these reactions. Wildfires are becoming more frequent and severe; hence, it is crucial to understand the landscape controls that drive contaminant reactivity.

The objectives of this work were to (1) understand how soil weathering influences contaminant reactivity (2) quantify fire-induced Cr and Cr-reactive mineral generation and transport from burned soils as a function of landscape position; (3) determine how multiple contaminants (Co, Mn, Ni, and V) are impacted and transported from burned soils across a landscape. Data reveal that amorphous-pedogenic minerals, driven and maintained by soil weathering, greatly influence soil contaminant reactivity. When subjected to fire, amorphous phases associated with contaminants increase before transforming into more crystalline phases with reduced sorption capacities. Furthermore, Cr(VI), a Class A carcinogen, was generated during burning and correlated with amorphous soil minerals that varied across a landscape. Contaminants released and transported from burned soils exceeded drinking water standards for Cr(VI), Mn, and Ni; the degree and persistence of contamination depended on landscape

position. These findings assist in understanding how soil contaminants are influenced by weathering across a landscape and the subsequent transformations and transport that can occur after fire.

This dissertation includes previously published and unpublished coauthored materials.

CURRICULUM VITAE

NAME OF AUTHOR: Chelsea Sabrina Obeidy

DEGREES AWARDED:

Doctor of Philosophy, Earth Science, University of Oregon
Bachelor of Science, Environmental Science and Management, 2017, Cal Poly Humboldt

AREA OF SPECIAL INTEREST:

Environmental Soil Chemistry
Soil Science
Critical Zone Science

PUBLICATIONS:

Chelsea Obeidy and Matthew Polizzotto (2024) "Understanding the Influence of Soil Development on Contaminant Reactivity Along a Fluvial Chronosequence in the Oregon Coast Range" *Geoderma.* http://dx.doi.org/10.2139/ssrn.4461677

Hannah R. Peel, Fatai O. Balogun, Christopher A. Bowers, Cass T. Miller, **Chelsea S. Obeidy**, Matthew L. Polizzotto, Sadeya U. Tashnia, David S. Vinson, and Owen W. Duckworth. (2022) "Towards Understanding Factors Affecting Arsenic, Chromium, and Vanadium Mobility in the Subsurface" *Water* 14, no. 22: 3687. DOI:10.3390/w14223687

Chelsea Obeidy and A. Sharma (2021) "2021 Congressional Visits Day Goes Virtual" *CSA News* DOI:10.1002/csan.20447

JP Berrill, CM Dagley, AJ Gorman, **CS Obeidy**, HK Powell (2018) "Variable-density Retention Promotes Spatial Heterogeneity and Structural Complexity in a Douglas-fir/Tanoak Stand" *Current Trends Forest Research:* CTFR-108. DOI:10.29011/CTFR-108.100008

ACKNOWLEDGMENTS

My profound reverence for soil's essential role in shaping our existence here on Earth has motivated this work. With heartfelt appreciation, I acknowledge the vital functions of soil, which include purifying and storing water (in this dissertation, a source of contamination), modifying our atmosphere, providing nutrients and a medium for plant growth, offering habitat for diverse organisms, and recycling of nutrients and organic wastes. Let us strive to safeguard and cherish the thin veneer of Earth that sustains life!

I want to extend my appreciation to Dr. Matt Polizzotto, who was instrumental in completing this work. His wealth of knowledge and infectious enthusiasm have been a constant source of inspiration. I am immensely grateful for his unwavering support, patience, and encouragement over the years. Working and learning with Matt has been an absolute honor!

Lastly, I am incredibly grateful for my mother, Rafaelina Obeidy, and her unconditional love and support throughout my life. I love you, Mom!

DEDICATION

In loving memory of my brother Aaron (1995-2020), father Moe (1961-2021), and grandfather Baba (1933-2022). Thank you for always believing in me.

TABLE OF CONTENTS

Chapter Page

Chapter Page

Chapter Page

LIST OF FIGURES

Chapter Page

CHAPTER II

Chapter Page

CHAPTER III

CHAPTER IV

LIST OF TABLES

Chapter Page

CHAPTER II

CHAPTER III

CHAPTER IV

CHAPTER I: INTRODUCTION

Soil and water quality are local concerns and global issues that significantly impact human and environmental health. The increasing demand for soil and water resources has made understanding the reactions that govern the fate of contaminants in the environment of utmost importance. Metal(oid) trace elements like arsenic (As), chromium (Cr), nickel (Ni), and manganese (Mn) are prime examples of contaminants that pose threats to human and environmental health across the globe (Peel et al., 2022). The fate of these contaminants in soil and water can vary significantly across landscapes, and understanding how landscape-scale processes influence contaminant reactivity is complicated due to the inherent spatial and temporal heterogeneity of earth surface features and processes.

One critical, yet understudied, control on environmental contaminants is soil weathering. Weathering proceeds as parent material becomes fractured, ground, dissolved, and bioturbated into chemically altered and potentially transportable materials, processes that can take thousands of years (Buol et al., 2011; Peel et al., 2022). At the shortest timescales, chemical reactions taking place at the mineral-water interface can take seconds to minutes, resulting in the ripening of primary minerals, but such processes vary from soil particle (millimeter) to landscape (kilometer) scales (Brantley et al., 2007, 2017; Chorover et al., 2007). Many efforts have been made towards identifying the influences of weathering on Critical Zone (CZ) processes. However, CZ weathering and its influences on reactions that govern contaminant fate and transport are poorly identified and constrained, thereby limiting our ability to effectively maintain soil and water resources.

Weathering and landscape position influence the cycling of soil contaminants through the transformation, formation, and accumulation of secondary minerals. For instance, weathering releases Fe from primary minerals and governs the generation of secondary Fe oxides, hydroxides, and oxyhydroxides that are dynamic and reactive due to their surface structures, areas, and charges (Bigham et al., 2002; Bowell, 1994; Brown et al., 1999; Duckworth et al., 2022). Secondary Fe minerals and their influence over contaminant reactivity have been the focus of extensive research in pure mineral systems (Dixit & Hering, 2003; Ona-Nguema et al., 2005; Raven et al., 1998). However, when this knowledge is upscaled to the field, reactions that govern the sustainability of soil and water quality are not always consistent due to heterogeneity

at various scales within landscapes (Brantley et al., 2007; Hingston et al., 1971; Peel et al., 2022; Smedley & Kinniburgh, 2002; Vitre et al., 1991a).

Field-based experimentation can help facilitate an understanding of the landscape-scale influences on soil properties that govern contaminant reactivity. In particular, making use of chronosequences (time) and toposequences (relief) can enable the systematic examination of these factors by isolating a specific influence. Considering landscape heterogeneity, a nuanced comprehension of multi-scale phenomena is necessary for accurate prediction, effective management, and response to environmental contamination. In coupling field-based experimentation with lab-based observations and experimentation, we can contribute to understanding landscape-scale variations that drive the sustainability of soil and water resources (Buol et al., 2011).

The research presented here integrates field-based assessment with laboratory experimentation to elucidate the interplay between the time of soil weathering, hillslope position, and fire intensity on contaminant reactivity within Western Oregon. I first utilize a soil chronosequence to quantify how secondary pedogenic minerals control soil contaminant mobility and sorption. I then use a serpentine toposequence naturally enriched in Cr, Co, Fe, Ni, and Mn to understand the distribution of geogenic contaminants that are driven by weathering of serpentine/ultramafic rocks. I apply this knowledge to understand how these weathering-derived contaminants may be transformed and mobilized by wildfires, which are increasing in severity and extent in Oregon. Overall, these efforts seek to improve our understanding for how natural and externally driven mineral transformations modify contaminant cycles and influence soil and water sustainability. With human development and pressures like climate change increasingly altering our landscapes, this research enhances our capacity to understand and predict resulting environmental threats.

Dissertation Research

The objectives of my research are to: (1) understand how soil weathering influences contaminant reactivity; (2) quantify Cr generation and potential transport from burned soils across a landscape; and (3) determine how multiple contaminants (Co, Mn, Ni, and V) are impacted and transported from burned soils based on landscape position.

In order to meet my research objectives, I used a well-established chronosequence to investigate the effects of soil weathering on the mineral phases that control contaminant behavior in the environment. I learned that amorphous Fe minerals, influenced by primary mineral weathering rates and subsequent transformation to secondary crystalline minerals, govern contaminant reactivity across a landscape. I then applied this knowledge to a serpentine toposequence with naturally high concentrations of Cr and Fe to understand how landscape weathering and the transformation of contaminant-reactive minerals through fire affect the degree of Cr oxidation and its mobility. By quantifying fire-induced Cr oxidation and Fe mineral transformations with burn intensity, I identified the degree of Cr oxidation and subsequent transport controlled by secondary minerals and soil weathering. I then expand this understanding to include other contaminants, such as Co, Mn, Ni, and V, that are present in the serpentine toposequence. Through this, I identified the transformations of mineral-phase associations and the potential transport of Co, Mn, Ni, and V from burned soils. Across my studies, the data collected highlight the critical role of secondary amorphous minerals in controlling contaminant reactivity across landscapes and how fire and soil weathering transform and maintain these critical minerals that govern contaminant fate in the environment.

My first project, described in Chapter II of this dissertation, shows that soil weathering across a landscape governs Fe and Al mineral phases that influence contaminant reactivity. The influence of soil weathering on contaminant reactivity was evaluated by using As sorption as a proxy. I specifically hypothesized that As sorption would increase with soil age and depth due to the preponderance of secondary mineral oxides generated through weathering. Our findings reveal that As sorption onto soils as a function of soil age and depth did not proceed as initially hypothesized; amorphous minerals, which were dependent on the stage of soil weathering, dominated As sorption. Chemical extractions revealed that amorphous (oxy)hydroxides were the dominant mineral phases governing As sorption, even in the presence of abundant crystalline oxides. Micro-X-ray fluorescence (μ-XRF) revealed a strong spatial correlation between As and Fe in reacted soils. The data collected allowed for the determination of pedogenic controls maintained by weathering on the fate of contaminants across a landscape. Chapter II is titled "Understanding the influence of soil development on contaminant reactivity along a fluvial chronosequence in the Oregon Coast Range" and is published in the Elsevier journal *Geoderma*. It is coauthored by Dr. Matthew Polizzotto (Obeidy & Polizzotto, 2024).

Chapter III pertains to soil weathering and modification by fire across a serpentine landscape in the Rogue River-Siskiyou National Forest, Oregon. Soil weathering drives the inherent concentrations and forms of Cr and Fe. My specific objectives were to quantify the fire-induced generation, availability, and transport of Cr(VI) and observe the mineral transformations and phase associations of Fe and Cr across a hillslope burned to different intensities. I hypothesized that soils derived from in-situ weathering of the underlying contaminant-rich bedrock (summit position) would generate the greatest concentrations and availability of Cr(VI), and these hypotheses were supported with a suite of data from analytical approaches characterizing the abundance and phase-associations of Cr(VI). Micro-X-ray fluorescence (μ-XRF) analyses of burned soils revealed that Cr(VI) was generated around chromite-rich particles and throughout the mineral matrix. Chemical extractions and synchrotron X-ray diffraction exposed that Cr-reactive minerals and Fe(oxy)hydroxides were generated and subsequently transformed into new crystalline minerals with increased burn intensity, which varied across the hillslope due to weathering's control on Fe-mineral phases. Finally, of critical importance to management and environmental health protection, transport experiments highlighted that regardless of hillslope position, Cr(VI) was leached from burned soils at concentrations that exceeded drinking water standards. Collectively, these findings achieved my objectives of understanding how weathering products such as Cr and Fe released into soils can vary across a landscape and how, when exposed to fire, Cr(VI) can be generated and transported at different rates depending on burn intensity and landscape position.

Chapter IV, expands our understanding of the influence of soil weathering and fire-induced contaminant reactivity across a landscape to other geogenic contaminants found within serpentine soils (Co, Mn, Ni, and V). Since I established that soil weathering across a landscape governed the degree of Cr(VI) found within soils and the subsequent transformation and reactivity by fire, we expected a similar result for other contaminants. I specifically hypothesized that the summit soils would release the greatest concentration of contaminants and that contaminant-reactive minerals (Fe-(oxy)hydroxides) would transform towards more crystalline phases before contaminants were included into newly formed minerals at the highest burn intensities. Our data highlight that Co, Ni, and Mn are associated with amorphous and crystalline minerals, which decrease with burn intensity, while V availability increases with burn intensity. Chemical extractions highlight that soil weathering determined the degree of contaminants found

across a landscape and that these contaminants were greatest at the summit position. Results from transport experiments highlight that regardless of hillslope position, Ni and Mn were transported from soils at concentrations that exceeded drinking water standards. Furthermore, we also identified that Mn was transported above drinking water standards from unburned soils across the serpentine landscape. These results partially support my hypothesis that summit position soils had the greatest concentrations of contaminants and that their association with amorphous and crystalline pedogenic minerals decreased with increased crystallinity and inclusion into new minerals. These findings facilitate an understanding of how soil contaminants are influenced by weathering across a hillslope and the subsequent transformations and transport that can occur after fire.

REFERENCES

Bigham, J. M., Fitzpatrick, R. W., & Schulze, D. G. (2002). Chapter 10 Iron Oxides. *Soil Mineralogy with Environmental Applications.*, *7*, 323–376.

Bowell, R. J. (1994). Sorption of arsenic by iron oxides and oxyhydroxides in soils. *Applied Geochemistry*, *9*(3), 279–286. https://doi.org/10.1016/0883-2927(94)90038-8

Brantley, S. L., Goldhaber, M. B., & Vala Ragnarsdottir, K. (2007). Crossing disciplines and scales to understand the critical zone. *Elements*, *3*(5), 307–314. https://doi.org/10.2113/gselements.3.5.307

Brantley, S. L., McDowell, W. H., Dietrich, W. E., White, T. S., Kumar, P., Anderson, S. P., Chorover, J., Ann Lohse, K., Bales, R. C., Richter, D. D., Grant, G., & Gaillardet, J. (2017). Designing a network of critical zone observatories to explore the living skin of the terrestrial Earth. *Earth Surface Dynamics*, *5*(4), 841–860. https://doi.org/10.5194/esurf-5-841-2017

Brown, G. E., Foster, A. L., & Ostergren, J. D. (1999). *Mineral surfaces and bioavailability of heavy metals: A molecular-scale perspective* (Vol. 96). www.pnas.org.

Buol, S. W., Southard, R. J., Graham, R. C., & P.A., M. (2011). *Soil Genesis and Classification* (Sixth). Wiley-Blackwell.

Chorover, J., Kretzschmar, R., Garcia-pichel, F., & Sparks, D. L. (2007). Soil Biogeochemical Processes within the Critical Zone. *Elements*, *3*, 321–326.

Dixit, S., & Hering, J. G. (2003). Comparison of arsenic(V) and arsenic(III) sorption onto iron oxide minerals: Implications for arsenic mobility. *Environmental Science and Technology*, *37*(18), 4182–4189. https://doi.org/10.1021/es030309t

Duckworth, O. W., Polizzotto, M. L., & Thompson, A. (2022). *tackle soil contaminants*. https://doi.org/10.3389/fenvs.2022.981607.Bringing

Hingston, F. J., Posner, " A M, Quirk, J. P., & Hpoi-, +. (1971). *Competitive Adsorption of Negatively Charged Ligands on Oxide Surfaces*.

Obeidy, C. S., & Polizzotto, M. L. (2024). Understanding the influence of soil development on contaminant reactivity along a fluvial chronosequence in the Oregon Coast Range. *Geoderma*, *442*. https://doi.org/10.1016/j.geoderma.2024.116784

Ona-Nguema, G., Morin, G., Juillot, F., Calas, G., & Brown, G. E. (2005). EXAFS analysis of arsenite adsorption onto two-line ferrihydrite, hematite, goethite, and lepidocrocite. *Environmental Science and Technology*, *39*(23), 9147–9155. https://doi.org/10.1021/es050889p

Peel, H. R., Balogun, F. O., Bowers, C. A., Miller, C. T., Obeidy, C. S., Polizzotto, M. L., Tashnia, S. U., Vinson, D. S., & Duckworth, O. W. (2022). Towards Understanding Factors Affecting Arsenic, Chromium, and Vanadium Mobility in the Subsurface. *Water (Switzerland)*, *14*(22), 1–36. https://doi.org/10.3390/w14223687

Raven, K. P., Jain, A., & Loeppert, R. H. (1998). Arsenite and arsenate adsorption on ferrihydrite: Kinetics, equilibrium, and adsorption envelopes. *Environmental Science and Technology*, *32*(3), 344–349. https://doi.org/10.1021/es970421p

Smedley, P. L., & Kinniburgh, D. G. (2002). A review of the source, behaviour and distribution of arsenic in natural waters. In *Applied Geochemistry* (Vol. 17, Issue 5, pp. 517–568). https://doi.org/10.1016/S0883-2927(02)00018-5

Vitre, R. De, Belzile, N., & Tessier, A. (1991). Speciation and adsorption of arsenic on diagenetic iron oxyhydroxides. In *Limnology and Oceanography* (Vol. 36, Issue 7, pp. 1480–1485). https://doi.org/10.4319/lo.1991.36.7.1480

CHAPTER II: THE INFLUENCE OF SOIL DEVELOPMENT ON CONTAMINANT REACTIVITY ALONG A FLUVIAL CHRONOSEQUENCE IN THE OREGON COAST RANGE

Published as: Obeidy, C. S., & Polizzotto, M. L. (2024). Understanding the influence of soil development on contaminant reactivity along a fluvial chronosequence in the Oregon Coast Range. *Geoderma*, 442. https://doi.org/10.1016/j.geoderma.2024.116784

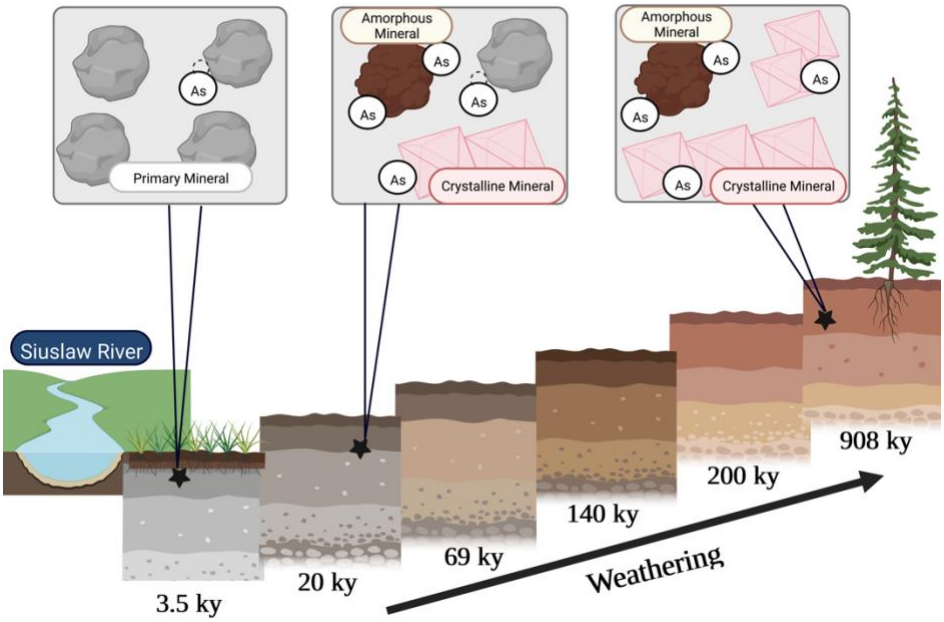

Conceptual Abstract. Conceptual diagram of the Oregon Coast Range chronosequence and the dominant host-phases that govern contaminant reactivity as a function of age. Soils that had the greatest affinity for arsenic sorption were the 20-ky soils and sorption affinity was tied to concentrations of amorphous minerals, which is governed by the rates of primary mineral weathering and the formation of secondary mineral. Created with biorender.com.

Highlights:

- Soil development impact on contaminant reactivity was quantified for a chronosequence
- Soil arsenic sorption varied with soil age and depth
- Arsenic sorption capacity was most influenced by soil amorphous oxide mineral content
- Amorphous oxide content is balanced by primary mineral weathering and ripening
- Soil weathering stage is a critical driver of soil and water quality

ABSTRACT

Weathering processes are recognized as drivers of soil and water resource sustainability, but how pedogenesis stage impacts contaminant reactivity and mobility in soils has been minimally investigated. The primary goal of this study was to quantify how soil development influences contaminant reactivity. To achieve this goal, soils from two depths (30 and 100 cm) across a chronosequence (ages 3.5, 20, 69, 140, 200, and 908 ky) in the Oregon Coast Range were subjected to arsenic (As) adsorption isotherms, with As removal from solution serving as a proxy for soil-contaminant reactivity. Langmuir models were applied to isotherm data to quantify relationships between contaminant retention capacity, soil age and soil physicochemical properties, and data revealed that 20 ky soils from a 30-cm-depth had the greatest affinity for As sorption (8,474.5 mg kg^{-1}). Chemical extractions revealed that amorphous (oxy)hydroxides were the dominant mineral phases governing As sorption, even in the presence of abundant crystalline oxides. Micro-X-ray fluorescence spectroscopy revealed a strong spatial correlation between As and Fe in reacted soils. The abundance of amorphous minerals within soils is controlled by the balance between their production from weathering of primary minerals and their loss from ripening to crystalline minerals, and because the mode, extent and minerals governing contaminant sorption determine solid-aqueous phase partitioning, this knowledge will assist in improving models for predicting Critical Zone processes that govern the sustainability of soil and water quality.

INTRODUCTION

The spatial and temporal heterogeneity of weathering complicate projections of contaminant cycling onto our understanding of water and soil resource sustainability. Weathering proceeds as parent material becomes fractured, ground, dissolved, and bioturbated into chemically altered and potentially transportable materials, processes that can take thousands of years (Buol et al., 2011). At the shortest timescales, chemical reactions taking place at the mineral-water interface can take seconds to minutes, resulting in the ripening of primary minerals, but such processes vary from soil particle (millimeter) to landscape (kilometer) scales (Brantley et al., 2017, 2007; Chorover et al., 2007). Many efforts have been made towards

identifying the influences of weathering on Critical Zone (CZ) processes. However, CZ weathering and its influences on reactions that govern contaminant fate and transport are poorly identified and constrained.

Weathering drives the transformation, formation, and accumulation of secondary minerals that are essential for understanding and predicting contaminant reactivity in soils. For instance, weathering releases Fe from primary minerals and governs the generation of secondary Fe oxides, hydroxides, and oxyhydroxides that are dynamic and reactive due to their surface structures, areas, and charges (Bigham et al., 2002; Bowell, 1994; Brown et al., 1999; Duckworth et al., 2022). Secondary Fe minerals and their influence over contaminant reactivity have been the focus of extensive research in pure mineral systems (Dixit and Hering, 2003; Ona-Nguema et al., 2005; Raven et al., 1998). However, when this knowledge is upscaled to the field, reactions that govern the sustainability of soil and water quality are not always consistent due to heterogeneity at various scales within a landscape (Brantley et al., 2007; Hingston et al., 1971; Peel et al., 2022; Smedley and Kinniburgh, 2002; Vitre et al., 1991a).

Pedogenic Fe-mineral transformations through weathering and their influence on contaminant sorption have begun to be investigated using chronosequences. In volcanic soils ages 1.5 to 1,070 ky, amorphous Fe phases (denoted 'Feo' for their characterization via oxalate-based extractions) have been identified as the dominant hosts for sorption of contaminants, with sorption affinities for copper (Cu) and cadmium (Cd) decreasing with age as Fe-mineral crystallinity and electrical conductivity increased (M. Rechberger et al., 2020; M. Rechberger et al., 2020). In contrast, the influence of soil weathering on sorption of dissolved PO_4^{3-} in a young volcanic chronosequence (0.77 – 1.2 ky) found that sorption increased with soil age, regardless of depth, and was correlated with increasing allophane concentrations (Lilienfein et al., 2004). Within these systems, the underlying mechanistic controls of weathering on contaminant reactivity need to be further identified, particularly for non-volcanic soils.

The present study seeks to examine contaminant reactivity as a function of weathering in nonvolcanic soils. We specifically hypothesized that arsenic (As) sorption would increase with soil age and depth due to the preponderance of secondary Fe minerals generated through weathering. To test this hypothesis, we harnessed samples from a well-characterized chronosequence in the Oregon Coast Range (OCR) in order to link the influences of weathering on processes that govern contaminant mobility. We sought to quantify (1) arsenic sorption within

the OCR as a function of soil age and depth and (2) the dominant host phases governing As sorption as a function of age and depth. Our findings reveal that As sorption onto soils as a function of age and depth did not proceed as initially hypothesized, with amorphous minerals dominating arsenic sorption but the magnitude of sorption varying based on weathering stage. This work highlights the need for understanding the intricacies of weathering-influenced reactions that govern the sustainability of soil and water resources.

MATERIALS AND METHODS

Study Site and Soil Samples

Soils from a well-characterized fluvial chronosequence were used to elucidate the influence of soil pedogenesis on contaminant reactivity (SI Table 2.1, SI Table 2.2) (Almond et al., 2007; Hunter et al., 2023; Lindeburg et al., 2013). Six soil terraces of ages 3.5, 20, 69, 140, 200, and 908 ky were used in this analysis. Soils are derived from the Tyee Formation, a lithified Eocene-aged sandstone-dominated ramp turbidite sequence found in the Coast Range of western Oregon, USA (Figure 2.1) (Heller and Dickinson, 1985). The dominant parent material mineralogy of this formation consists of quartz, andesine, calcic andesine, and lithic fragments (Heller et al., 1985; Lindeburg et al., 2013; Ryu, 2003; Snavely et al., 1964). Time-dependent alterations include profile thickness, soil redness, and accumulation of secondary minerals. Pedogenesis within this chronosequence is dominated by the transformation of primary minerals to secondary clays and metal (oxy)hydroxides. Pedogenic Al decreases while Fe increases with terrace age (Figure 2.2). Non-quartz Si is either leached or bound in secondary aluminosilicate clays.

Oregon Coast Range soils from 3.5, 20, 69, 140, 200, and 908 ky terraces were used for sorption isotherms, and for all but one terrace, 30- and 100-cm-depth soils were tested; the exception was for the 3.5 ky terrace because soil did not reach 100-cm depth. These samples represent all the characterized terrace ages and depth increments from the target chronosequence (Lindeburg et al., 2013). Soils from each terrace age were used to identify the influence of soil age on sorption capacities, and 30- and 100-cm depths were utilized to identify pedogenic variabilities with depth. Soils were all oven-dried for 48 h at 105 ^{o}C and passed through a 2-mm

sieve. Amorphous and crystalline Fe and Al were extracted by 0.2 M ammonium acid and oxalic acid buffered at a pH of 3 (McKeague JA et al., 1971) and citrate-bicarbonate-dithionite (Mehra and Jackson, 1958), respectively. The resulting data are presented in Figure 2.2 and SI Table 2.3, with oxalate extractable designating amorphous Fe and Al (oxy)hydroxide phases, and dithionite extractable designating crystalline Fe and Al (oxy)hydroxide phases (Lindeburg et al., 2013).

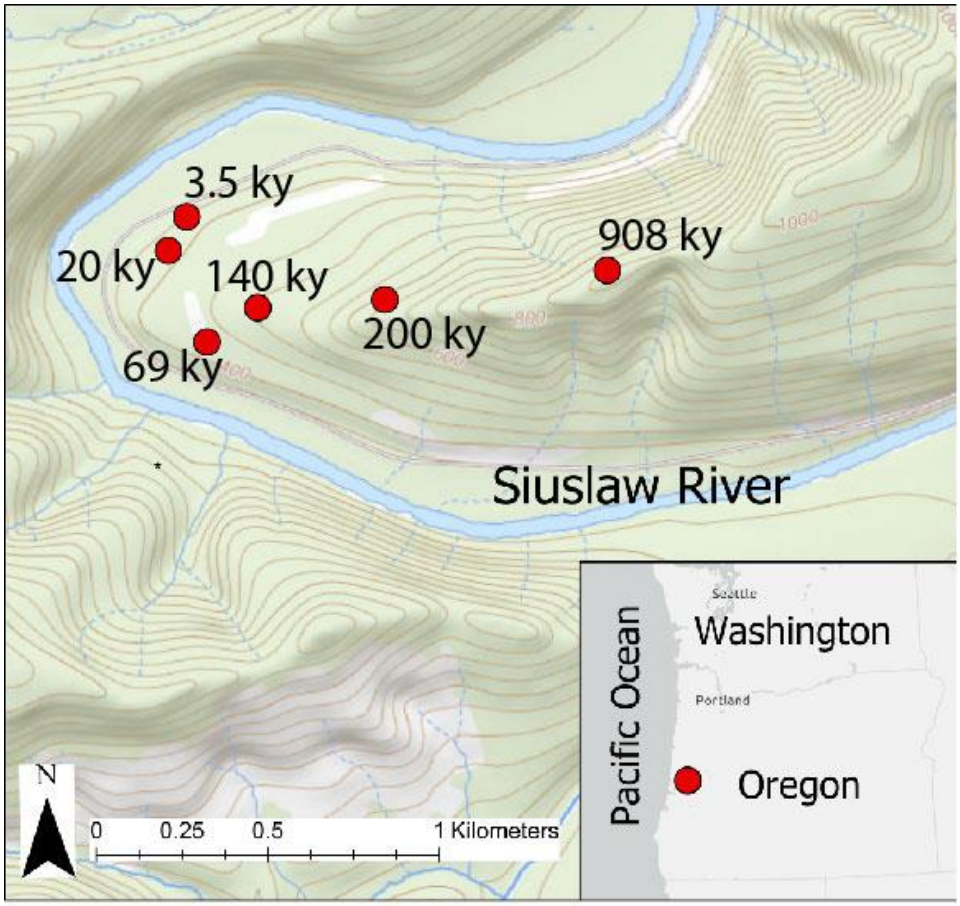

Figure 2.1. Location of fluvial chronosequence analyzed along the Siuslaw river in the Siuslaw National Forest in western Oregon, USA. Soils range in age from 3.5 ky to 908 ky and elevation varies by 163 m (Almond et al., 2007; Hunter et al., 2023; Lindeburg et al., 2013).

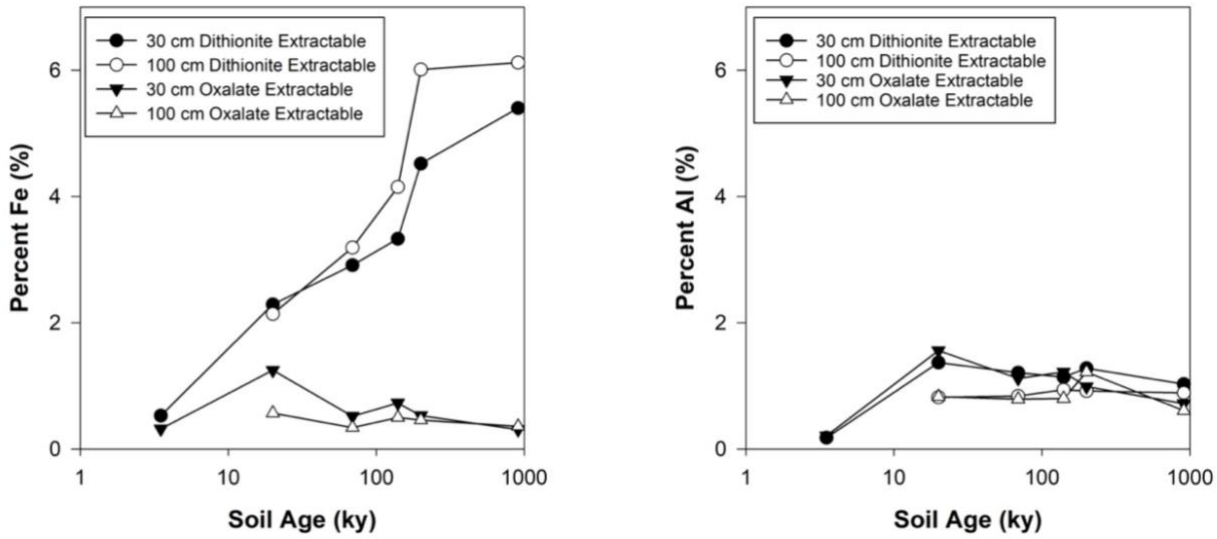

Figure 2.2. (Left) Percent of dithionite-extractable and oxalate-extractable Fe from 30- and 100-cm depth in OCR soils. (Right) Percent of dithionite extractable and oxalate extractable Al from 30- and 100-cm depth in OCR soils. Data were obtained from (Lindeburg et al., 2013).

Adsorption Isotherms

Arsenic sorption isotherms were conducted to quantify how soil age influenced contaminant reactivity. For each selected soil sample, one gram of soil was mixed with 10 mL of solution containing one of seven concentrations of As, ranging from 0 to 1,000 mg L^{-1}. Arsenic was added as $Na_2HAsO_4 \cdot 7H_2O$ (Alfa Aesar crystalline powder), and 0.1 M NaCl (VWR Chemicals) was also included in the solutions to maintain ionic strength. pH was maintained at in-situ soil conditions (pH 5 ± 0.2) by HCl or NaOH addition every 24 h. Soil slurries were shaken on a SCILOGEX MX-RD-pro shaker at room temperature for 48 h, then centrifuged at 10,000 rpm for 15 min. Soils were then decanted, and resulting solutions were filtered through 1-µm Whatman filter paper before being acidified with one drop of concentrated HNO_3. Solutions were stored in a refrigerator and diluted 100-fold in 2% HNO_3 for As analysis via inductively coupled plasma-optical emission spectroscopy (ICP-OES) at Oregon State University's Keck Laboratory. The detection limit for As on the Spectros Arcos ICP-OES in side-on view is ~0.05 mg L^{-1}. Starting As sorption solutions were acidified and refrigerated until analysis, along with triplicate soil blanks to ensure quality control. All experiments and analyses were conducted in triplicate.

Data generated from sorption isotherms were used to model As sorption characteristics for each soil sample. Data conformed best to Langmuir models (R^2 = 0.99), and the following equation was used quantify the maximum As sorption capacity (q_{max}) for each soil:

$$(q = \frac{K_L\, C_{eq}\, q_{max}}{1 + K_L\, C_{eq}})$$

In this equation, K_L is the Langmuir constant, C_{eq} is equilibrium concentration of As remaining in solution after sorption isotherms, and q is the equilibrium concentration of As (mg kg^{-1}) that sorbed onto soils. The maximum sorption capacity, q_{max}, was derived for each sample and used as a metric for comparison of arsenic sorption capacities across all tested soil samples.

Chemical Extractions

Ammonium oxalate/oxalic acid extractions were conducted to target amorphous phases that served as the host phase for As after sorption incubations. Ammonium oxalate and oxalic acid extracts target As coprecipitated with amorphous Fe and Al (oxy)hydroxides by ligand-promoted dissolution (Keon et al., 2001). Extractions were conducted in triplicate on soils that were dosed with 1,000 mg L^{-1} of As. Soils used for extractions came from 20- and 908-ky soils from a 30- and 100-cm depth, as they represented the most contrasting soils with respect to stage of weathering and arsenic sorption. Soils were air dried after As isotherms, then 0.4 g of soil and 40 mL of 0.2 M ammonium oxalate and oxalic acid solution were placed into 50 mL HDPE centrifuge tubes and vortexed before placing on a shaker. Samples were shaken in the dark on an Orbital Shaker SYC-2102A at room temperature for 2 h. After the 2-h incubation period, samples were centrifuged at 2,000 rpm for 15 min. Solutions were then filtered through 1-µm Whatman filter paper, acidified, and stored in the refrigerator. Samples were then diluted 100-fold in 2% HNO_3 and analyzed for As on the ICP-OES at Oregon State University. All analyses were conducted in triplicate.

Citrate-bicarbonate-dithionite (CBD) extractions were conducted to target crystalline Fe-(oxy)hydroxides that were associated with As after sorption isotherms (Mehra and Jackson, 1958). Extractions were conducted on 20- and 908-ky soils from 30- and 100-cm depth that were dosed with 1,000 mg L^{-1} of As and 0.1 NaCl, as previously described. For each sample, 0.4 g of dosed soils were placed into 50 mL HDPE centrifuge tubes along with 20 mL of 0.3 M sodium citrate and 2.5 mL of 1 M sodium bicarbonate. Samples were heated in a hot water bath to 80 °C,

then 0.5 g of sodium dithionite were added. Samples were in the hot water bath for 30 min and shaken intermittently, after which, soils were removed and centrifuged at 2,000 rpm for 15 min. Solutions were then filtered using 1-µm Whatman filter paper, preserved with concentrated HNO_3, and stored in the refrigerator until analysis. Samples were diluted 100-fold in 2% HNO_3 and analyzed for As on the ICP-OES at Oregon State University. All analyses were conducted in triplicate.

Micro-X-Ray Fluorescence Imaging

Micro X-ray fluorescence (μ-XRF) elemental mapping was conducted on Beamline 2-3 at the Stanford Synchrotron Radiation Lightsource (SSRL) to identify spatial relationships between As and soil elements. Two soils with contrasting ages and depths were analyzed: 20 ky from a 30-cm-depth and 908 ky from a 100-cm-depth. Soils were dosed with 1,000 mg L^{-1} of As, dried, and then thin-sectioned at Spectrum Petrographics. Thin sections were mounted onto quartz glass slides using Epotex-301 resin**.** μ-XRF mapping was conducted in fluorescence mode using a harmonic rejection mirror and a channel-cut Si(III) monochromator. The beam was 2 µm by 2 µm beam size. Elemental maps were created with 7 µm step sizes and 25 ms dwell times at an incident energy of 12 keV. Data were analyzed via Sam's Microprobe Analysis Kit (Webb, 2011).

RESULTS

Adsorption model

The sorption of As onto soils of 30- (Figure 2.3a) and 100-cm (Figure 2.3b) depths as a function of soil age is presented in Figure 3. Experimental data conformed to L-curves and were best fit to a Langmuir sorption models ($R^2 > 0.99$). Parameters derived from Langmuir fits are presented in Tables 2.1 and 2.2. Variability in As sorption was more apparent across the soils from 30-cm than it was in the 100-cm soils. Langmuir-calculated As sorption maximum (q_{max}) was lowest in the youngest soil (3.5 ky, 30 cm), with a value of 1,666 mg As kg^{-1} but was greatest in the next-youngest soil examined (20 ky, 30 cm), with a value of 8,475 mg As kg^{-1} (Table 2.1, Figure 2.4). As soils got older, calculated q_{max} values clustered from 6,622 to 7,143 mg As kg^{-1} in 30-cm samples. Soils at depth (100 cm) had sorption maxima that were clustered

between 5,000-7,900 mg As kg^{-1}, with the greatest As sorption observed with the 200 ky sample (Table 2.2, Figure 2.4).

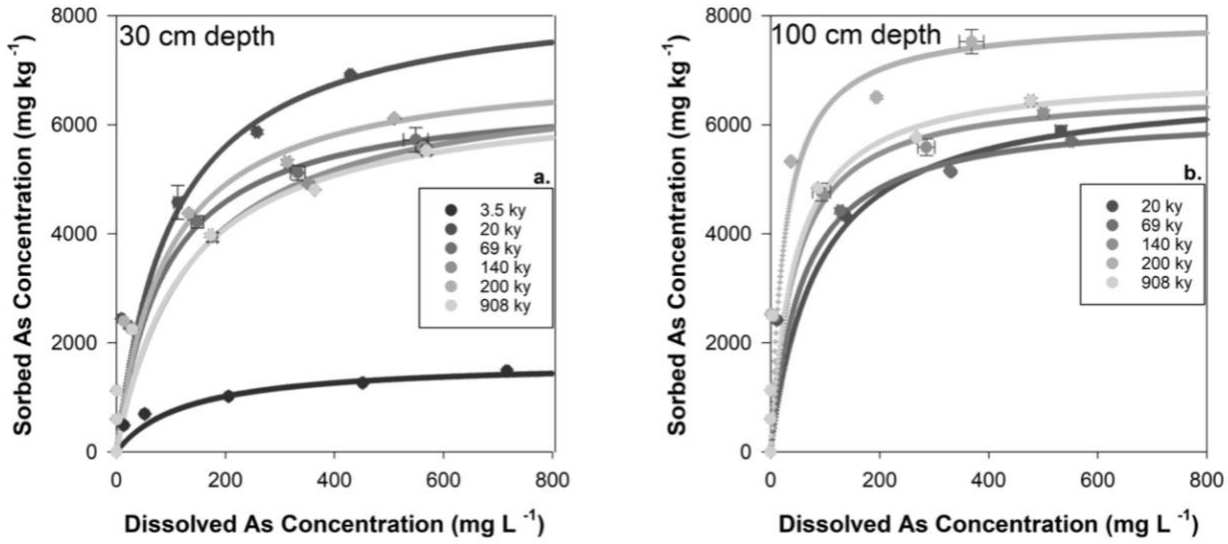

Figure 2.3. Experimental data (symbols) and Langmuir models (lines) of As sorption in varying aged soils from two depths, 30 (3a) and 100 (3b) cm. Soils were incubated in 0 – 1,000 mg L^{-1} As solution. Experimental data is averaged from triplicate samples and standard error is calculated from triplicate samples.

Table 2.1. Langmuir model parameters calculated from As sorption isotherms for 30-cm-depth soils. q_{max} represents the maximum sorption capacity and K_L is the Langmuir constant.

Terrace Age (ky)	q_{max} (mg kg^{-1})	K_L	R^2
3.5	1666.66	0.0078	0.998
20	8474.58	0.0098	0.995
69	6622.52	0.0113	0.999
140	6944.44	0.0073	0.999
200	7142.86	0.0109	0.995
908	6666.67	0.0080	0.995

Table 2.2. Langmuir model parameters calculated from As sorption isotherms for 100-cm-depth soils. q_{max} represents the maximum sorption capacity and K_L is the Langmuir constant.

Terrace Age (ky)	q_{max} (mg kg^{-1})	K_L	R^2
20	6756.76	0.0116	0.994
69	6250.00	0.0171	0.998
140	6666.67	0.0228	0.997
200	7936.51	0.0378	0.993
908	6944.44	0.0226	0.997

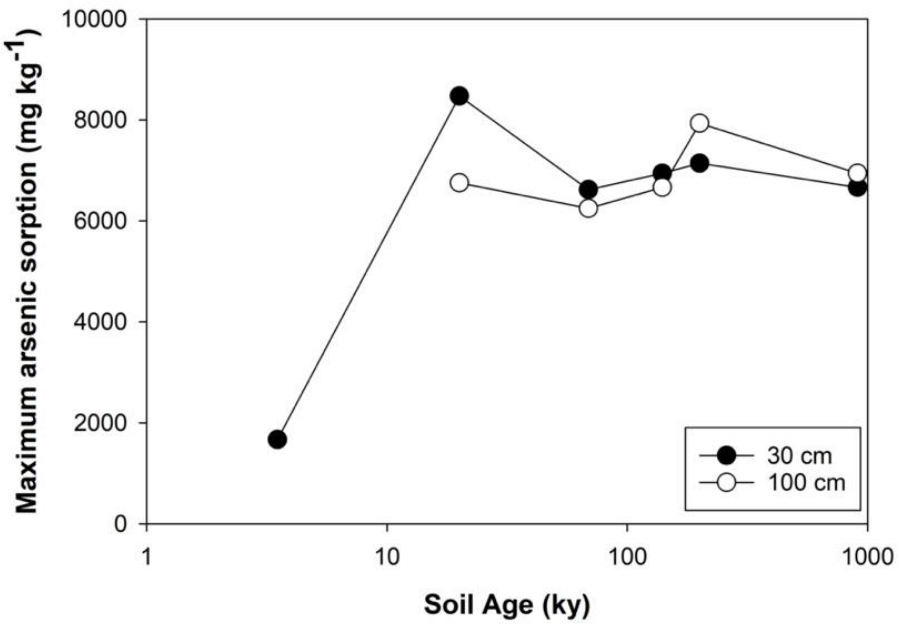

Figure 2.4. Arsenic sorption maxima (q_{max}) as a function of soil terrace age from 30- (black symbols) and 100-cm (white symbols) soils. Maximum capacity for As sorption (q_{max}) was calculated using experimental data and the Langmuir model.

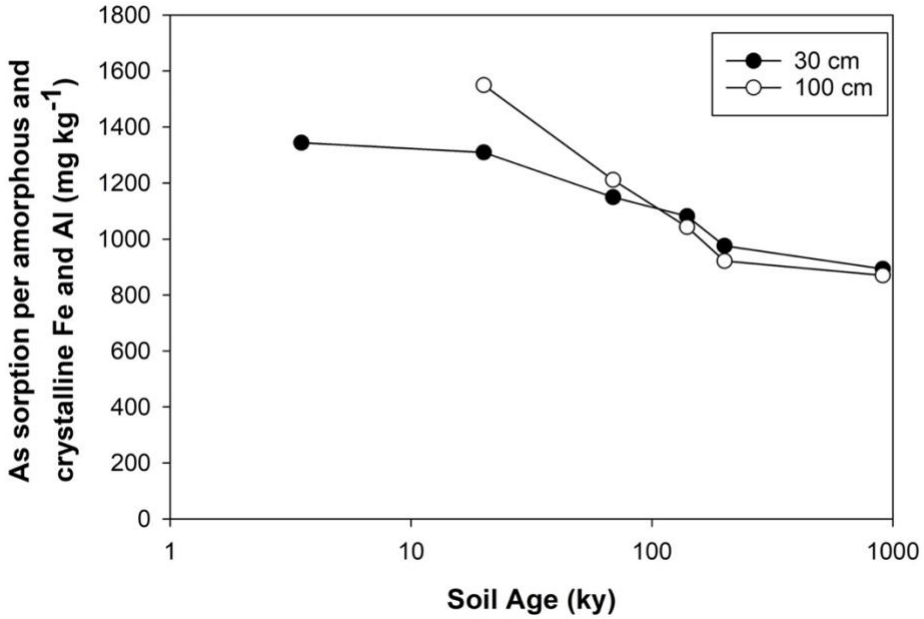

Figure 2.5. Maximum As sorption per amorphous (Feo and Alo) and crystalline (Fed and Ald) phases in 30- and 100-cm soils from the OCR chronosequence. Concentrations of Feo, Fed, Alo, and Ald were provided by Lindeburg et al., 2013.

Maximum As sorption capacity per amorphous and crystalline Fe and Al from 30- and 100-cm soils is presented in Figure 2.5. Concentrations of Feo, Fed, Alo, and Ald, indicative of amorphous and crystalline Fe and Al, were provided by Lindeburg et al., (2013) and summed. Arsenic sorption per Fe and Al-phases in 30- and 100-cm soils decreased with soil age, from 1,549 to 870 mg kg^{-1}. The highest As sorption per Fe and Al phases was in 20-ky soils from a 100-cm depth and the lowest sorption was in 200-ky soils from a 100-cm depth. Arsenic sorption per Fe and Al phases decreased more rapidly in soils from a 100-cm depth than from 30-cm depth, and both soil depths remained relatively consistent in As sorption capacities between 200 and 908 ky. Arsenic sorption per Fe and Al was relatively consistent in soils from 30-cm depth 3.5 to 20 ky and then gradually decreased with soil age. In 100-cm soils, As sorption per Fe and Al decreased substantially between 20- and 200-ky soils, and thereafter, As sorption decreased minimally with soil age.

Arsenic Host Phases

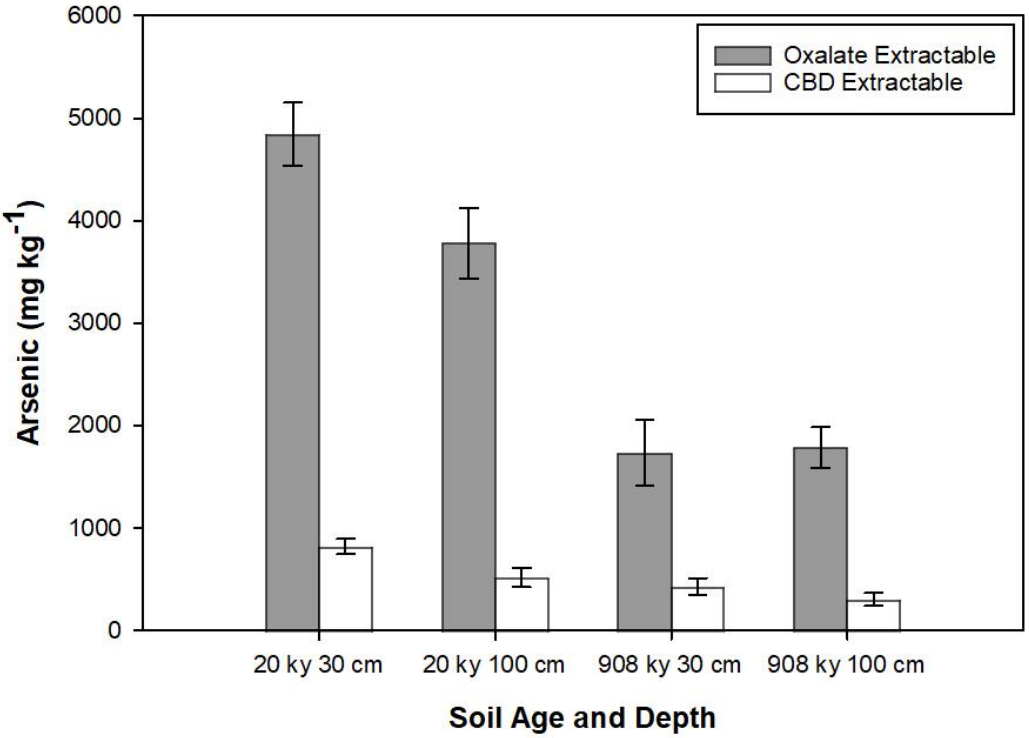

Figure 2.6. Concentrations of oxalate- and CBD-extractable As. Extractions were conducted on soils that were 20- and 908-ky old, from both 30- and 100-cm depths. Soils were dosed with 1,000 mg L^{-1} As for 48 h prior to extractions. Error bars represent standard error of experimental triplicates.

Chemical extractions revealed that after incubation of 1,000 mg L^{-1} As solution, amorphous materials (ammonium oxalate and oxalic acid extractable) were the dominant host-phases of sorbed As (Figure 2.6). The highest concentration of As extracted was from oxalate extractions in 20-ky soils from a 30-cm depth (4,842.7 mg kg^{-1}), followed by 20-ky soils from a 100-cm depth (3,781.6 mg kg^{-1}); these soils sorbed 64-69% of As from solution. Oxalate extractions of As-doped, 908-ky soils from 30- and 100-cm-depth yielded 1,736.3 mg kg^{-1} and 1,786.5 mg kg^{-1} of As, respectively, indicating that 27-31% of added As sorbed to amorphous phases. Citrate-bicarbonate-dithionite extractions, indicative of As sorbed to crystalline oxide phases, yielded less As than all oxalate extractions, with As extracted ranging from 215.1 mg kg^{-1} (908 ky, 100-cm-depth) to 724.2 mg kg^{-1} (20 ky, 30-cm depth).

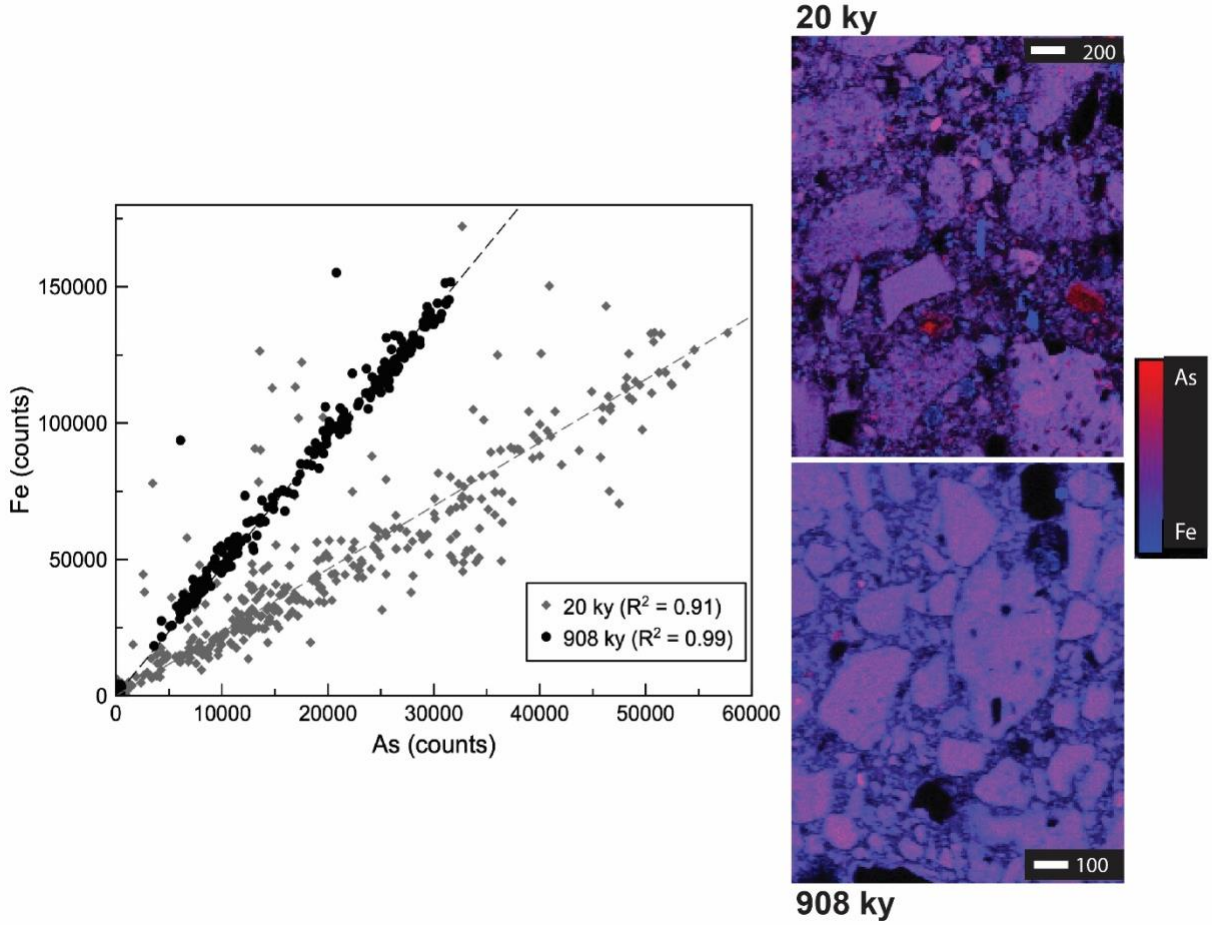

Figure 2.7. Solid phase bicolor elemental maps and correlation plot based on counts of As and Fe obtained from μ-X-ray fluorescence elemental mapping of OCR soils dosed with As. Left: As-Fe spatial correlation plots; grey diamonds represent 20-ky soils from 30-cm-depth and black circles represent 908-ky soils from 100-cm-depth. Right: As and Fe elemental distribution maps; 20-ky (top) and 908-ky (bottom) soils, with red and blue coloration representing As and Fe counts, respectively.

Micro X-ray fluorescence (μ-XRF) analyses revealed that As was strongly associated with Fe in both 20-ky, 30-cm-depth soil and 908-ky, 100-cm-depth soil (Figure 2.7). In 20 ky soils, As was less homogenously associated with Fe and there were more independent zones of As whereas As sorption in 908 ky soil was more homogenously associated with Fe, reflected by the slightly higher R^2 values quantifying spatial correlation between the elements (0.99 for 908-ky soil and 0.91 for 20-ky soil).

DISCUSSION

Progression of soil weathering

Soil weathering in the OCR chronosequence is dominated by the conversion of primary minerals into secondary minerals and oxides. The percentage of oxalate-extractable Fe in soils minimally varies with age and depth (0.32- 1.25% oxalate-extractable Fe); the highest concentration was in 20 ky soils from a 30-cm depth while the lowest was in 908 ky soils from a 30-cm depth (Figure 2.2). Except for 908 ky soils, all soils had higher concentrations of oxalate-extractable Fe at a 30-cm depth than at 100-cm depth (Figure 2.2). Relatively stable concentrations of oxalate-extractable Fe that persist in soils throughout pedogenesis are maintained by a balance between the rates of Fe weathering from primary minerals to amorphous oxides (oxalate extractable) and the ripening from amorphous to crystalline Fe-oxide phases (dithionite extractable). Dithionite-extractable Fe concentrations in OCR soils increase with soil age from ~0.5 to 6% Fe. Between 200 ky and 908 ky, soils at depth (100 cm) appear to reach steady-state concentrations of dithionite-extractable Fe, which is likely limited by primary mineral weathering rates (Figure 2.2), although Feo:Fed decreases (SI Figure 2.2). Aluminum varied minimally with pedogenesis and at depth; oxalate-extractable Al (0.21 – 1.56 %) and dithionite-extractable Al (0.18 – 1.37%) were highest in soils from a 30-cm-depth. Between 3.5 and 20 ky, soils increase in oxalate- and dithionite-extractable Al, which is likely indicative of the ripening of primary Al-minerals (Figure 2.2).

The development of secondary oxides within the OCR chronosequence is consistent with the general model of pedogenesis in non-volcanic soils. Oxalate-extractable Fe concentrations are highest in moderately young soils and slightly decrease with soil age and depth (McFadden and Hendricks, 1985). Accumulation of dithionite-extractable Fe from 69 - 200 ky in OCR soils is consistent with other chronosequences, where the increasing dithionite-extractable Fe was observed from 105 - 490 ky and was attributed to the release of the Fe-containing primary minerals through weathering (Figure 2.2) (Lawrence et al., 2015; Schulz et al., 2010). After the rapid accumulation of dithionite-extractable Fe, steady-state concentrations are reached due to exhumation of primary Fe-bearing minerals; in OCR soils, this was observed between 200 - 908 ky, and this has been reported in other chronosequences between 300 – 600 ky (Figure 2.2) (Aniku and Singer, 1990).

Arsenic sorption as a function of soil age and depth

The rates of weathering and generation of amorphous-secondary minerals ultimately govern contaminant fate in the subsurface environment. We initially hypothesized that the preponderance of Fe-oxide minerals present in OCR soils would result in increased As sorption with soil age and with depth. However, contrary to our hypothesis, we did not observe a correlation between soil age and As sorption maxima but rather, As sorption per (oxy)hydroxide Fe and Al (oxalate- and CBD-extractable Fe) decreased through pedogenesis after 3.5 ky (Figure 2.5). Although crystalline Fe- and Al-oxide phases are well-established sorbents for As (Giménez et al., 2007; Grafe et al., 2001; Ladeira and Ciminelli, 2004; Mamindy-Pajany et al., 2009; Smedley and Kinniburgh, 2002), oxalate-extractable phases, indicative of amorphous Fe-oxide and possibly amorphous Al-oxide phases, disproportionately influenced contaminant sorption in our samples, regardless of soil age and depth. Comparing samples from different depths, 30-cm soils had a higher affinity for As sorption than 100-cm soils until 200 ky, after which trends reversed (Figure 2.3).

Previous studies that have investigated the influences of weathering on contaminant reactivity have observed peak sorption maxima at a younger stage of pedogenesis than what was observed in the OCR soils. In volcanic soils, contaminant sorption is highest at an earlier stage of pedogenesis (1.2 -1.5 ky), while OCR soils reached maximum sorption in 20 ky soils (Figure 2.3) (Lilienfein et al., 2004; Rechberger et al., 2020; Rechberger et al., 2021). In these studies, soil sorption maxima of Cd and Cu decreased with increased soil weathering (Rechberger et al., 2020; Rechberger et al., 2021). The delayed maximum sorption affinities in OCR soils are likely due to differences in volcanic and non-volcanic parent material weathering rates; poorly crystalline volcanic parent materials weather more rapidly and generate higher concentrations of amorphous materials that have been linked to increased contaminant reactivity at early stages of pedogenesis (Buol et al., 2011; Shoji et al., 1993). Our results highlight the delayed generation of oxalate-extractable minerals in non-volcanic soils that disproportionately influence contaminant reactivity.

Factors governing arsenic sorption

Chemical extractions revealed that the dominant host-phase of As was the oxalate-extractable fraction in all soils, regardless of age or depth (Figure 2.6) and µ-XRF imaging revealed a strong spatial correlation between As and Fe (Figure 2.7). Arsenic, as arsenate, has a high sorption affinity for secondary Fe-minerals and sorbs as an inner-sphere complex (Smedley and Kinniburgh, 2002; Strawn et al., 2015). Arsenate sorption onto oxalate-extractable Fe-minerals, such as ferrihydrite, has been thoroughly investigated because of the mineral's high surface area and affinity for contaminant sorption (Jain et al., 1999; Vitre et al., 1991b; Waychunas et al., 1996; Wilkie and Hering, 1996). In pure mineral studies, ferrihydrite can sorb ~3.02 mol of As(V) per kg^{-1} of Fe at pH 4.6 to 5 (Grafe et al., 2002, 2001; Ladeira and Ciminelli, 2004; Raven et al., 1998) whereas crystalline phases of Fe, such as goethite, sorb 0.33 mol of As(V) per kg^{-1} Fe (Grafe et al., 2001). Though As sorbs as inner-sphere complexes in both cases, differences in Fe-oxide surface area influence sorption capacities, as ferrihydrite's surface area can range from 100 – 700 m^2 g^{-1} whereas goethite and hematite have surface areas ranging from 6 - 115 m^2 g^{-1} (Barron et al., 1988; Bigham et al., 2002; Cornell and Schwertmann, 2003; Torrent et al., 1990). Although μ-XRF imaging highlights the strong positive correlation between As and Fe and chemical extractions revealed a strong dependence on amorphous phases (Figure 2.6, Figure 2.7), extrapolating measurements from pure systems to experiments with natural materials is complicated by confounding factors, and in our study, it is probable that aluminum oxides and organic carbon, among other soil components that wouldn't be detectable by the μ-XRF techniques employed, may have also contributed to As sorption at given soil properties and experimental conditions (Manning and Goldberg, 1997; Smedley and Kinniburgh, 2002; Vitre et al., 1991b).

Based on measured concentrations of oxalate- and dithionite-extractable Fe and Al in the OCR soils, as well as published As sorption capacity values for pure Fe and Al oxides, we calculated the maximum As sorption we would expect for the OCR soils. To approximate As(V) sorption onto amorphous Fe- and Al-minerals (oxalate-extractable) sorption capacities of ferrihydrite or allophane were used, and based on OCR concentrations of oxalate-extractable Fe and Al, we expect the range of As sorption to be between 0.016 – 0.085 mol of As sorbed to ferrihydrite and allophane per kg^{-1} of soil (Table 2.3) (Arai et al., 2005; Raven et al., 1998). These calculated values were well matched to our measured values of oxalate-extracted As from

As-doped soils (Figure 2.6), which ranged from 0.02 to 0.06 mol of oxalate-extractable As kg^{-1} OCR soil. In order to estimate As(V) sorption onto crystalline Fe- and Al-minerals (CBD extractable), goethite and gibbsite's sorption maxima were used, and sorption capacities were expected to range from 0.002 – 0.022 mol of As sorbed to goethite and gibbsite per kg^{-1} of soil (Table 2.3) (Grafe et al., 2001; Ladeira and Ciminelli, 2004). Measured citrate-bicarbonate-dithionite-extractable As from OCR soils (20 and 908 ky soils from a 30- and 100-cm depth; Figure 2.6) overlapped on the lower end of these calculated values, ranging from 0.002 to 0.009 mol of CBD-extractable As kg^{-1} OCR soils.

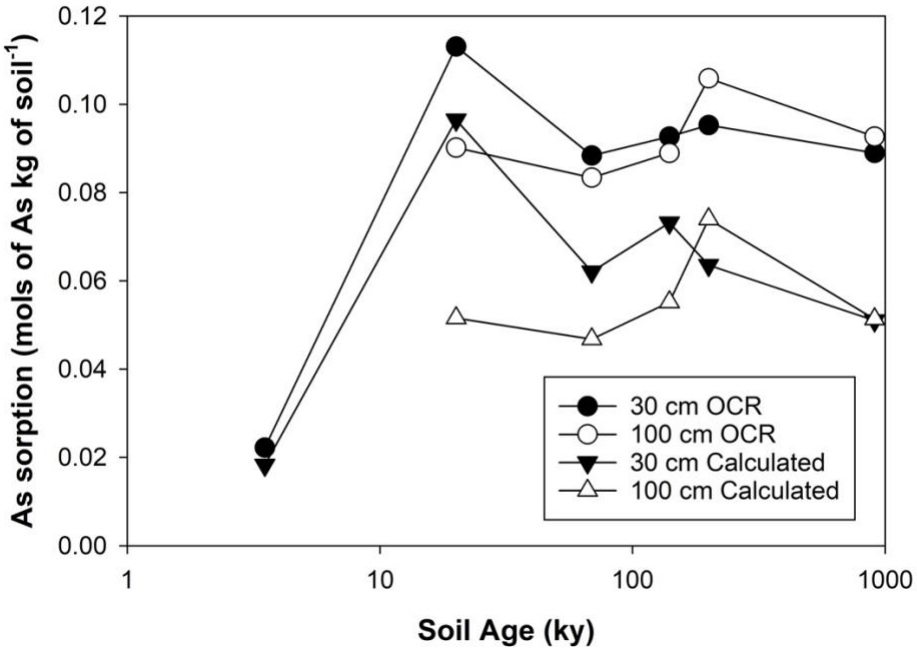

Figure 2.8. Actual and calculated As sorption onto OCR soils from 30- (black symbols) and 100-cm (white symbols) depths. Actual As sorption capacities (circles) are derived from sorption isotherm data and is also presented in Figure 2.3. Calculated As sorption capacities (triangles) were calculated using literature As(V) sorption values for ferrihydrite, allophane, goethite, and gibbsite and are based on concentration of Feo, Alo, Fed, and Ald that was presented in Lindeburg et al., 2013.

The expected sorption capacity of As(V) onto oxalate- and dithionite-extractable Fe- and Al-minerals ranged from 0.018 to 0.096 mol of As sorbed to ferrihydrite, allophane, goethite, and gibbsite per kg^{-1} of soil, while maximum As sorption capacities in OCR soils, as determined by Langmuir q_{max} values from our measured isotherms, ranged from 0.022 - 0.113 mol As per kg^{-1}

of OCR soil (Figure 2.8). In general, sorption capacities observed in OCR soil isotherms were higher than those calculated from pure minerals, which may be attributed to pedogenic ferrihydrite having a greater capacity for As sorption than synthesized ferrihydrite, additional phases – such as organic matter – contributing to As sorption, and the overall heterogeneity of soils vs. pure mineral systems (Dzombak and Morel, 1991; Hingston et al., 1971; Pierce and Moore, 1982; Smedley and Kinniburgh, 2002; Vitre et al., 1991c). Still, the order-of-magnitude agreement of measured As sorption maxima with values calculated from As sorption capacities to pure minerals highlights, in this case, a particularly strong connection between measurements from idealized and field samples.

In general, measured (Figure 2.6) and calculated (Table 2.3) As sorption onto oxalate-extractable phases was frequently over 10 times the As sorption to CBD-extractable phases, which highlights the disproportionate influence of amorphous phases over crystalline phases in governing contaminant sorption. Moreover, differences in phases controlling As sorption, as demonstrated by oxalate vs. CBD extractions, demonstrate how stage of pedogenesis, which creates different quantities and ratios of amorphous and crystalline phases, is a critical driver of contaminant reactivity.

Amorphous Fe and Al concentrations that ultimately govern contaminant mobility in OCR soils are maintained by the rates of primary mineral weathering and the proportion that are transformed towards crystalline-oxide phases (Bigham et al., 2002; Hingston et al., 1971; Smedley and Kinniburgh, 2013). Crystalline Fe- and Al-oxide minerals sorb contaminants by an order of magnitude lower than their amorphous precursors. Our findings suggest that the concentration of amorphous phases, which can be in a roughly steady state balanced by rates of their production from primary mineral weathering and ripening-driven destruction, is the key factor controlling contaminant retention, and this value is therefore critical for assessing contaminant availability and threats to environmental quality within a given soil system. Future research should be directed towards understanding Fe- and Al-oxide genesis in varying soil forming conditions and environments that ultimately govern contaminant reactivity in the subsurface.

Table 2.3. Arsenic sorption capacities of OCR soils compared to estimated amorphous and crystalline Fe and Al sorption capacities calculated from pure mineral isotherms for soils as a function of age and depth. Abbreviations used in the table: extractable (Extr.), dithionite (Dith.), calculated (Calc.), and oxalate (Ox.)

Sample Name	Dith. Extr. Fe (mol kg^{-1})	Ox. Extr. Fe (mol kg^{-1})	Dith. Extr. Al (mol kg^{-1})	Ox. Extr. Al (mol kg^{-1})	Calc. As sorption for ferrihydrite and allophane[1] (mol kg^{-1})	Calc. As Sorption for goethite and gibbsite[2] (mol kg^{-1})	Total Calc. As sorption[3] (mol kg^{-1})	OCR q_{max} (As mol kg^{-1})
3.5 ky 30 cm	0.0948	0.0572	0.0667	0.0778	0.0161	0.0023	0.0183	0.0222
20 ky 30 cm	0.4100	0.2238	0.5077	0.5782	0.0852	0.0113	0.0965	0.1131
69 ky 30 cm	0.5210	0.0931	0.4484	0.4151	0.0498	0.0124	0.0621	0.0883
140 ky 30 cm	0.5962	0.1307	0.4225	0.4521	0.0592	0.0140	0.0732	0.0926
200 ky 30 cm	0.8093	0.0948	0.4744	0.3669	0.0461	0.0174	0.0636	0.0953
908 ky 30 cm	0.9668	0.0555	0.3817	0.2668	0.0313	0.0197	0.0510	0.0889
20 ky 100 cm	0.3831	0.1020	0.3039	0.3076	0.0343	0.0125	0.0468	0.0901
69 ky 100 cm	0.5711	0.0608	0.3113	0.2928	0.0394	0.0157	0.0552	0.0834
140 ky 100 cm	0.7430	0.0895	0.3484	0.2965	0.0510	0.0229	0.0740	0.0889
200 ky 100 cm	1.0760	0.0823	0.3409	0.4521	0.0294	0.0219	0.0513	0.1059

[1] Calculated As sorption capacity for oxalate extractable Fe and Al are based on concentrations extracted from OCR soils that are presented in Lindeburg et al 2013. Pure mineral sorption isotherms of As(V) and ferrihydrite (Raven et al 1998) or allophane (Arai et al 2005; Andersen et al 1976) were used to estimate As sorption of amorphous oxides.

[2] Calculated As sorption capacity for dithionite extractable Fe and Al are based on concentrations extracted from OCR soils that are presented in Lindeburg et al 2013. Pure mineral sorption isotherms of As(V) and goethite (Grafe et al 2001) or gibbsite (Ladiera et al 2004) were used to estimate As sorption of crystalline oxides.

[3] Calculated sorption capacities are the sum of predicted As(V) sorption onto ferrihydrite, allophane, goethite, and gibbsite.

Sample Name	Dith. Extr. Fe (mol kg^{-1})	Ox. Extr. Fe (mol kg^{-1})	Dith. Extr. Al (mol kg^{-1})	Ox. Extr. Al (mol kg^{-1})	Calc. As sorption for ferrihydrite and allophane[4] (mol kg^{-1})	Calc. As Sorption for goethite and gibbsite[5] (mol kg^{-1})	Total Calc. As sorption[6] (mol kg^{-1})	OCR q_{max} (As mol kg^{-1})
908 ky 100 cm	1.0957	0.0644	0.3298	0.2260	0.0161	0.0023	0.0183	0.0926

CONCLUSION

Soil weathering processes influence the sustainability and quality of soil and water resources in the environment. In using As removal from solution as a proxy for soil-contaminant reactivity in soils from a chronosequence in the Oregon Coast Range (3.5 to 908 ky from a 30- and 100-cm depth) we highlight the strong dependence on short-range-order minerals that disproportionally govern contaminant fate in our environment. Chemical extractions and μ-XRF spectroscopy revealed the strong dependence on amorphous solid-host phases and the strong spatial correlation between As and Fe, respectively. Arsenic sorption capacities are most greatly governed by the concentrations of amorphous (oxy)hydroxide mineral phases, even when crystalline oxides and oxyhydroxide minerals are abundant. The concentration of amorphous minerals is balanced by rates of their production from weathering of primary minerals and rates of loss from ripening to more crystalline phases, which accumulate through pedogenesis. This

[4] Calculated As sorption capacity for oxalate extractable Fe and Al are based on concentrations extracted from OCR soils that are presented in Lindeburg et al 2013. Pure mineral sorption isotherms of As(V) and ferrihydrite (Raven et al 1998) or allophane (Arai et al 2005; Andersen et al 1976) were used to estimate As sorption of amorphous oxides.

[5] Calculated As sorption capacity for dithionite extractable Fe and Al are based on concentrations extracted from OCR soils that are presented in Lindeburg et al 2013. Pure mineral sorption isotherms of As(V) and goethite (Grafe et al 2001) or gibbsite (Ladiera et al 2004) were used to estimate As sorption of crystalline oxides.

[6] Calculated sorption capacities are the sum of predicted As(V) sorption onto ferrihydrite, allophane, goethite, and gibbsite.

knowledge can assist in improving models for predicting CZ processes that govern the sustainability of soil and water quality, and future work could aim to understand the influences of different environments on soil weathering, in order to ultimately determine contaminant fate in the environment.

SOURCES OF FINANCIAL SUPPORT

This work was supported by the National Institute of Health through the National Institute of Environmental Health Sciences under Grant No. NIH-5P42ES031007-02 and the University of Oregon. Use of the Stanford Synchrotron Radiation Lightsource, SLAC National Accelerator Laboratory, is supported by the U.S. Department of Energy, Office of Science, Office of Basic Energy Sciences under Contract No. DE-AC02-76SF00515.

ACKNOWLEDGMENTS

We thank Markus Koeneke, Fatai Balogun, Katie Fisher, and Jason John for support in developing and conducting this research; Josh Roering for the chronosequence soils; Owen Duckworth and Sam Webb for assistance in gathering μ-XRF data at the Stanford Synchrotron Radiation Lightsource; and Chris Russo and Jesse Muratli at Oregon State University for assistance in gathering ICP-OES data.

SUPPLEMENTAL MATERIALS FOR CHAPTER II.

Supplemental Tables

SI Table 2.1. Soil characterization data, reproduced from Lindeburg et al. 2013.

Depth (cm)	Soil Horizon	Age (ky)	Bulk Density (g cm^3)	Sand (%)	Silt (%)	Clay (%)	CEC	Carbon (%)	Elevation (m)	pH
30	C2	3.5	1.14	90.4	6	3.6	15.7	0.5	85.5	5.7
30	Bw1	20	0.93	30.3	45.3	24.4	38.1	4.17	89	4.8
30	Bt1	69	1.25	32	29.2	38.7	17.6	1.08	94.3	5
30	Bw	140	1	31.1	31.6	37.3	20.7	1.72	106.9	4.8
30	Bw1	200	1.04	8.8	38.6	42.7	23.1	2.68	117.6	5.1
30	AB	908	1.1	15.4	22.2	62.3	21.3	2.33	248.9	5.2
100	BC	20	1.15	24.4	41.2	34.5	24.4	0.45	89	4.9
100	Bt3	69	1.19	30	25.9	44.1	15.2	0.32	94.3	5.1
100	2Bt2	140	1.31	29.6	26.5	43.9	15.3	0.35	106.9	5.2
100	Bt1	200	1.21	19.1	24.8	45.7	17.7	0.74	117.6	5.1
100	Bt2	908	1.03	13.6	18.9	67.5	17.4	0.43	248.9	4.8

SI Table 2.2. Soil classification of each soil terrace, reproduced from Lindeburg et al., 2013.

Soil Age (ky)	USDA Soil Taxonomy	Series Name
3.5	Fine-loamy, isotic, mesic Typic Humudepts	Meda
20	Fine-loamy, isotic, mesic Typic Humudepts	Meda
69	Fine-loamy, isotic, mesic Typic Humudepts	Meda
140	Fine, isotic, mesic Humic Dystrudepts	Blachly
200	Fine-loamy, isotic, mesic Andic Humudepts	Preacher
908	Fine-loamy, isotic, mesic Andic Humudepts	Preacher

SI Table 2.3. Crystalline and amorphous Fe- and Al-oxides in Oregon Coast Range soils. Reproduced from Lindeburg et al., 2013.

Age (ky)	Crystalline Fe (dithionite extractable) (mg kg^{-1})	Amorphous Fe (oxalate extractable) (mg kg^{-1})	Crystalline Al (dithionite extractable) (mg kg^{-1})	Amorphous Al (oxalate extractable) (mg kg^{-1})
3.5	5300	3200	1800	2100
20	22900	12500	13700	15600
69	29100	5200	12100	11200
140	33300	7300	11400	12200
200	45200	5300	12800	9900
908	54000	3100	10300	7200
20	21400	5700	8200	8300
69	31900	3400	8400	7900
140	41500	5000	9400	8000
200	60100	4600	9200	12200
908	61200	3600	8900	6100
3.5	5300	3200	1800	2100

SI Table 2.4. Langmuir model data for each soil terrace from a 30-cm depth.

Soil Terrace Age (ky)	q_{max} (mg kg^{-1})	m - Linear	$K_{Langmuir}$	b - Linear
3.5	1666.66	0.0006	0.0078	0.0767
20	8474.58	1.18E-04	0.0098	0.0121
69	6622.52	1.51E-04	0.0113	0.0134
140	6944.44	1.44E-04	0.0073	0.0198
200	7142.86	1.40E-04	0.0109	0.0128
908	6666.67	1.50E-04	0.0080	0.0188

SI Table 2.5. Langmuir model data for each soil terrace from a 100-cm depth.

Soil Terrace Age (ky)	q_{max} (mg kg^{-1})	m - Linear	$K_{Langmuir}$	b - Linear
20	6756.76	1.48E-04	0.0116	0.0128
69	6250.00	1.60E-04	0.0171	0.0094
140	6666.67	1.50E-04	0.0228	0.0066
200	7936.51	1.26E-04	0.0378	0.0033
908	6944.44	1.44E-04	0.0226	0.0064

Supplemental Figures

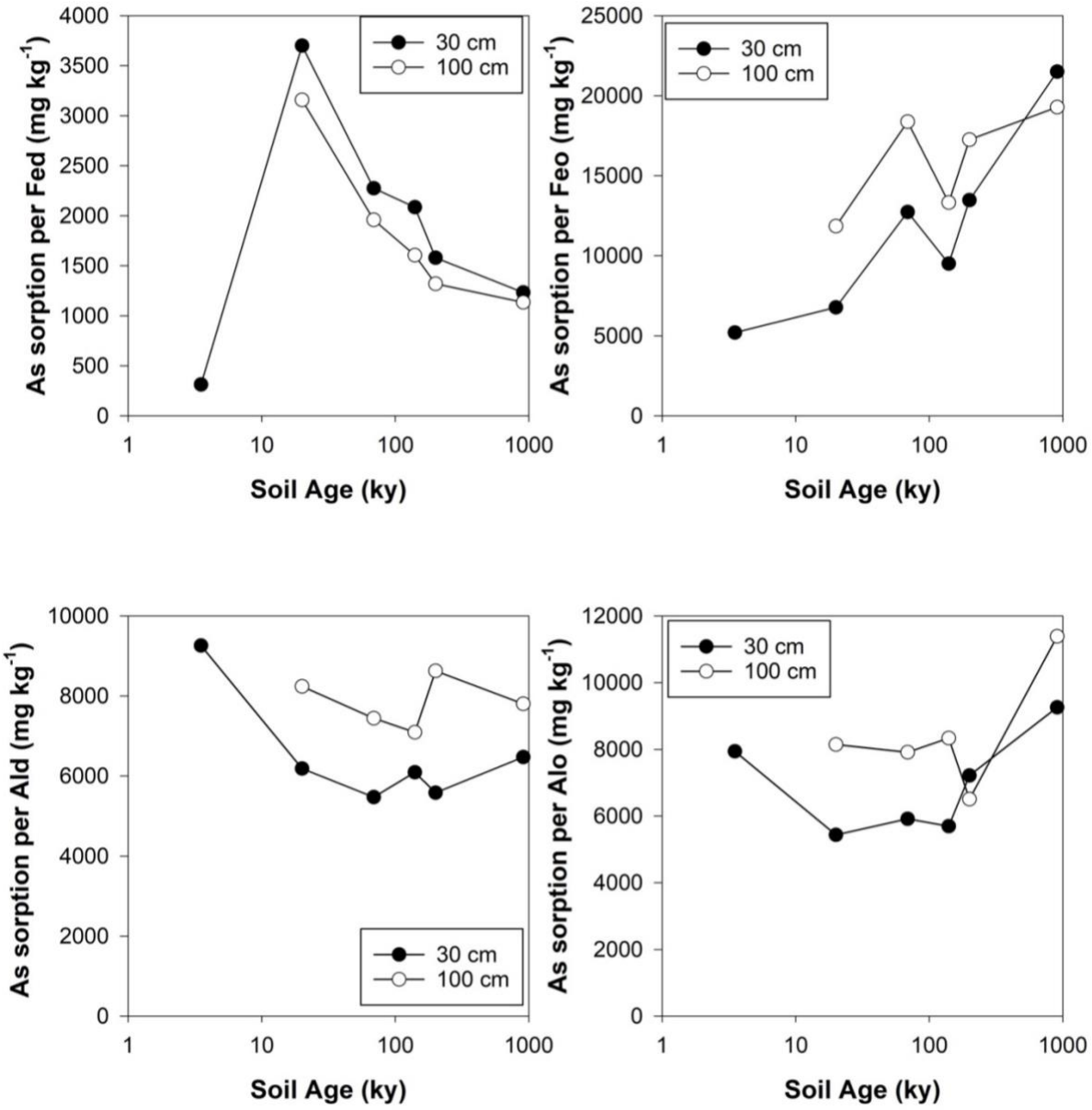

SI Figure 2.1. (Upper Left) Maximum As sorption capacity per crystalline Fe (CBD extractable) for 30- and 100-cm soils across the OCR. (Upper right) Maximum As sorption capacity per amorphous Fe (oxalate extractable) for 30- and 100-cm soils across the OCR. (Lower left) Maximum As sorption capacity per crystalline Al (CBD extractable) for 30- and 100-cm soils across the OCR. (Lower right) Maximum As sorption capacity per amorphous Al (oxalate extractable) for 30- and 100-cm soils across OCR. Oxalate- and CBD-extractable Fe and Al data were provided by Lindeburg et al., 2013.

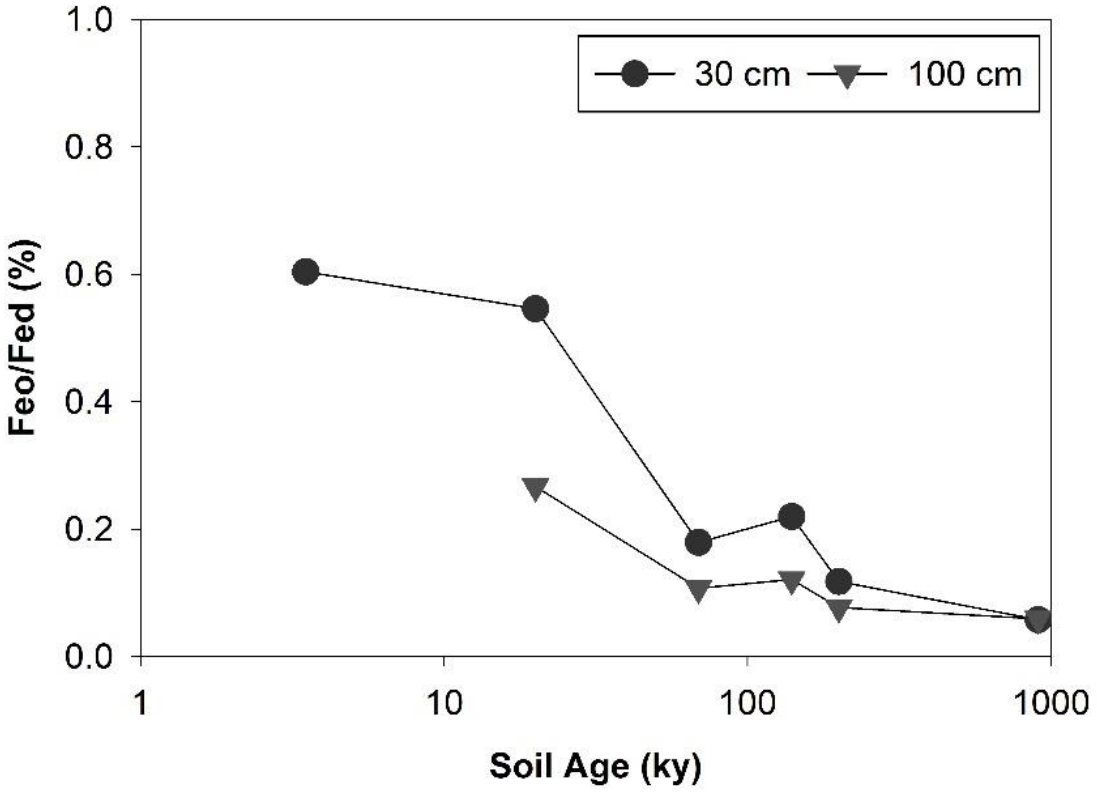

SI Figure 2.2. Ratio of Feo (oxalate-extractable Fe) and Fed (dithionite extractable Fe) in 30- and 100-cm soils as a function of soil age.

REFERENCES

Almond, P., Roering, J., Hales, T.C., 2007. Using soil residence time to delineate spatial and temporal patterns of transient landscape response. J Geophys Res Earth Surf 112. https://doi.org/10.1029/2006JF000568

Aniku, J.R.F., Singer, M.J., 1990. Pedogenic Iron Oxide Trends in a Marine Terrace Chronosequence. Soil Science Society of America Journal 54, 147–152. https://doi.org/10.2136/sssaj1990.03615995005400010023x

Arai, Y., Sparks, D.L., Davis, J.A., 2005. Arsenate adsorption mechanisms at the allophane - Water interface. Environ Sci Technol 39, 2537–2544. https://doi.org/10.1021/es0486770

Barron, V., Herruzo, M., Torrent, J., 1988. Phosphate Adsorption by Aluminous Hematites of Different Shapes. Soil Science Society of America Journal 52, 647–651. https://doi.org/10.2136/sssaj1988.03615995005200030009x

Bigham, J.M., Fitzpatrick, R.W., Schulze, D.G., 2002. Chapter 10 Iron Oxides. Soil Mineralogy with Environmental Applications. 323–376.

Bowell, R.J., 1994. Sorption of arsenic by iron oxides and oxyhydroxides in soils. Applied Geochemistry 9, 279–286. https://doi.org/10.1016/0883-2927(94)90038-8

Brantley, S.L., Goldhaber, M.B., Vala Ragnarsdottir, K., 2007. Crossing disciplines and scales to understand the critical zone. Elements 3, 307–314. https://doi.org/10.2113/gselements.3.5.307

Brantley, S.L., McDowell, W.H., Dietrich, W.E., White, T.S., Kumar, P., Anderson, S.P., Chorover, J., Ann Lohse, K., Bales, R.C., Richter, D.D., Grant, G., Gaillardet, J., 2017. Designing a network of critical zone observatories to explore the living skin of the terrestrial Earth. Earth Surface Dynamics 5, 841–860. https://doi.org/10.5194/esurf-5-841-2017

Brown, G.E., Foster, A.L., Ostergren, J.D., 1999. Mineral surfaces and bioavailability of heavy metals: A molecular-scale perspective.

Buol, S.W., Southard, R.J., Graham, R.C., P.A., M., 2011. Soil Genesis and Classification, Sixth. ed. Wiley-Blackwell.

Chorover, J., Kretzschmar, R., Garcia-pichel, F., Sparks, D.L., 2007. Soil Biogeochemical Processes within the Critical Zone. Elements 3, 321–326.

Cornell, R.M., Schwertmann, U., 2003. The Iron Oxides, 2nd ed. Wiley. https://doi.org/10.1002/3527602097

Dixit, S., Hering, J.G., 2003. Comparison of arsenic(V) and arsenic(III) sorption onto iron oxide minerals: Implications for arsenic mobility. Environ Sci Technol 37, 4182–4189. https://doi.org/10.1021/es030309t

Duckworth, O.W., Polizzotto, M.L., Thompson, A., 2022. tackle soil contaminants. https://doi.org/10.3389/fenvs.2022.981607.Bringing

Dzombak, D., Morel, F., 1991. Surface Complexation Modeling: Hydrous Ferric Oxide. John Wiley, New York.

Giménez, J., Martínez, M., de Pablo, J., Rovira, M., Duro, L., 2007. Arsenic sorption onto natural hematite, magnetite, and goethite. J Hazard Mater 141, 575–580. https://doi.org/10.1016/j.jhazmat.2006.07.020

Grafe, M., Eick, M.J., Grossl, P.R., 2001. Adsorption of Arsenate (V) and Arsenite (III) on Goethite in the Presence and Absence of Dissolved Organic Carbon. Soil Science Society of America Journal 65, 1680–1687. https://doi.org/10.2136/sssaj2001.1680

Grafe, M., Eick, M.J., Grossl, P.R., Saunders, A.M., 2002. Adsorption of Arsenate and Arsenite on Ferrihydrite in the Presence and Absence of Dissolved Organic Carbon. Environmental Quality 1123, 1115–1123.

Heller, P.L., Dickinson, W.R., 1985. Submarine ramp facies model for delta-fed, sand-rich turbidite systems. Am. Assoc. Pet. Geol., Bull.; (United States) 69:6.

Heller, P.L., Peterman, Z.E., O'Neil, J.R., Shafiqullah, M., 1985. Isotopic provenance of sandstones from the Eocene Tyee Formation, Oregon Coast Range. Geol Soc Am Bull 96, 770–780. https://doi.org/10.1130/0016-7606(1985)96<770:IPOSFT>2.0.CO;2

Hingston, F.J., Posner, " A M, Quirk, J.P., Hpoi-, +, 1971. Competitive Adsorption of Negatively Charged Ligands on Oxide Surfaces.

Hunter, B.D., Roering, J.J., Almond, P.C., Chadwick, O.A., Polizzotto, M.L., Silva, L.C.R., 2023. Pedogenic pathways and deep weathering controls on soil organic carbon in Pacific Northwest forest soils. Geoderma 436. https://doi.org/10.1016/j.geoderma.2023.116531

Jain, A., Raven, K.P., Loeppert, R.H., 1999. Arsenite and arsenate adsorption on ferrihydrite: Surface charge reduction and net OH- release stoichiometry. Environ Sci Technol 33, 1179–1184. https://doi.org/10.1021/es980722e

Keon, N.E., Swartz, C.H., Brabander, D.J., Harvey, C., Hemond, H.F., 2001. Validation of an arsenic sequential extraction method for evaluating mobility in sediments. Environ Sci Technol 35, 2778–2784. https://doi.org/10.1021/es001511o

Ladeira, A.C.Q., Ciminelli, V.S.T., 2004. Adsorption and desorption of arsenic on an oxisol and its constituents. Water Res 38, 2087–2094. https://doi.org/10.1016/j.watres.2004.02.002

Lawrence, C.R., Harden, J.W., Xu, X., Schulz, M.S., Trumbore, S.E., 2015. Long-term controls on soil organic carbon with depth and time: A case study from the Cowlitz River Chronosequence, WA USA. Geoderma 247–248, 73–87. https://doi.org/10.1016/j.geoderma.2015.02.005

Lilienfein, J., Qualls, R.G., Uselman, S.M., Bridgham, S.D., 2004. Adsorption of Dissolved Organic and Inorganic Phosphorus in Soils of a Weathering Chronosequence. Soil Science Society of America Journal 68, 620–628. https://doi.org/10.2136/sssaj2004.6200

Lindeburg, K.S., Almond, P., Roering, J.J., Chadwick, O.A., 2013. Pathways of soil genesis in the Coast Range of Oregon, USA. Plant Soil 367, 57–75. https://doi.org/10.1007/s11104-012-1566-z

Mamindy-Pajany, Y., Hurel, C., Marmier, N., Roméo, M., 2009. Arsenic adsorption onto hematite and goethite. Comptes Rendus Chimie 12, 876–881. https://doi.org/10.1016/j.crci.2008.10.012

McFadden, L.D., Hendricks, D.M., 1985. Changes in the content and composition of pedogenic iron oxyhydroxides in a chronosequence of soils in southern California. Quat Res 23, 189–204. https://doi.org/10.1016/0033-5894(85)90028-6

McKeague JA, Brydon JE, Miles NM, 1971. Differentiation of Forms of Extractable Iron and Aluminum in Soils 35, 33–38. https://doi.org/10.2136/sssaj1971.03615995003500010016x

Mehra, O.P., Jackson, M.L., 1958. Iron Oxide Removal from Soils and Clays by a Dithionite-Citrate System Buffered with Sodium Bicarbonate. Clays Clay Miner 7, 317–327. https://doi.org/10.1346/ccmn.1958.0070122

Ona-Nguema, G., Morin, G., Juillot, F., Calas, G., Brown, G.E., 2005. EXAFS analysis of arsenite adsorption onto two-line ferrihydrite, hematite, goethite, and lepidocrocite. Environ Sci Technol 39, 9147–9155. https://doi.org/10.1021/es050889p

Peel, H.R., Balogun, F.O., Bowers, C.A., Miller, C.T., Obeidy, C.S., Polizzotto, M.L., Tashnia, S.U., Vinson, D.S., Duckworth, O.W., 2022. Towards Understanding Factors Affecting Arsenic, Chromium, and Vanadium Mobility in the Subsurface. Water (Switzerland) 14, 1–36. https://doi.org/10.3390/w14223687

Pierce, M.L., Moore, C.B., 1982. Adsorption of arsenite and arsenate on amorphous iron hydroxide, Dater Res.

Raven, K.P., Jain, A., Loeppert, R.H., 1998. Arsenite and arsenate adsorption on ferrihydrite: Kinetics, equilibrium, and adsorption envelopes. Environ Sci Technol 32, 344–349. https://doi.org/10.1021/es970421p

Rechberger, M. v., Roberti, D., Phillips, A., Zehetner, F., Keiblinger, K.M., Kandeler, E., Gerzabek, M.H., 2021. Cadmium retention and microbial response in volcanic soils along

gradients of soil age and climate on the Galápagos Islands. J Environ Qual 50, 1233–1245. https://doi.org/10.1002/jeq2.20275

Rechberger, M. v., Zehetner, F., Candra, I.N., Gerzabek, M.H., 2020. Impact of soil development on Cu sorption along gradients of soil age and moisture on the Galápagos Islands. Catena (Amst) 189, 104507. https://doi.org/10.1016/j.catena.2020.104507

Rechberger, M. V., Zehetner, F., Candra, I.N., Gerzabek, M.H., 2020. Impact of soil development on Cu sorption along gradients of soil age and moisture on the Galápagos Islands. Catena (Amst) 189, 104507. https://doi.org/10.1016/j.catena.2020.104507

Ryu, I.-C., 2003. Petrography, diagenesis and provenance of Eocene Tyee Basin sandstones, southern Oregon Coast Range: New view from sequence stratigraphy. The Island Arc 12, 398–410.

Schulz, M.S., Vivit, D., Schulz, C., Fitzpatrick, J., White, A., 2010. Biologic Origin of Iron Nodules in a Marine Terrace Chronosequence, Santa Cruz, California. Soil Science Society of America Journal 74, 550–564. https://doi.org/10.2136/sssaj2009.0144

Shoji, S., Dahlgren, R., Nanzyo, M., 1993. Chapter 3 Genesis of Volcanic Ash Soils. Developments in Soil Science 21, 37–71. https://doi.org/10.1016/S0166-2481(08)70264-2

Smedley, P.L., Kinniburgh, D.G., 2002. A review of the source, behaviour and distribution of arsenic in natural waters. Applied Geochemistry. https://doi.org/10.1016/S0883-2927(02)00018-5

Snavely, P., Wagner, H., MacLeod, N., 1964. Rhythmic-bedded Eugeosynclinal Deposits of the Tyee Formation, Oregon Coast Range. D.F. Merriam, ed., Kansas Geological Survey 461–480.

Strawn, D.G., Bohn, H.L., O'Connor, G.A., 2015. Soil Chemistry. John Wiley & Sons, Ltd.

Torrent, J., Barrón, V., Schwertmann, U., 1990. Phosphate Adsorption and Desorption by Goethites Differing in Crystal Morphology. Soil Science Society of America Journal 54, 1007–1012. https://doi.org/10.2136/sssaj1990.03615995005400040012x

Vitre, R. De, Belzile, N., Tessier, A., 1991a. Speciation and adsorption of arsenic on diagenetic iron oxyhydroxides. Limnol Oceanogr. https://doi.org/10.4319/lo.1991.36.7.1480

Vitre, R. De, Belzile, N., Tessier, A., 1991b. Speciation and adsorption of arsenic on diagenetic iron oxyhydroxides. Limnol Oceanogr 36, 1480–1485. https://doi.org/10.4319/lo.1991.36.7.1480

Vitre, R. De, Belzile, N., Tessier, A., 1991c. Speciation and adsorption of arsenic on diagenetic iron oxyhydroxides. Limnol Oceanogr. https://doi.org/10.4319/lo.1991.36.7.1480

Waychunas, G.A., Fuller, C.C., Rea, B.A., Davis, J.A., 1996. Wide angle X-ray scattering (WAXS) study of "two-line" ferrihydrite structure: Effect of arsenate sorption and counterion variation and comparison with EXAFS results. Geochim Cosmochim Acta 60, 1765–1781. https://doi.org/10.1016/0016-7037(96)89830-9

Webb, S.M., 2011. The MicroAnalysis Toolkit: Fluorescence Image Processing Software. https://doi.org/10.1063/1.3625338

Wilkie, J.A., Hering, J.G., 1996. Adsorption of arsenic onto hydrous ferric oxide: effects of adsorbate/adsorbent ratios and co- occurring solutes. Colloids and Surfaces 107, 97–110.

CHAPTER III: HEAT-INDUCED CHROMIUM REACTIVITY ALONG A SERPENTINE SOIL TOPOSEQUENCE IN SOUTHWESTERN OREGON

Chelsea S. Obeidy, Markus W. Koeneke, Matthew L. Polizzotto

Reproduced with permission from Obeidy, C.S., Koeneke, M.W., Polizzotto, M. L.

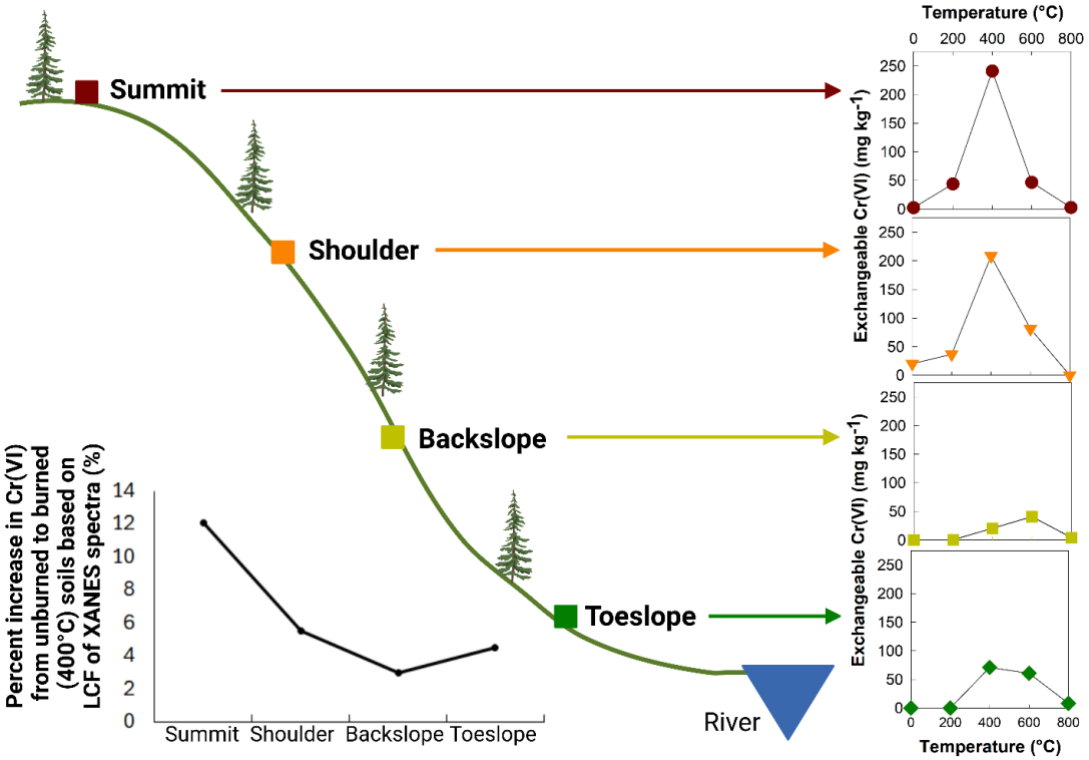

Conceptual Abstract- Conceptual diagram of the serpentine toposequence in southwestern Oregon and the Cr(VI) generated as a function of fire intensity. Maximum exchangeable Cr(VI) was generated in summit soils after burning at 400 °C and decreased down the hillslope until the toeslope, where exchangeable Cr(VI) was generated slightly afterward. At 600 °C, soils generated Cr(VI) to a lesser degree and Cr(VI) was highest at the toeslope position. Minimal Cr(VI) was detected in unburned, 200 °C, and 800 °C treated soils. XAS spectroscopy confirmed valency and general Cr(VI) abundance in 400 °C soils.

Highlights:

- Hillslope position and burn intensities impact on Cr and Fe reactivity was quantified
- Fire-induced Cr(VI) generation varied with hillslope position and burn temperature
- Reactivity of Cr(VI) was correlated with amorphous-oxide-minerals
- Release of Cr(VI) from burned soils exceeded drinking water standards
- Persistence and degree of contamination are dependent on hillslope position

INTRODUCTION

Wildfires are the most widespread ecosystem disturbance and pose a worldwide threat to human and environmental health (Bowman et al., 2009; Burton et al., 2016). Fires are not just a natural disturbance but an agricultural practice and a traditional landscape management aid. Ecosystems have evolved with fire; however, the intensity and extent of fires have changed through decades of fire suppression, urbanization, and climate change. Climate change and wildfires are predicted to have a positive feedback loop, fueling each other towards ecological disaster (Halofsky et al., 2020). There are many processes driving the increase in fire in the western U.S., and climate change has been deemed the most important due to its influence over warming-driven fuel drying (Halofsky et al., 2020). In California and Southern Oregon, climate change is expected to increase wildfire frequency and extent and decrease precipitation and snowpack. Such environmental changes threaten the security and quality of drinking water and soil resources for millions of people who live in Northern California and Southern Oregon, an already water-stressed area.

Serpentine landscapes that occur throughout California and Southern Oregon have naturally high concentrations of contaminants in their soils. The abundance of Cr found in serpentine soils is dependent on the weathering of ultramafic and serpentine bedrock. In general, serpentine weathering progresses from most weathered to least weathered: Fe-rich pyroxene > antigorite > Mg-rich lizardite > Al-rich lizardite (Baumeister et al., 2015). Across a hillslope, weathering products vary, and serpentine toposequences have been utilized to capture differences in pedogenic Cr concentrations as a function of hillslope position. In California, along a serpentine toposequence, weathering and primary mineral alteration were greatest at the summit position and decreased with the hillslope position (Bullard, 2005). In a Taiwanese serpentine toposequence, landscape position was the most important factor in controlling the abundance of Cr, which accumulated at the footslope position and, to a lesser degree, at the shoulder and backslope position (Cheng et al., 2011). Additionally, chromite, a common source of Cr in serpentine soils, was found to be more chemically weathered near the soil surface than at depth (Cheng et al., 2011). Differences in serpentine weathering across a hillslope highlight the variations of available Cr that can be transformed by wildfire across a landscape.

Contaminants that are naturally observed in serpentine soils pose a risk to human and environmental health. Chromium is a transition metal that exists in two main oxidation states, Cr(III) and Cr(VI), in near-surface environments, and recently, thermal alterations have been shown to influence Cr oxidation state and toxicity in post-fire landscapes (Alexakis, 2020; Allin et al., 2008; Burton et al., 2019a; Burton et al., 2019b; Campos et al., 2016; Costa et al., 2014; Pereira & Úbeda, 2010; Plumlee et al., 2007). Trivalent chromium [Cr(III)] exists as a cation that is poorly soluble and immobile in most soils, whereas Cr(VI) is a notorious cancer-causing toxin and has been detected in groundwaters associated with serpentine soils, where oxidation of Cr(III) is frequently facilitated by Mn-oxides (e.g. birnessite) (Bartlett & James, 1996a; Chrysochoou et al., 2016; Ellis et al., 2002; Jardine et al., 2011; Kim & Dixon, 2002; Kožuh et al., 2000; Landrot et al., 2010, 2012; Oze et al., 2004; Peel et al., 2022).

Fire intensity controls the mobilization of redox-sensitive metals into surface water, air, and soil (Abraham et al., 2017; Burton et al., 2019a; Johnston et al., 2019; Lopez et al., 2023; Panichev et al., 2008; Roshan & Biswas, 2023; Jovanovic et al., 2011). Minerals that host and sorb trace elements in soils are modified during a fire, and trace element availability can be enhanced (Burton et al., 2019a; Burton et al., 2019b; Lopez et al., 2023). Burton et al. 2019 have observed that in natural unpolluted soils, 35% of the Cr(III) was oxidized to Cr(VI) after heating between 200-400 ºC. In a more recent study, Lopez et al. (2023) observed that after wildfire in serpentine chapparel there was a 6.5-fold increase (200 µg kg^{-1}) in Cr(VI) after a high severtiy fire and a 3.6 times increase (63 µg kg^{-1}) Cr(VI) in the low-intensity areas when compared to controls. These results highlight the influence of burn intensity on controlling the generation of Cr(VI), which likely poses a substantial threat to human health and environmental quality across the globe (Burton, et al., 2019b). However, although changes to trace-element availability in post-fire soils have been observed, prediction of these fire-induced changes across landscapes remains complicated due to the natural spatial heterogeneity of soils and variability in fire intensities that may occur across different fire events.

This research seeks to expand our understanding of heat-induced contaminant reactivity and contaminant-reactive minerals within serpentine soils as a function of hillslope position and burn intensity. We specifically hypothesized that burned summit soils would have the greatest generation and availability of Cr(VI) as compared to lower hillslope positions due to in-situ weathering being greatest at the summit and there being more reactive minerals to release Cr into

soils. In considering burn intensity, we expected that the 600 °C treatment would generate the greatest Cr(VI) due to the dominant host phase of Cr being Cr-bearing crystalline minerals. To test these hypotheses, we utilized a serpentine soil toposequence in southwestern Oregon with naturally high concentrations of Cr and burned soils to various temperatures. We sought to quantify burn intensity and hillslope position on (1) Cr(VI) generation, mobility, and transport, (2) chromium phase associations, and (3) transformation of contaminant-reactive minerals in serpentine soils. Our findings reveal that Cr(VI) generation varied with fire intensity and hillslope position, with soils from the summit position at 400 °C generating and mobilizing the highest concentrations of Cr(VI). Hexavalent Cr decreased with hillslope position up until the toeslope position, whereafter 600 °C treated soils generated greater concentrations of Cr(VI). Reactive secondary minerals generally transformed towards more crystalline phases with increased burn intensity, and amorphous associated Fe and Cr decreased after the 400 ºC treatment with increased fire intensity. This work expands our understanding of burn intensity on contaminant transformations and their associations across a serpentine landscape that can influence soil and water quality sustainability.

MATERIALS AND METHODS

Study Site and Soil Samples

Soils from a toposequence in the Josephine ophiolite deposit were used to elucidate the influence of flame-induced Cr transformations as a function of temperature and hillslope position (Figure 3.1). The investigated soils are weathered from the northeastern Josephine ultramafic sheet with local alterations to serpentine. Josephine peridotites are part of the northern extent of the largest peridotite massif in North America, covering over 1,000 km^2 (Harper, 1984; Kumamoto et al., 2019). The specific areas of the study were within the Josephine peridotite unit, which is Jurassic-aged and predominantly serpentinized harzburgite and dunite, with the clay fraction generally consisting of montmorillonite, chlorite, and talc (Hotz, 1964). The soils were likely formed near sea level in a subtropical environment and are highly weathered and considered a laterite (oxisol) soil (John-Paul Oze, 2003). The current vegetation of the area

consists of predominantly serpentine-tolerant plants, such as manzanitas, grasses, and Jeffery pine trees that have coevolved with fire.

Surface soils (5 cm), which experience the most temperature alteration during wildfires (Lopez et al., 2023), were sampled in triplicate from 4 positions (summit, shoulder, backslope, and toeslope) along the toposequence (Figure 3.1). Each position across the toposequence was representative of the area, and triplicate samples from each position were homogenized when returned to the lab. The soil was air-dried, and material larger than 2 mm was removed. Overall, the texture of all soils collected was coarse clayey.

Heating experiment

Soils from different hillslope positions were heated in a muffle furnace to simulate the thermal impacts of fire. Soils were sieved using a brass 2-mm sieve and 10 g was then placed in 10-mL ceramic crucibles for incineration. Soils were heated in a Thermoscientific Thermolyne muffle furnace for 2 h at 200, 400, 600, and 800 ºC, simulating fires of different burn intensities and a time that can be experienced in burning landscapes (Burton et al., 2019a; Burton et al., 2019). Soils were cooled at room temperature before being subjected to chemical and spectral analyses.

Hexavalent chromium chemical extractions

Chemical extractions were conducted on soils to identify the solid-phase, exchangeable, and water-exchangeable Cr(VI) after heating. Hexavalent chromium in extracts was quantified using a modified version of US EPA Method 7196A, which utilizes 1,5-diphenyl carbazide (DPC) and employs UV-VIS for analysis. This approach has been shown to be reliable in analyzing Cr(VI). The detection limit for this method is 5 µg L^{-1} (Environmental Protection Agency, 1992).

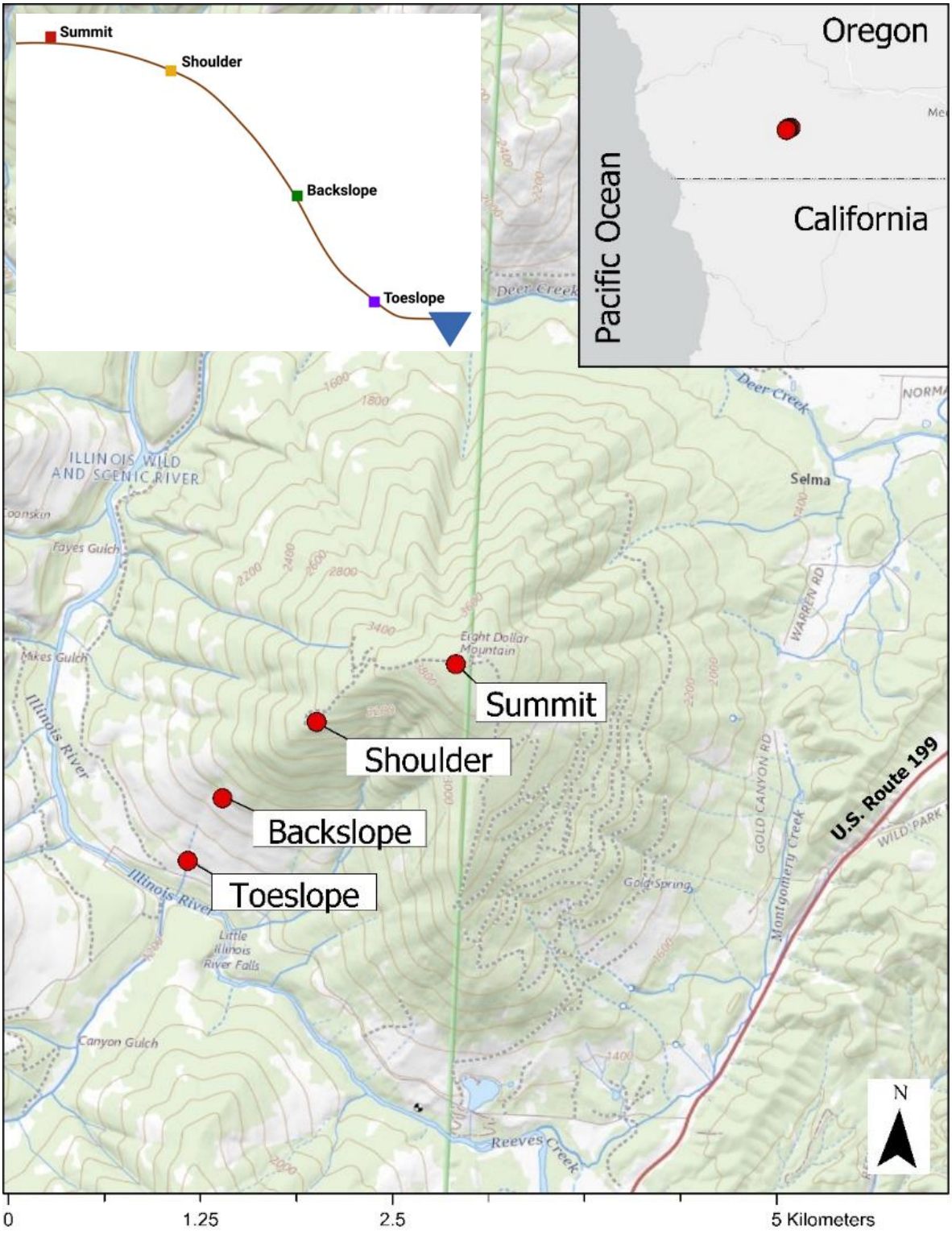

Figure 3.1. The location of the serpentine toposequence analyzed along the Illinois River in the Rogue River-Siskiyou National Forest in southwestern Oregon, USA. Triplicate soil samples were collected from each hillslope position: summit, shoulder, backslope, and toeslope.

Strong alkaline digestions (modified EPA Method 3060a) were conducted on soils to quantify the generation of solid-phase Cr(VI) in soils as a function of temperature and hillslope position. Method 3060A is a well-known procedure for quantifying solid-phase Cr(VI) without altering speciation or valency (United States Environmental Protection Agency, 1996). The procedure was modified by cutting the soil and solution in half (25 mL), and an extraction temperature of 90 ° C was maintained in a digestion block rather than a hot plate. Alkaline digestions were carried out by placing 1.25 g of soil and a solution of 0.28 M Na_2CO_3 and 0.5 M NaOH (pH of 13.2) in 50 mL polypropylene digestion vessels. Samples were swirled on a SCILOGEX MX-RD-pro shaker for 1 h before being placed into a DigiPREP and heated to 90 °C with regular swirling for 1 h. Samples were removed, cooled, filtered through a 1-µm Whatman filter paper, and then dosed with DPC.

Exchangeable Cr(VI) was extracted by 10 mM KPO_4^{2-} using a method described by Bartlett & James, 1996. One g of soil and 10 mL of 10 mM KPO_4^{2-} were placed into 15 mL HDPE centrifuge tubes and shaken for 2 h. After the 2 h extraction, samples were centrifuged at 2,000 rpm for 15 min and filtered through 1-µm Whatman filter paper and then analyzed via UV-VIS.

Water exchangeable Cr(VI) was extracted using 10 mL of a 5 mM $MgCl_2$ solution with 1 g soil in 15 mL HDPE centrifuge test tubes. Samples were shaken for 2 h and then centrifuged, filtered through a 1-µm Whatman filter paper, and analyzed via UV-VIS.

Extraction of Cr associated with amorphous oxide phases in soil

Ammonium oxalate/oxalic acid extractions were conducted to target amorphous phases that served as host phases for Cr and Fe after burn experiments. Ammonium oxalate and oxalic acid extracts target elements coprecipitated with amorphous Fe and Al (oxy)hydroxides by ligand-promoted dissolution (Keon et al., 2001). All extractions were conducted in triplicate on soils, using 0.4 g of unburned or burned soils and 40 mL of a 0.2 M ammonium oxalate/oxalic acid solution in 50-mL HDPE centrifuge tubes. Samples were vortexed then shaken in the dark on an Orbital Shaker SYC-2102A at room temperature for 2 h. After the 2 h incubation period, samples were centrifuged at 2,000 rpm for 15 min. Solutions were then filtered through 1-µm Whatman filter paper, acidified, and stored in the refrigerator. Samples were then diluted 100-

fold in 2% HNO_3 and analyzed for Cr and Fe on the Spectro-Arcos ICP-OES. The detection limits for Cr and Fe via ICP-OES are 0.6 µg L^{-1} and 0.4 µg L^{-1}, respectively.

Extraction of Cr associated with crystalline oxide phases in soil

Citrate-bicarbonate-dithionite (CBD) extractions were conducted to target trace-element contaminants associated with crystalline Fe-(oxy)hydroxides (Mehra & Jackson, 1958). Extractions were conducted on soils from each hillslope position and each temperature previously described. For each sample, 0.4 g of dosed soils were placed into 50 mL HDPE centrifuge tubes along with 20 mL of 0.3 M sodium citrate and 2.5 mL of 1 M sodium bicarbonate. Samples were heated in a hot water bath to 80 °C, and then 0.5 g of sodium dithionite was added. Samples were in the hot water bath for 30 min and shaken intermittently, after which soils were removed and centrifuged at 2,000 rpm for 15 min. Solutions were filtered using 1-µm Whatman filter paper, preserved with concentrated HNO_3, and stored in the refrigerator until analysis. Samples were diluted 100-fold in 2% HNO_3 and analyzed for Cr and Fe via ICP-OES. All analyses were conducted in triplicate.

Environmentally available Cr and Fe in soils

Strong-acid digestions were conducted to quantify "environmentally available" Cr and Fe in burned and unburned soils across the serpentine toposequence. The strong-acid digestion, EPA 3050B, is used to extract most of the environmentally available elements from a soil sample (Environmental Protection Agency, 1996). In a 50 mL DigiPREP test tube, 0.5 g of soil, 2.5 mL of 18.2 MΩ water, and 2.5 mL of 15.8 M nitric acid (HNO_3) were vortexed and left for 16 h with a watch glass. After the 16 h incubation, samples were placed into the DigiPREP digestion block at 95 °C for 15 min, removed, and then cooled for 10 min. After cooling, 2.5 mL of 15.8 M HNO_3 was added, and then samples were vortexed and placed back into the digestion block for 30 min at 95 °C; this step was repeated. After the repetition, samples in the digestion block were heated for 2 h at 95 °C. Once samples were removed and cooled, 1.5 mL of 18.2 MΩ water and 1 mL of 30% hydrogen peroxide were added to the samples. Samples were then put back into the digestion block with watch glasses and heated to 95 °C, adding 1 mL of 30% hydrogen peroxide when the effervescence stopped from the previous addition. This was done until 5 mL total of 30% hydrogen peroxide was added to each sample. Once the effervescence of the 5 mL of 30%

hydrogen peroxide stopped, samples were vortexed and heated uncovered for 2 h at 95 °C. After 2 h, samples were removed, cooled, and 2.5 mL of 12 M hydrochloric acid (HCl) was added, and then samples were reheated to 95 °C for 45 min in the digestion block. Afterward, samples were cooled and filtered through 1-µm Whatman paper into 50 mL centrifuge tubes and stored in the refrigerator. Samples were analyzed for Cr and Fe via ICP-OES. All analyses were conducted in triplicate.

X-ray absorption spectroscopy

In order to quantify how burning impacted Cr speciation and the relative abundance of Cr(VI) in soils, Cr X-ray absorption near-edge structure (XANES) was conducted on unburned soils and 400 °C-burned soils from across the serpentine toposequence. Spectroscopy at the Cr K-edge (5989 eV) was conducted at the Stanford Synchrotron Radiation Laboratory (SSRL), Stanford, California, using Beamline 4-3. A Si(220) monochromator and a Ge-detector were used, and three scans were collected for each XANES analysis. Burned and unburned soils were prepared by removing the 1.5 mm fraction and crushing the resulting material to a fine powder. Samples were loaded into an acrylic sample holder and covered with nonreactive Kapton tape. XANES spectra were collected from 5,800-6,250 eV, and triplicate spectra were averaged, baseline-corrected with a linear model, and normalized to an edge step of 1 using IFEFFIT suite of the computer program Athena. Estimates of the proportion of Cr(VI) that was generated through heating soils were accomplished by using the linear combination fitting (LCF) package in Athena (Ravel & Newville, 2005). LCF fits used unburned soils and a Cr(VI) standard ($K_2Cr_2O_4$) in order to determine the increase in Cr(VI) in burned soils from unburned soils. LCF fits were conducted over the range of 5,980 – 6,050 eV.

Synchrotron X-ray powder diffraction

Synchrotron X-ray diffraction was conducted on burned and unburned soils as a function of burn intensity and hillslope position to identify major mineral phases in samples. Analyses were conducted at SSRL on Beamline (BL) 11-3. BL 11-3 is equipped with a side-scattering Si(311) monochromator, GIXRD helium chamber, and vortex silicon drift detector. Samples were packed into Kapton capillaries (~0.7 mm) and placed into magnetic steel bases. BL 11-3 utilizes a robotic sample changing arm, and analyses were conducted at an incident energy of 17

KeV (0.729 Å). Data were analyzed via the program Match!, where background subtraction, smoothing, and peak fitting were conducted. The best merit of fit was used to determine the most abundant mineral within each soil sample (Crystal Impact, 1997).

Micro X-ray fluorescence analysis

Micro X-ray fluorescence (μ-XRF*)* was used to map the spatial distribution of Cr and associated elements. Unburned, 400 ºC, and 800 ºC soils from the summit, transition (combination of shoulder and backslope), and toeslope positions were shipped to Spectrum Petrographics Inc, Portland, OR for thin section preparation. Samples were mounted on quartz glass slides (4.5 x 2.5 cm) using EPOTEX 301 resin and then were cut and polished before analysis. Samples were analyzed at SSRL BL 2-3 in ambient air conditions and in fluorescence mode with a double Si(111) crystal monochromator to tune the X-ray beam and a Si Drift Detector (Vortex-90EX, Hitachi) for data collection. The size of the X-ray beam was focused to 5-μm diameter, and the energy at which maps were generated was 10 KeV. Data processing and visualization were conducted using SMAK (Webb, 2011).

Multi-energy XRF mapping was conducted to observe the spatial distribution of Cr(VI) in unburned, 400 ºC, and 800 ºC soils from the summit, transition (combination of shoulder and backslope), and toeslope soils. Chromium speciation maps of each distinct energy were generated at 5,989, 6,003, and 6,010 eV, energies characteristic of Cr(VI), Cr(III), and total Cr, respectively (Landrot et al., 2012; Liu et al., 2019; Lopez et al., 2023). For each image, edge removal and dead pixels were removed then we took an inverse-binary threshold of approximately 1.69 %, which removes intensities of less than 1.69 % as background in the mapped region.

Chromium μ-XANES analysis was conducted on spots of interest to confirm the valency of Cr. Calibration was conducted using a potassium chromate (K_2CrO_4) standard and by setting the position of the first maximum of spectra in the first derivative to 5,989 eV. We acquired Cr μ-XANES spectra from −230 to 270 eV around the Cr K-edge, and spectral scans were collected in duplicate. As described above, XANES spectra were calibrated, averaged, and aligned using ATHENA software packages (Ravel & Newville, 2005).

Soil column-flow experiments

Soil column experiments were conducted on unburned and burned (400 ° C) soils from each hillslope position (summit, shoulder, backslope, toeslope) to quantify the transport of Cr, under flow conditions. Dried soils were weighed out and packed into columns in duplicate with regular tapping to ensure settling. Experimentation lasted a week, with ~0.4 L of rainwater solution flowing through columns, a volume intended to replicate more than half of the annual precipitation for the field area (annual precipitation ~150 cm; NOAA), given the cross-sectional area of the column soils. After flow experiments were terminated, soils were removed, air-dried, and subjected to solid-phase analyses.

Column experiments were conducted using borosilicate-glass chromatography columns (2.5 x 10 cm Econon-Column BIORAD) fitted with polypropylene and polyethylene tubing. A fixed porous polymer filter was located at the bottom of each column. Each column also had 5 mm of glass wool, 5 mm of sand, and 5 mm of glass wool at each end to ensure an even distribution flow. Column connections were glued to reduce increasing pressure, which ruptured columns during a pilot experiment. A peristaltic pump (Watson Marlow, 323) was used to pump rainwater solution through soil columns, and Watson-Marlow manifold tubing (internal width of 0.25 mm) was used to transport the solution into columns. Column experiments were conducted in duplicate.

The rainwater solution used throughout the column experiment was designed to replicate the atmospheric water of western Oregon. The composition of the rainwater was chosen based on the atmospheric analysis of water in a nearby region (Bormann et al., 1989). The rainwater solution consisted of 1.75 mg L^{-1} of NaCl, 0.8 mg L^{-1} of $MgSO_4^{2-}$, and 0.44 g L^{-1} of KBr, the last of which was added as a conservative tracer. The pH of the rainwater solution was then adjusted to 4.88 before experimentation began.

Soil column effluent was collected throughout the experiment in order to quantify metal transport from unburned and burned (400 °C) soil columns. Effluent was collected every 4 h for 168 h. The collected solutions were filtered through a 1-µm Whatman filter paper, pH was measured (Orion STAR), then 1 mL of sample was used for Cr(VI) analysis via UV-VIS (as described above). The remaining solution from each sampling time was acidified and refrigerated until analysis via ICP-OES (as described above). Samples were analyzed for Cr and

Fe with a blank every 25 samples to ensure quality control. All samples were analyzed in triplicate.

Soil organic carbon

Soil organic carbon was analyzed for each hillslope position and burn intensity. Soil organic carbon was analyzed using a Fisher Scientific FlashSmart Elemental Analyzer. Sample preparation was conducted by encapsulating 30 mg of soil into tin capsules (4 x 7 mm). A soil reference was analyzed every 10 samples, and a standard was run every 20 samples for quality control and to monitor instrumental drift. All samples were analyzed in duplicate and the variability in C concentration between replicates was less than < 0.5%.

RESULTS

Cr(VI) generation in soils as a function of hillslope position and burn intensity

Water-extracted (5 mM $MgCl_2$) Cr(VI) as a function of hillslope position and burn temperature is presented in Figure 3.2A and SI Table 3.1. Unburned and 200 °C treated soils had no detectable Cr(VI) in samples, regardless of hillslope position. The highest concentration of water-extracted Cr(VI) was in soils from the 400 ºC treatment from the shoulder-slope position (132.9 mg kg^{-1}), followed by soils from the toeslope (70.9 mg kg^{-1}). Soils from the 600 ºC treatment had the highest water-exchangeable Cr in soils from the summit position (66.4 mg kg^{-1}), followed by the shoulder slope (64.9 mg kg^{-1}), then the toeslope (60.6 mg kg^{-1}). Soils from the 800 °C treatment had the highest Cr(VI) generated in soils from the summit position (8.8 mg kg^{-1}), followed by soils from the toeslope (8.1 mg kg^{-1}) and backslope (5.3 mg kg^{-1}) positions.

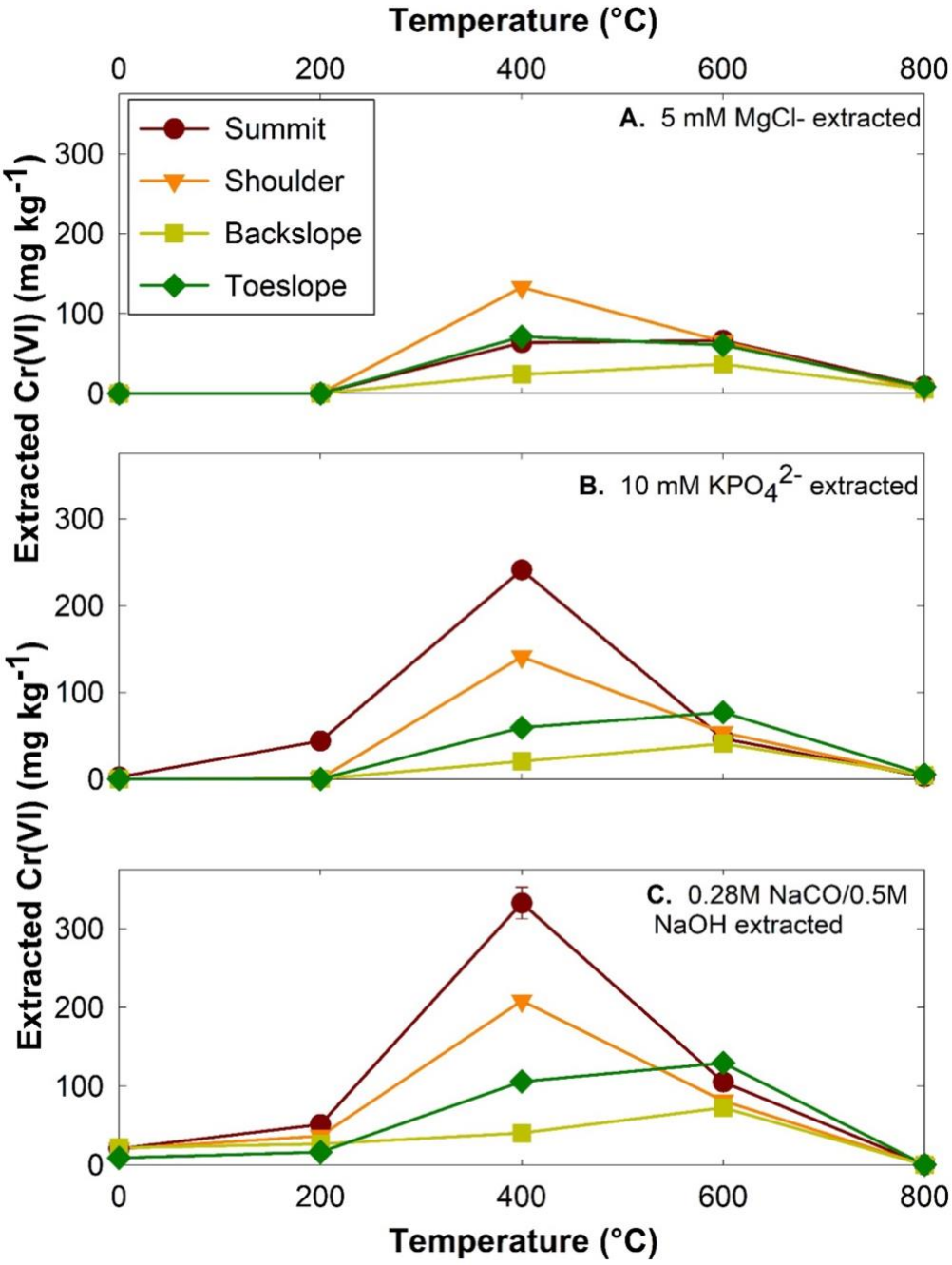

Figure 3.2. Hexavalent Cr was extracted from serpentine soils from different positions across the toposequence (summit, shoulder, backslope, and toeslope) after heating to a suite of temperatures. (A) water-extractable Cr(VI) (5 mM $MgCl^2$), (B) exchangeable Cr(VI) (10 mM KPO_4^{2-}), and (C) solid-phase Cr(VI) (0.28 M NaCO/0.5 M NaOH; EPA 3060A). Data points represent averages from triplicate samples. Error bars represent standard error of triplicate measurements; in some cases, error bars are smaller than symbols.

Exchangeable Cr(VI) extracted via 10 mM PO_4^{2-} for each hillslope position and temperature treatment are presented in Figure 3.2B and SI Table 3.1. Unburned soils did not have any detectable Cr(VI) except for soils from the summit position (2.2 mg kg^{-1}). Across the experiments, the highest concentration of exchangeable Cr(VI) was found in summit soils from the 400 °C treatment (241.2 mg kg^{-1}), followed by the 400 °C shoulder-slope soil (141.0 mg kg^{-1}). Exchangeable Cr(VI) in soils from the toeslope position (59.2 mg kg^{-1}) was greater than the backslope (20.4 mg kg^{-1}) in the 400 °C treatment. Exchangeable Cr(VI) generated in the toeslope and backslope positions were greater in the 600 °C treatment than in the 400 °C treatment for the backslope and toeslope positions. In the 600 °C treatment, toeslope soils generated the most Cr(VI) (76.9 mg kg^{-1}), followed by the shoulder-slope position (53.7 mg kg^{-1}). Soils from the 200 °C treatment from the shoulder-slope, backslope, and toeslope positions generated less than 1 mg kg^{-1} of Cr(VI), while the summit position generated 43.8 mg kg^{-1} of Cr(VI). Soils from the 800 °C treatment had negligible exchangeable Cr(VI) (5.4 – 2.6 mg kg^{-1}), regardless of hillslope position.

Solid-phase Cr(VI) extracted from each hillslope position and temperature treatment are presented in Figure 3.2C and SI Table 3.3. Unburned soils had similar concentrations of Cr(VI) in the summit, shoulder, and backslope positions (20.1 mg kg^{-1}), while the toeslope position had 8.9 mg kg^{-1} of Cr(VI). The highest concentration of solid-phase Cr(VI) was present in soils from the summit position 400 °C treatment (332.6 mg kg^{-1}) followed by the shoulder-slope position (208.4 mg kg^{-1}). The 600 °C treatment had the highest concentration of solid-phase Cr(VI) generated in soils from the toeslope position (129.4 mg kg^{-1}), followed by the summit position (105.13 mg kg^{-1}). In the 200 °C treatment, Cr(VI) decreased with the hillslope position from the summit (51.3 mg kg^{-1}) to the toeslope (16.1 mg kg^{-1}). Soils from the 800 °C treatment had no detectable Cr(VI) in the summit, shoulder, and backslope positions, while the toeslope position had 0.1 mg kg^{-1} of Cr(VI) present.

Multi-energy-μ-XRF maps, Cr μ-XANES spectra, and Cr XANES spectra

The results of multi-energy μ-XRF maps of 400 °C-burned soils from each hillslope position are presented in Figure 3.3. Hexavalent chromium was present in 400 °C-summit soils, which show Cr(VI) halos surrounding Cr-rich particles (chromite) (spectra 4-6 in Figure 3.3A),

which were found to be spatially associated with Fe, Mn and Cr (SI Figure 3.1), as well as other grains in which Cr(VI) is dispersed through the mineral matrix (spectra 1 and 3 in Figure 3.3a). The intensity of Cr(VI) in multi-energy maps decreased with the hillslope position, particularly within the soil mineral matrix. Multi-energy μ-XRF maps of soils from the transition (Figure 3.3b) and toeslope (Figure 3.3c) had few usable spectra for μ-XANES analyses. No Cr(VI) was found in multi-energy maps of soil from the unburned and 800 °C summit treatments (SI Figure 3.2), which is consistent with results from chemical extractions.

Bulk Cr K-edge XANES spectroscopy was used to quantify the increase in Cr(VI) from unburned to burned (400 ºC) soils from each hillslope position (Figure 3.4). Linear combination fitting used unburned soil spectra and a Cr(VI) standard to quantify the increase of Cr(VI) generated in burned soils. The summit position had the greatest increase in Cr(VI) (12.1% of the Cr was fit as Cr(VI)), followed by the shoulder slope (5.5%), toeslope (3%), and backslope position (4.5%). Spectra were also collected on 800 ºC soils, but fits did not identify any Cr(VI).

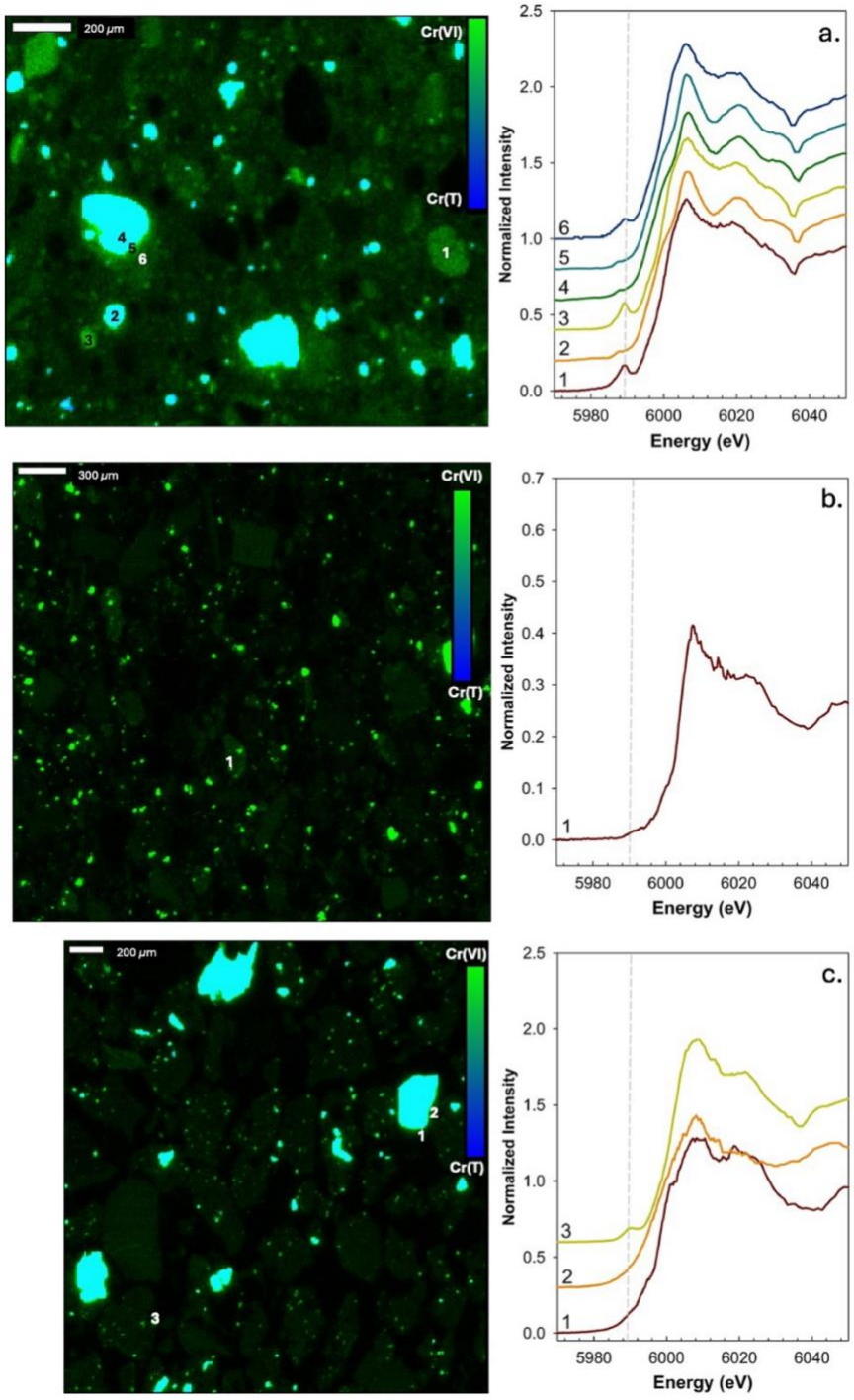

Figure 3.3. (Left) Multi-energy μ-XRF maps of serpentine soils from the (a.) summit, (b.) transition, and (c.) toeslope positions burned at 400 °C. Maps show the relative intensity of Cr(VI) (green) and total Cr (blue). Numbers on the map correlate to the Cr μ-XANES spectra shown on the right. (Right) Cr μ-XANES spectra of points selected for analysis. Vertical lines correspond to the Cr(VI) pre-edge feature at 5989 eV, Cr(III) inflection point at 6003 eV, and total Cr white line at 6010 eV.

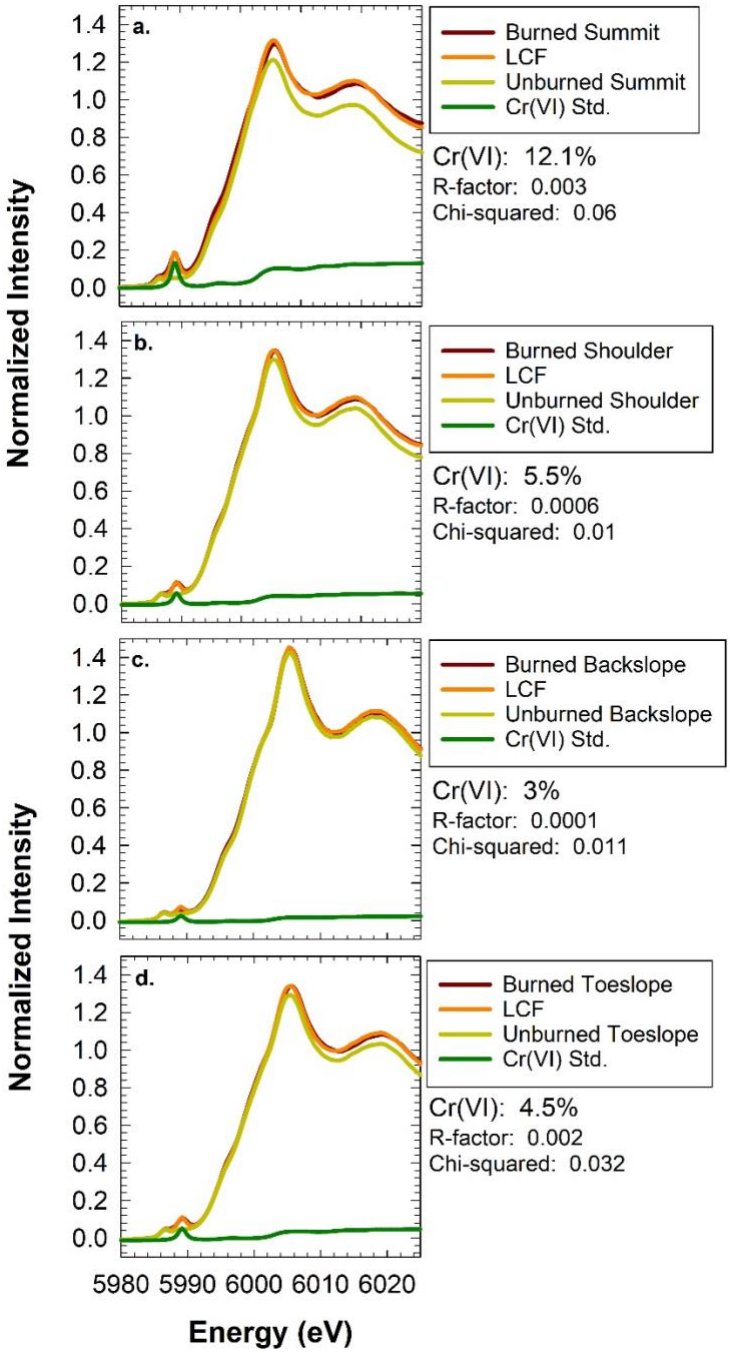

Figure 3.4. Bulk Cr XANES spectra and LCFs of soils burned at 400 °C from the serpentine toposequence in SW Oregon. Soil samples were fit using linear combination fitting (LCF) of unburned soils from the same position and a Cr(VI) mineral standard. (a) summit position, (b) shoulder position, (c) backslope position, and (d) toeslope position. For each plot, the Cr(VI) standard, as a proportion of its fit, is shown in green. Cr XANES spectra of unburned soils were fit to a suite of mineral standards and fits are presented in the supplemental information.

Role of hillslope position and burn intensity on solid-phase associations of Cr and Fe

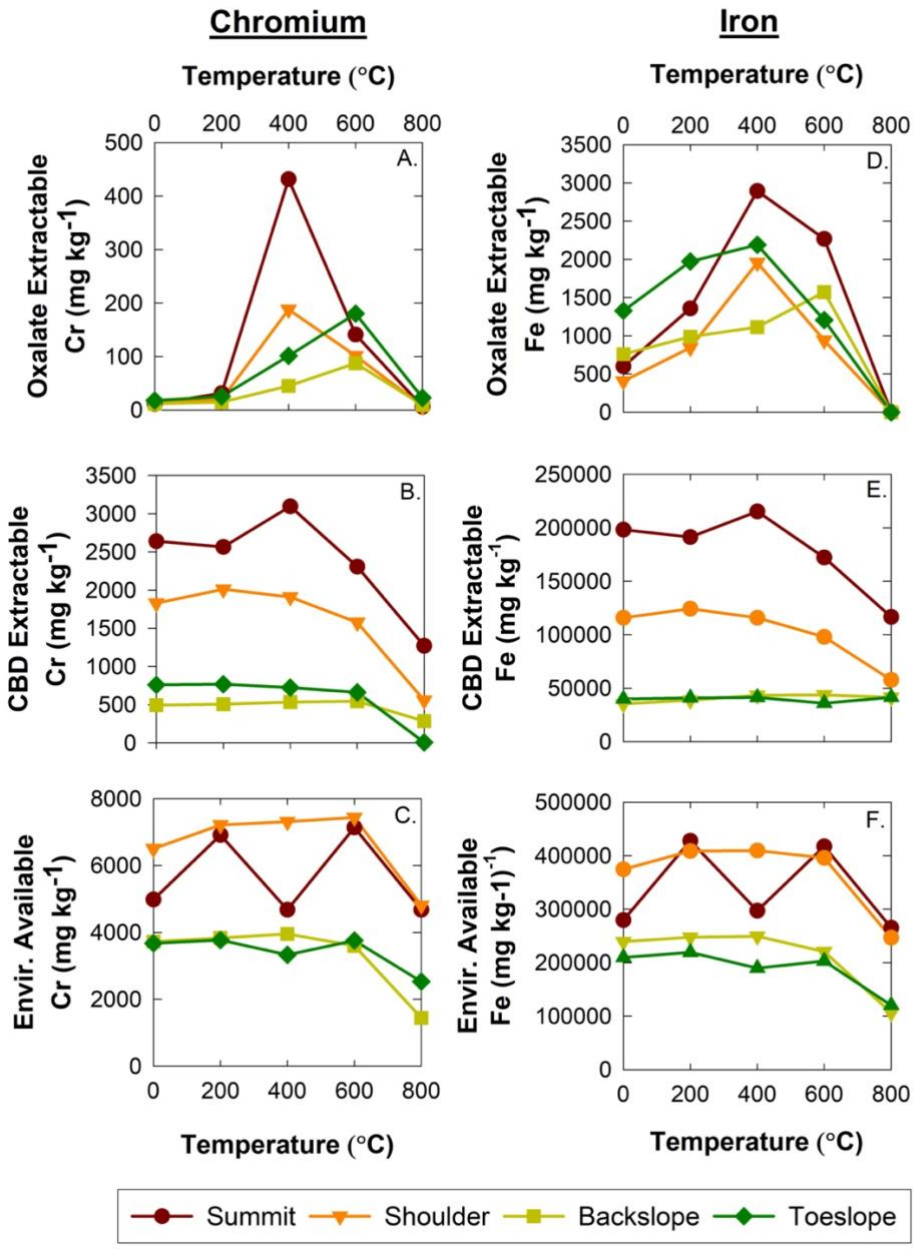

Figure 3.5. Concentrations of chromium (left column) and iron (right column) extracted from serpentine soils from different positions across a toposequence [summit (red circles), shoulder (orange triangles), backslope (yellow squares), and toeslope (green diamonds)] that have been heated up to 800 °C. (top row) Oxalate-extractable Cr and Fe; (middle row) CBD-extractable Cr and Fe; (bottom row) Cr and Fe concentrations after strong-acid digestions. Data points represent averages from experimental triplicate samples. Error bars represent standard error of triplicate measurements; in some cases, error bars are smaller than symbols.

Chromium

Oxalate-extractable Cr as a function of hillslope position and heating treatment is presented in Figure 3.5A. Oxalate-extractable Cr varied with hillslope position and flame induction temperature and was highest in soils from the 400 °C treatment at the summit position (431.6 mg kg^{-1}). Soils from the summit and shoulder slope position (188.0 mg kg^{-1}) had the highest concentrations of oxalate-extractable Cr in the 400 °C treatment, while the backslope and toeslope soils had the highest oxalate-extractable Cr in the 600 °C treatment, with values of 87.7 mg kg^{-1} and 180.2 mg kg^{-1}, respectively. Unburned, 200 ºC, and 800 ºC-treated soils had minimal oxalate-extractable Cr (<30 mg kg^{-1}). Oxalate-extractable Cr was lower in the 800 °C treatment than in the unburned soil, except for at the toeslope.

CBD-extractable Cr from each hillslope position and heating treatment is presented in Figure 3.5B. CBD-extractable Cr was higher in summit soils than in other hillslope positions and was highest in 400 °C soils (3,096 mg kg^{-1}). Summit soils decreased in CBD-extractable Cr in treatments higher than 400 °C. Shoulder slope soils had concentrations of CBD-extractable Cr that slightly increased from the unburned in the 200 °C treatment, thereafter, decreasing in CBD-extractable Cr with increasing temperature treatment. Backslope and toeslope positions had more persistent concentrations of CBD-extractable Cr until the 800 °C treatment, where CBD-extractable Cr decreased.

Strong acid-digested Cr from each hillslope position and heating treatment is presented in Figure 3.5C. Unburned soils had the greatest environmentally available Cr in the shoulder slope position (6,504.56 mg kg^{-1}), followed by the summit position (4,983.5 mg kg^{-1}), thereafter decreasing from the backslope (3,723.23 mg kg^{-1}) to the toeslope (3,612.7 mg kg^{-1}). Burned soils from the 200 °C treatment increased in environmentally available Cr as shoulder slope (7,210.9 mg kg^{-1}) > summit (6,912.7 mg kg^{-1}) > backslope (3,836 mg kg^{-1}) > toeslope (3,770.16 mg kg^{-1}), the same relative relationship observed in the unburned soils. Soils from the 400 °C and 600 °C treatments had similar concentrations of environmentally available Cr in the shoulder slope position. The 400 °C summit soil decreased in environmentally available Cr when compared to the other hillslope positions and the unburned treatment. Soils from the 800 °C treatment substantially decreased in environmentally available Cr, where the summit and shoulder slope positions decreased to similar concentrations. Soils from the 800 °C treatment had less Cr than what was available in the unburned soils.

Iron

Oxalate-extractable Fe as a function of hillslope position and burn intensity are presented in Figure 3.5D. Unburned soils had the greatest concentration of oxalate-extractable Fe in soils from the toeslope position (1,359.2 mg kg^{-1}), followed by the backslope position (760.1 mg kg^{-1}). Soils from the 200 °C treatment had the highest oxalate-extractable Fe in toeslope soils, followed by summit position, which increased from unburned soils. The greatest concentration of oxalate extractable Fe was in summit soils from the 400 °C treatment (2,895 mg kg^{-1}) followed by the summit soils from the 600 °C treatment (2,268.9 mg kg^{-1}). Summit soils from the 600 °C treatment and toeslope soils from the 400 °C treatment was similar (2,268 mg kg^{-1} and 2,190 mg kg^{-1}, respectively). Soils from all hillslope positions except the backslope soils had the highest concentration of oxalate-extractable Fe in the 400 °C treatment, while the backslope position was greatest in the 600 °C treatment. Regardless of the hillslope position, soils from the 800 °C treatment had no detectable oxalate-extractable Fe.

Chemical extractions (citrate-bicarbonate-dithionite), indicative of Fe crystalline oxide phases, are presented in Figure 3.5E. Unburned soils had the greatest CBD-extractable Fe in summit soils from the 400 °C treatment. Regardless of treatment temperature, Summit soils were higher than the other hillslope positions and varied from 11-19% CBD-extractable Fe. Shoulder-slope soils had the second highest CBD-extractable Fe (5-11%), and the backslope and toeslope soils had similar concentrations of CBD-extractable Fe regardless of treatment temperature (3-4%). Regardless of the hillslope position, CBD-extractable Fe varied minimally with burn intensity; however, after 400 degrees, there was a slight decrease until the 800 °C treatment.

Strong acid-digested Fe from each hillslope position and heating treatment are presented in Figure 3.5F. Environmentally available Fe in all soils was above 20% and greater in unburned soils, with the highest concentrations in soils from the shoulder slope position (374,243 mg kg^{-1}). Shoulder slope soils varied minimally with burn intensity until the 800 °C treatment, where Fe decreased by 149,125 mg kg^{-1}. Environmentally available Fe from the summit position had the next highest concentrations of environmentally available Fe in the 200 ºC and 600 ºC treatments, where Fe was 427,635 mg kg^{-1} and 417,298 mg kg^{-1}, respectively. At the 400 ºC treatment, soils from the summit position had decreased to 280,794 mg kg^{-1}, which was similar to unburned and 800 ºC treatments for this position. Backslope soils generally had slightly higher values of environmentally available Fe compared to the toeslope soils with increased burn intensity. Both

the backslope and toeslope positions decreased from the 600 ºC treatment to the 800 ºC treatment.

X-ray diffraction

Table 3.1. Minerals were identified using synchrotron X-ray diffraction of unburned and burned soils from the different temperature treatments. Results of background-corrected and smoothed data were matched to the Match! reference spectra database. Spectra are presented in SI Figure 3.3-3.6.

Hillslope Position	Unburned	200 °C	400 °C	600 °C	800 °C
Summit	Goethite $FeO(OH)$	Hematite Fe_2O_3	Magnetite Fe_3O_4	Hematite	Nichromite $NiCr_2O_4$
Shoulder	Pumpellyite $Ca_2MgAl_2[Si_2O_6OH][SiO_4](OH)_2$	Pumpellyite $Ca_2MgAl_2[Si_2O_6OH][SiO_4](OH)_2$	Maghemite Fe_2O_3	Maghemite Fe_2O_3	
Backslope	Forsterite Mg_2SiO_4	Maghemite Fe_2O_3	Forsterite Mg_2SiO_4	Enstatite $Mg_2Si_2O_6$	
Toeslope	Pumpellyite $Ca_2MgAl_2[Si_2O_6OH][SiO_4](OH)_2$	Lizardite $Mg_3(Si_2O_5)(OH)_4$	Wonesite $Na_{0.4}K_{0.1}Mg_{2.2}Fe^{2+}_{0.4}Al_{1.1}Si_{3.2}O_{10}(OH)_{1.5}F_{0.5}$	Maghemite Fe_2O_3	Clinochlore $Mg_5Al(AlSi_3O_{10})(OH)_8$

As identified by analysis of X-ray diffraction patterns, soil minerals varied with hillslope position and burn intensity (Table 3.1 and SI Figures 3.3-3.6). X-ray diffraction identified that summit soils generally transformed towards more crystalline and less hydrated phases with the incorporation of Cr into minerals at the 800 ºC burn intensity. In summit soils, the dominant minerals identified in order from unburned to 800 ºC were goethite, hematite, magnetite, hematite, and nichromite. Soils from the shoulder slope position were mainly dominated by pumpellyite in the unburned and 200 ºC treatments and maghemite in the 400 ºC and 600 ºC

treatments. The unburned and 200 ºC backslope soils had forsterite, the 200 ºC treatment had maghemite, and the 600 ºC treatment was mainly enstatite. Toeslope soils from unburned to 800 ºC treatment were pumpellyite, lizardite, wonesite, maghemite, and clinochlore.

Chromium transport from unburned and burned soils

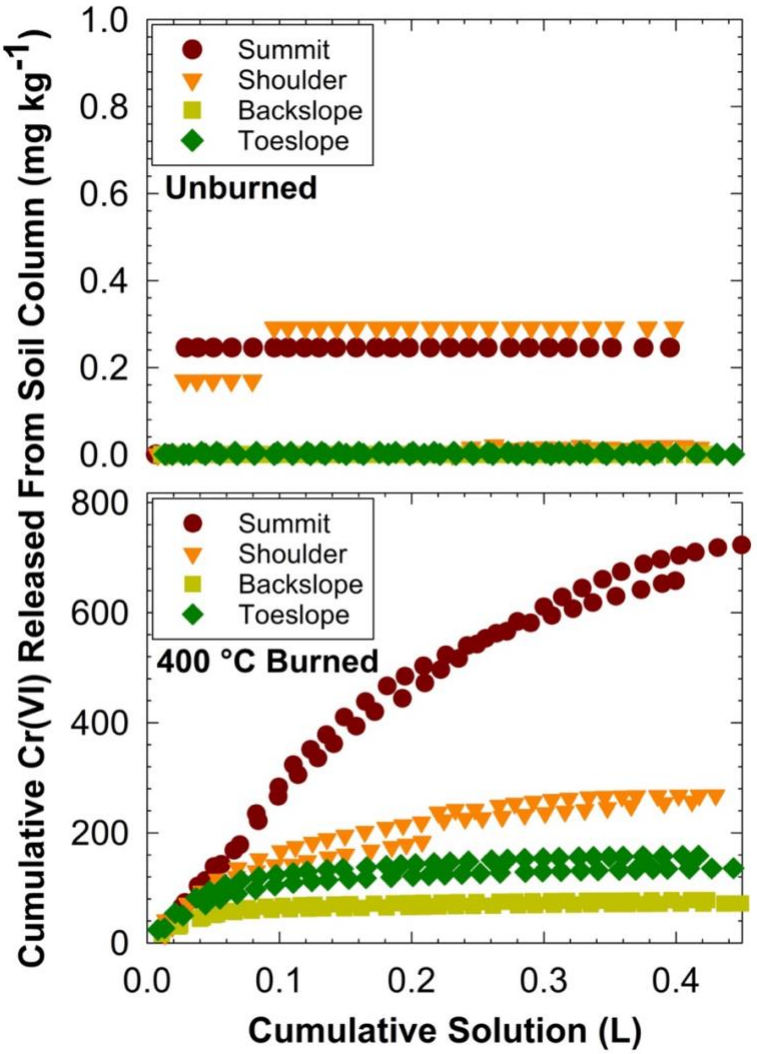

Figure 3.6. Cumulative concentrations of Cr(VI) released from unburned (top) and 400 °C (bottom) serpentine soil columns from different positions across a toposequence. Data from duplicate columns are shown for the summit (red circles), shoulder (orange triangles), backslope (yellow squares), and toeslope (green diamonds) soils. Packed soil columns had a flow rate of 4 mL hr^{-1}, and a total of 0.4 L solution was flushed through each column.

Table 3.2. Average cumulative Cr and Cr(V) released and transported from unburned and burned (400 ºC) soil columns from each hillslope position (summit, shoulder, backslope, and toeslope). Total Cr was analyzed via ICP-OES, and Cr(VI) was analyzed using UV-VIS. Due to the dilutions necessary to run Cr(VI) on the UV-VIS, there is a slight discrepancy between values, but on balance, all of the Cr measured in the solution was present as Cr(VI).

Samples name	Total Cr (mg kg^{-1})	Total Cr(VI) (mg kg^{-1})
Unburned Summit	0.18	0.00
Unburned Shoulder	0.16	0.00
Unburned Backslope	0.06	0.00
Unburned Toeslope	0.05	0.00
400 °C Summit	603.59	694.28
400 °C Shoulder	232.33	262.84
400 °C Backslope	97.77	118.22
400 °C Toeslope	136.06	147.18

Hexavalent Cr transport curves for unburned and burned (400 °C) soil columns as a function of hillslope position are presented in Figure 3.8. Unburned soil columns produced small amounts of Cr(VI) in effluent from two columns (summit and shoulder slope positions), although Cr(VI) was not detected in the effluent of the duplicate columns for these soils (Figure 3.8); the cumulative Cr(VI) concentration transported from unburned soils ranged from 0.05-0.18 mg kg^{-1} column soil. In contrast, burned soils (400 °C) transported greater concentrations of Cr(VI) than the unburned soils, with Cr(VI) efflux ranging from 97.7 – 603.6 mg kg^{-1}. All burned soil columns, regardless of hillslope position, released Cr(VI) at dissolved concentrations that exceeded drinking water standards (0.1 mg L^{-1}) for the entirety of the experiment (Figure 3.8); however, the degree of Cr(VI) released from burned soil columns was dependent on hillslope position. Summit soils had the greatest cumulative concentration of Cr transported from columns (avg. 603.2 mg kg^{-1}), followed by shoulder slope (232.3 mg kg^{-1}), toeslope (136.0 mg kg^{-1}), and then the backslope position (97.7 mg kg^{-1}) (Table 3.2).

The Supplemental Information for Chapter 3 contains additional data obtained from bulk analyses and column experiments. It includes bulk soil pH (SI Figure 3.7) and organic carbon (SI Figure 3.8) for each hillslope position and burn intensity analyzed. Effluent pH (SI Figure 3.9) and Br concentrations (SI Figure 3.10) for the duration of the column experiments. Additionally,

soil organic carbon of unburned and burned soils after column experiments were terminated is presented in SI Figure 3.11.

DISCUSSION

Weathering and mineral variability (Cr and Fe) across the serpentine hillslope

Hillslope position governed the abundance and mineral phase associations of Cr in unburned serpentine soils. Weathering across ultramafic landscapes drives the accumulation and phase of Cr and Fe in soils (Figure 3.5). As in-situ weathering proceeds at the summit and shoulder slope, we observed higher concentrations of environmentally available and free crystalline-associated Cr and Fe than at the backslope and toeslope positions (Figure 3.5). Although unburned soils had greater concentrations of environmentally available Cr and Fe at the shoulder slope position, crystalline-associated Cr and Fe were greatest at the summit position. This may be due to the increased generation of secondary crystalline minerals enriched at the summit position through weathering. High concentrations of Cr at the summit position within the upper 30 cm of soils have been observed in nearby studies that examined Cr variations across a landscape (Alexander et al., 2007). Unburned summit soils were rich in goethite, a weathering product in mature soils, while other soils across the landscape had a mix of primary minerals such as forsterite (Mg-rich olivine) and pumpellyite (silicate-rich) (Table 3.1. and SI Figures 3.3.-3.6.). Landscape position also influences the generation and persistence of amorphous minerals, which, in the soils analyzed, were found in greatest abundance at the toeslope position. Toeslope soils generally have frequent deposition of fresh weatherable minerals from either colluvium or alluvium, increasing the soil's reactive amorphous mineral concentrations (Buol et al., 2011; Obeidy & Polizzotto, 2024). Weathering products (Cr and Fe and their mineral phase association) in soils varied across the hillslope, influencing the generation and availability of flame-induced Cr oxidation.

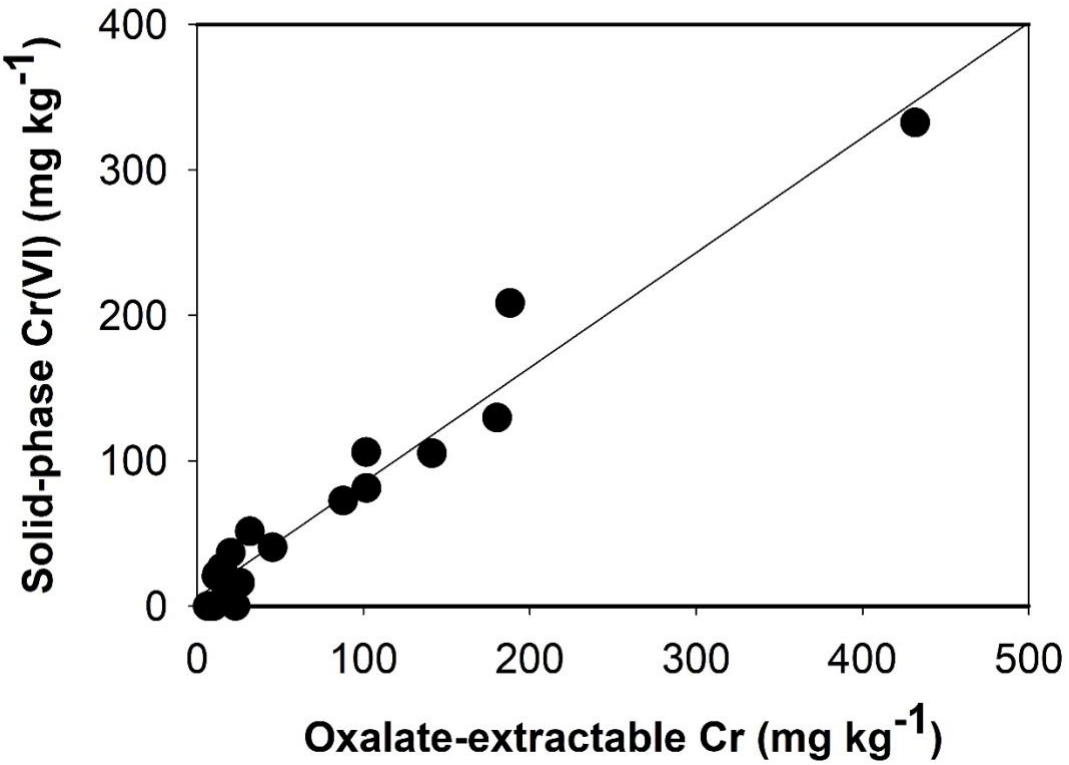

Figure 3.7. Correlation plot of oxalate-extractable Cr and solid-phase Cr(VI) extracted from soils from all the hillslope positions (summit, shoulder, backslope, and toeslope) and burned intensities (unburned, 200 ºC, 400 ºC, 600 ºC, and 800 ºC) analyzed. The near 1:1 relationship and strong correlation suggest that the Cr(VI) generated is likely the same pool of Cr as that extracted by oxalate.

Fate of Cr in burned soils

In burned soils, amorphous mineral transformations are tied to Cr(VI) generation (Figure 3.7). Amorphous phases associated with Cr and Fe increased with burn intensity, specifically at the 200, 400, and 600 ºC temperatures, before dropping to negligible concentrations at 800 ºC. A similar trend with Cr(VI) generation was also observed with burn intensity, and in fact, oxalate-extractable Cr and solid-phase Cr(VI) were correlated (Figure 3.7 and SI Figure 3.12). Oxalate-extractable Cr and solid-phase Cr(VI) generation with burn intensity nearly had a 1:1 relationship, which suggests that the solid-phase Cr(VI) generated with heating is associated with amorphous phases, regardless of hillslope position or burn intensity.

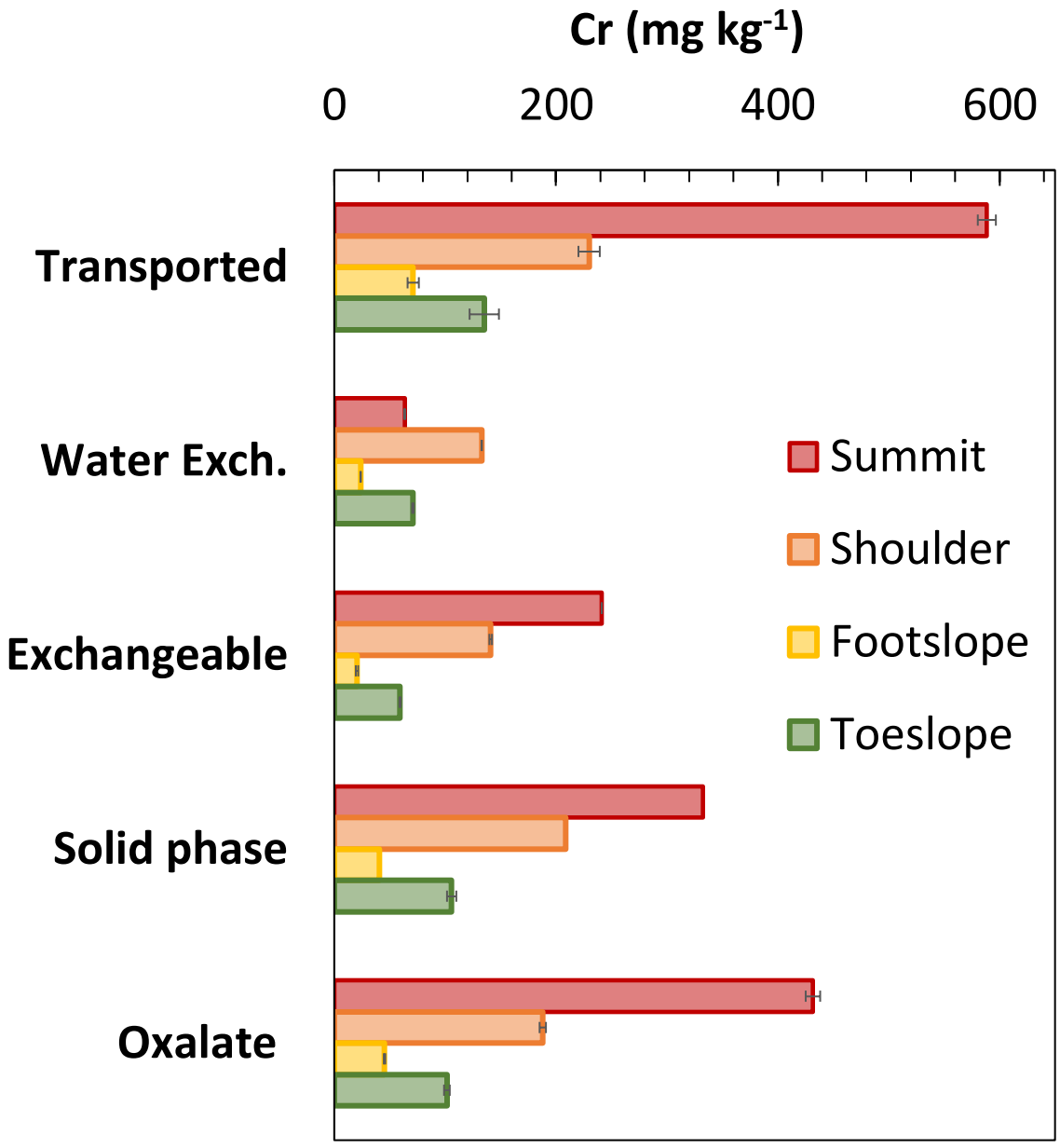

Figure 3.8. Comparison of Cr extractions that targeted labile Cr generated in 400 ºC burned soils from each hillslope position. Red bars indicate the summit position, orange for the shoulder slope, yellow for the backslope, and green for the toeslope. Transported Cr(VI) (column experiments), water exchangeable Cr(VI) (5 mM $MgCl^{2}$), solid-phase Cr(VI) (0.28 M NaCO/0.5 M NaOH), and exchangeable Cr(VI) (10 mM KPO_4^{2-}) were all measured for Cr(VI) via the UV-VIS. Oxalate-extractable Cr was analyzed on the ICP-OES. Error bars represent the standard error of experimental triplicates.

Burn intensity governed the degree of Cr(VI) generated and its availability in soils (Figure 3.2.). Heating at 200 ºC resulted in minimal to no Cr(VI) formation in soils; this may be due to the amorphous mineral transformations not yet occurring by flame-induction or the presence of organic matter in the soil, which can create reducing conditions during low-temperature heating that can prevent Cr(III) oxidation (SI Figure 3.8) (Burton et al., 2019a). Transformation of amorphous Fe minerals towards crystalline phases was observed in soils >400 °C (Figure 3.5), which agrees with prior observations that minerals such as ferrihydrite that transform towards crystalline phases >400 °C in idealized systems (Burton et al., 2019a; Roshan & Biswas, 2023). Between 400 and 600 ºC, Cr(VI) was generated and highly exchangeable (~50% of solid phase Cr(VI) was in an exchangeable form), which is likely due to the degree of oxalate-extractable Cr generated at these temperatures. However, at 800 ºC, amorphous phases and Cr(VI) were low or not detectable either following extractions or through XAS, suggesting that Cr(VI) was reduced or incorporated into new minerals. The observed decrease in amorphous phases and their subsequent transformations with increased burn intensity suggests that these mineral phases have fully transformed towards crystalline phases, converting to minerals such as goethite, hematite, and magnetite, which have been previously observed (Burton et al., 2019a; Johnston et al., 2019; Norouzi & Ramezanpour, 2013; Pereira & Úbeda, 2010; Roshan & Biswas, 2023). Amorphous phases generated through burning have a high surface area and are incredibly reactive; however, as minerals transform towards more crystalline phases, their capacity for sorption decreases, or Cr and Fe are incorporated into new minerals.

Chromium associated with secondary crystalline minerals decreased with increasing burn intensity. High burn intensities (>400 ºC) decreased the concentrations of crystalline-associated Cr and Fe in soils from the summit and shoulder slope positions (Figure 3.5). However, crystalline-associated Cr and Fe in soils from the backslope and toeslope were minimally influenced by burn intensity, except for crystalline-associated Cr in the 800 ºC treatment. Crystalline-associated Cr and Fe in soils from the backslope and toeslope soils varied less than the upper positions investigated with burn intensities, which may be due to the higher proportion of Si/Mg primary minerals to secondary Fe minerals generated through weathering. Results from X-ray diffraction reveal that soils from the summit position transformed from goethite (unburned) to hematite (200 ºC), magnetite (400 ºC), hematite (600 ºC), and lastly, nichromite (800 ºC) (Table 3.1. and SI Figure 3.3.). These results agree with the fact that at 600 °C, spinel-

group minerals form, which would indicate the incorporation of Cr into Cr-spinel minerals (nichromite), which cannot be easily targeted by the CBD and strong-acid extractions we employed (John-Paul Oze, 2003; Roshan & Biswas, 2023). Maghemite, magnetite, and hematite had maximum abundance at 600 and 800 °C, and these minerals were present in some soils across the hillslope we investigated (Ketterings et al., 2000; Roshan & Biswas, 2023). Another indication of mineral transformations in our soils was the increase in soil magnetism with increased burn intensity (SI Figure 3.13.), which aligns with ultra-fine magnetite formation after heat alterations of goethite above 600 °C (Jordanova et al., 2019; Ketterings et al., 2000; Roshan & Biswas, 2023). Overall, soil weathering across the hillslope influenced the proportions of crystalline minerals found in unburned soils and the successive transformations that occurred with burn intensity that influenced Cr(VI) reactivity.

Impact of hillslope position and burn intensity on Cr(VI) reactivity

Hillslope position and burn intensity together governed Cr(VI) generation. The greatest solid-phase and exchangeable Cr(VI) were generated in summit soils from the 400 ºC treatment. In soils from the 600 ºC treatment, solid-phase and exchangeable Cr(VI) were greatest at the toeslope position. Toeslope soils from our study had a similar relationship with burn intensity, and prior studies on burned Ferrosol-type soils have found transformed Cr to be substituted into hematite with increased burn intensity (Burton et al., 2019). Differences in Cr(VI) concentrations between Burton et al., 2019 (non-serpentine soils) and our results can be attributed to the high inherent concentrations of Cr in serpentine-rich soils, usually present as chromite, that are released into soils through weathering. Additionally, in a pure mineral system, Burton et al., 2019 demonstrated that Cr-substituted ferrihydrite had the greatest generation of Cr(VI) at 400 °C, which our data show in soils from the summit and shoulder slope positions. Moreover, we observed a greater degree of exchangeable Cr(VI) (>50%) than the 35% that was observed in Burton et al., 2019.

Recent studies have observed that the generation of Cr(VI) in post-fire ultramafic soils was found at concentrations threatening to human and environmental health (Alexakis, 2020; Lopez et al., 2023). Our experiments generated concentrations of Cr(VI) in soils that were greater than those observed in these field studies, which may be due to differences in initial soil mineralogy, environmental variations from idealized systems, landscape position, the presence or

absence of ash, or the varying temperatures that a landscape experiences during wildfires. Nevertheless, our results are consistent with Lopez et al., 2023, in that Cr(VI) was generated and highly exchangeable in locations that experienced moderate-high severity fires, reflective of mild to high burn intensity temperatures (400 – 600 ºC). Additionally, our μ-XRF multi-energy maps also identified that Cr(VI) was present in the fine mineral matrix of burned soils, similar to findings from Lopez et al., 2023 with ultra-fine soil ash particles. We also identified that Cr(III)-rich particles (chromite) in soils from the 400 ºC burn intensity had Cr(VI) present in halos surrounding these particles. The fine particulates within the mineral matrix that generated Cr(VI) may pose a threat by being airborne during and after a fire. Lopez et al., 2023 demonstrate that the wind-blown fraction (2-µm) across a post-fire landscape also contained Cr(VI), which can create inhalation-based exposure routes to people, particularly first responders.

Transport and persistence of Cr(VI)

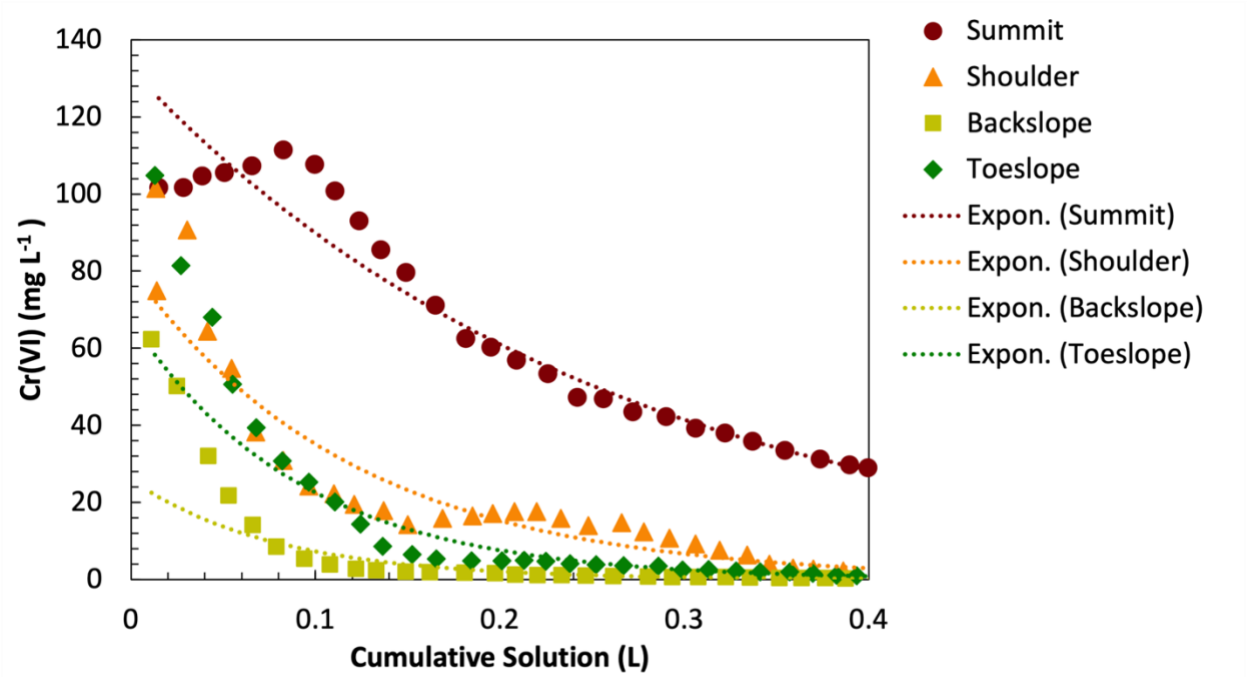

Figure 3.9. Concentrations of Cr(VI) in solution (mg L^{-1}) in column effluent for burned (400 ºC) soils from each hillslope position (summit is presented in red circles, shoulder slope in orange triangles, backslope in blue diamonds, and toeslope in blue squares). Exponential decay equations were used to fit the data and estimate how long effluent Cr(VI) concentrations would persist above the USEPA maximum contaminant level (MCL) for Cr(VI) (0.1 mg L^{-1}). Equations derived from line of best fit are presented in Table 3.3.

Cr(VI) was transported from burned (400 ºC) soil columns at concentrations that exceeded drinking water standards, regardless of hillslope position. The relative trends in variations observed due to the hillslope position agreed with results from solid-phase and exchangeable Cr(VI) measurements (Figure 3.2; Figure 3.9). In summit soils, about 13% of the environmentally available Cr was released as Cr(VI) during transport experiments, highlighting that even a small percentage of flame-induced Cr oxidation could substantially degrade soil and the quality of water draining from fire-impacted serpentine soils. The US EPA's Cr(VI) standard for drinking water is 0.1 mg L^{-1}; no samples collected from transport experiments were below these concentrations.

Table 3.3. Estimated precipitation needed for each hillslope position (summit, shoulder, backslope, and toeslope) to flush Cr(VI) so concentrations drop below the MCL for Cr(VI) (0.1 mg L^{-1}). The estimated time (years) needed to reach MCL levels were calculated using exponential decay best-fit lines of experimental data (Figure 3.9), assuming an average annual rainfall rate 153.94 cm, and normalizing column inflow volumes to the cross-sectional area of 4.90 cm^2.

	Cr(VI)	
Hillslope Position	**Time (yr)**	**Equation used based on the line of best fit**
Summit	2.43	$y = 132.29e^{-3.867x}$
Shoulder	1.05	$y = 80.587e^{-8.309x}$
Backslope	0.57	$y = 25.879e^{-12.67x}$
Toeslope	0.74	$y = 67.23e^{-10.91x}$

Based on experimental results and fitting effluent concentrations with exponential decay curves, we estimate that dangerous Cr(VI) concentrations in soil porewater generated from 10 cm of soil could persist for 0.57 to 2.43 years in post-fire landscapes (Table 3.3; Figure 3.9). The predicted persistence of Cr(VI) in the environment depends on landscape position, with 2.43 years for summit soils, 1.05 years for shoulder slope, 0.57 years for backslope, and 0.74 years for toeslope soils. Although specific times would surely vary in the environment, these results illustrate that the impacts of fires on soil and water quality can be long-lasting. Indeed, field observations of post-fire soils have found that elevated amounts of Cr(VI) in soils persisted at

least a year after a wildfire (Lopez et al., 2023); variations in Cr(VI) concentrations observed by Lopez et al., 2023 may be attributed to the landscape position or specific burn intensity.

Considerations for fire systems

Although our overall findings are experimentally derived, we highlight that the hillslope position governs secondary minerals through weathering, and that in turn influences Cr fate with burn intensity. Hillslope variations play an important role in fire behavior; for example, as fires spread up a hill, fuels can be dehydrated prior to combustion, influencing fire duration and increasing intensity (Pereira & Úbeda, 2010). Our findings that summit soils can generate the greatest hazard for soil and water degradation enhance our understanding of landscape variations on the rapid oxidation of Cr(III) to Cr(VI) by fire, allowing for better predictions across a burned landscape. In a rapidly changing climate where soil and water resources are increasingly important and where wildfire severity, extent, and reoccurrence are increasing, it is essential to understand the landscape controls on soil and water quality landscapes.

CONCLUSION

The rapid oxidation of chromium by fire is a newly understood pathway for soil and water degradation. Weathering across a hillslope drives the distribution and mineral association of Cr in soils and, when burned to different intensities, Cr(VI) is generated and transported. This study investigated the influence of hillslope position and burn intensity on Cr(VI) reactivity and mineral phase associations of Cr and Fe within a serpentine landscape. Chemical and spectral investigations revealed that Cr(VI) generation depends on hillslope position and burn intensity, with the greatest amount of Cr(VI) generated in weathered (summit) soils burned at 400 ºC. Hexavalent Cr generation was tied to amorphous-associated Cr, which is generated with increasing burn intensity (~400 ºC) until Cr is included in newly formed crystalline minerals (800 ºC). Regardless of hillslope position, burned soils can transport Cr(VI) at concentrations that exceed drinking water standards, and Cr(VI) contamination of porewater can persist for 0.5 – 2.4 years following a fire. Our results highlight Cr reactivity throughout a serpentine landscape and the influences of burn intensity on the generation and transport of Cr. Future work could use pyrocosms, prescribed fire, and post-fire monitoring to further evaluate the fate of contaminants

after fire and the mechanisms that influence soil and water quality across a landscape. Furthermore, monitoring of water resources (well water, rivers, and stormwater) draining from fire-impacted landscapes is necessary.

SOURCES OF FINANCIAL SUPPORT

This work was supported by the National Institute of Health through the National Institute of Environmental Health Sciences under Grant No. NIH-5P42ES031007-02 and the University of Oregon. Use of the Stanford Synchrotron Radiation Lightsource, SLAC National Accelerator Laboratory, is supported by the U.S. Department of Energy, Office of Science, Office of Basic Energy Sciences under Contract No. DE-AC02-76SF00515.

ACKNOWLEDGMENTS

We thank Fatai Balogun and Owen Duckworth for supporting the conceptualization of this work; Sam Webb, Nicholas Strange, and Erik Nelson for helping gather data at the Stanford Synchrotron Radiation Lightsource; Lev Zakharov for XRD support; Emily Huckstead for helping gather carbon data: and Chris Russo and Jesse Muratli at Oregon State University for helping gather ICP-OES data.

SUPPLEMENTAL MATERIAL FOR CHAPTER III

Supplemental Tables

SI Table 3.1. Results of Cr(VI) extractions for each hillslope position and burn intensity (0 – 800 ºC) in serpentine soils, including water extractable (5 mM $MgCl^2$), exchangeable (KPO_4^{2-}), and solid-phase methods (strong alkaline digestion).

Water Extraction of Cr(VI) (mg kg^{-1})				
Temperature (°C)	Summit	Shoulder	Backslope	Toeslope
0	0	0	0	0
200	0	0	0	0
400	63.49	132.97	23.78	70.90
600	66.42	64.97	36.65	60.66
800	8.88	4.16	5.33	8.09

KPO_4^{2-} Extraction of Cr(VI) (mg kg^{-1})				
Temperature (°C)	Summit	Shoulder	Backslope	Toeslope
0	2.27	0	0	0
200	43.84	0.59	0.38	0.16
400	241.21	141.03	20.46	59.26
600	46.52	53.77	40.71	76.95
800	2.62	3.43	4.39	5.44

Strong Alkaline Digestion of Cr(VI) (mg kg^{-1})				
Temperature (°C)	Summit	Shoulder	Backslope	Toeslope
0	20.59	20.19	21.79	8.93
200	51.38	36.63	26.47	16.11
400	332.64	208.50	40.43	105.84
600	105.13	81.21	72.53	129.49
800	0	0	0	0.11

Supplemental Figures

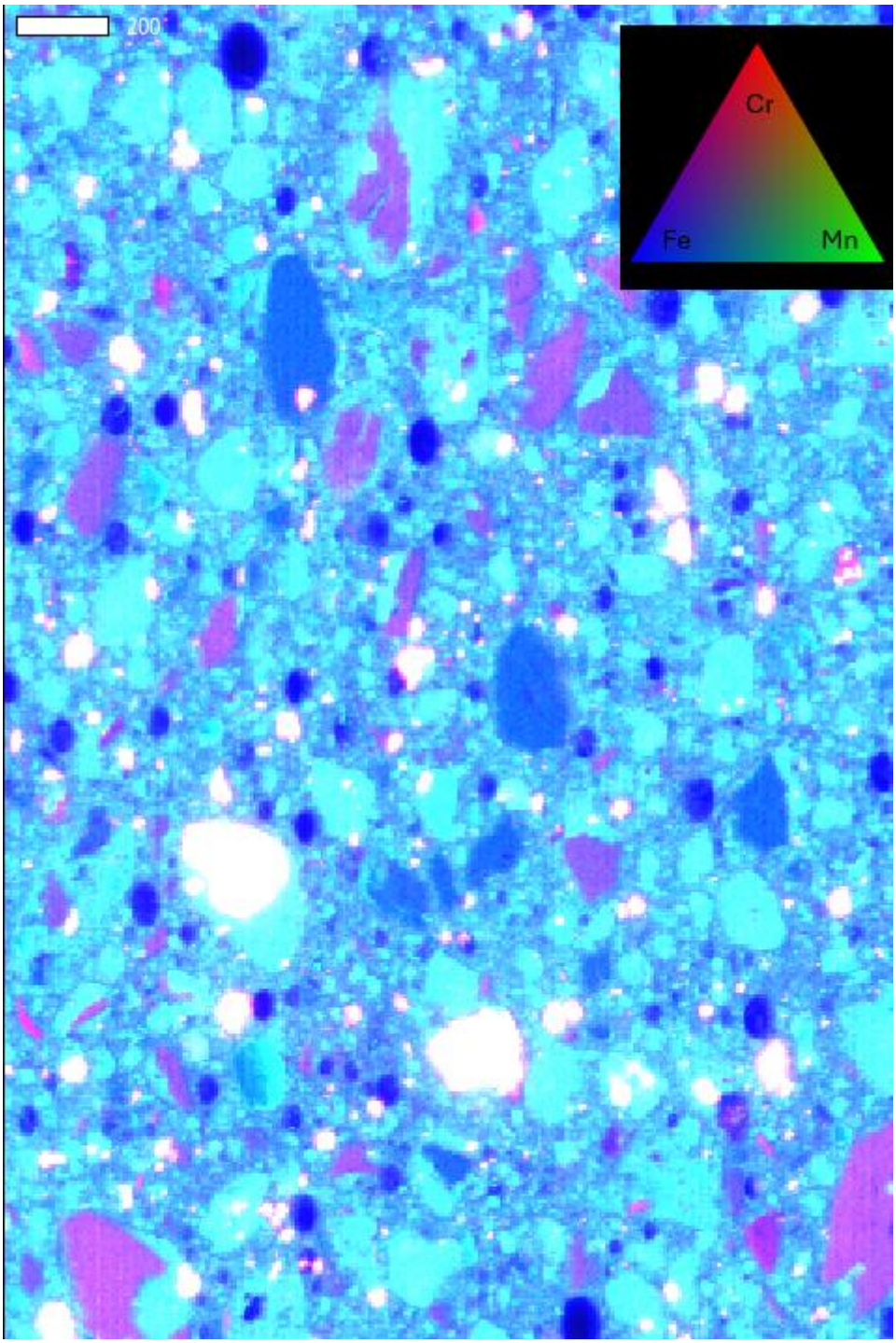

SI Figure 3.1. Spatial associations of Cr (red), Mn (green), and Fe (blue) in 400 ºC summit soils generated using µ-XRF mapping. White zones on the map show where all 3 elements are present. The distinct zones of Cr and Fe are presented in pink, and the light blue color shows where Fe and Mn are present within the mineral matrix. Data was collected at analyzed using Sam Webb's SMAK software. The white scale bar (top left) represents 200 µm.

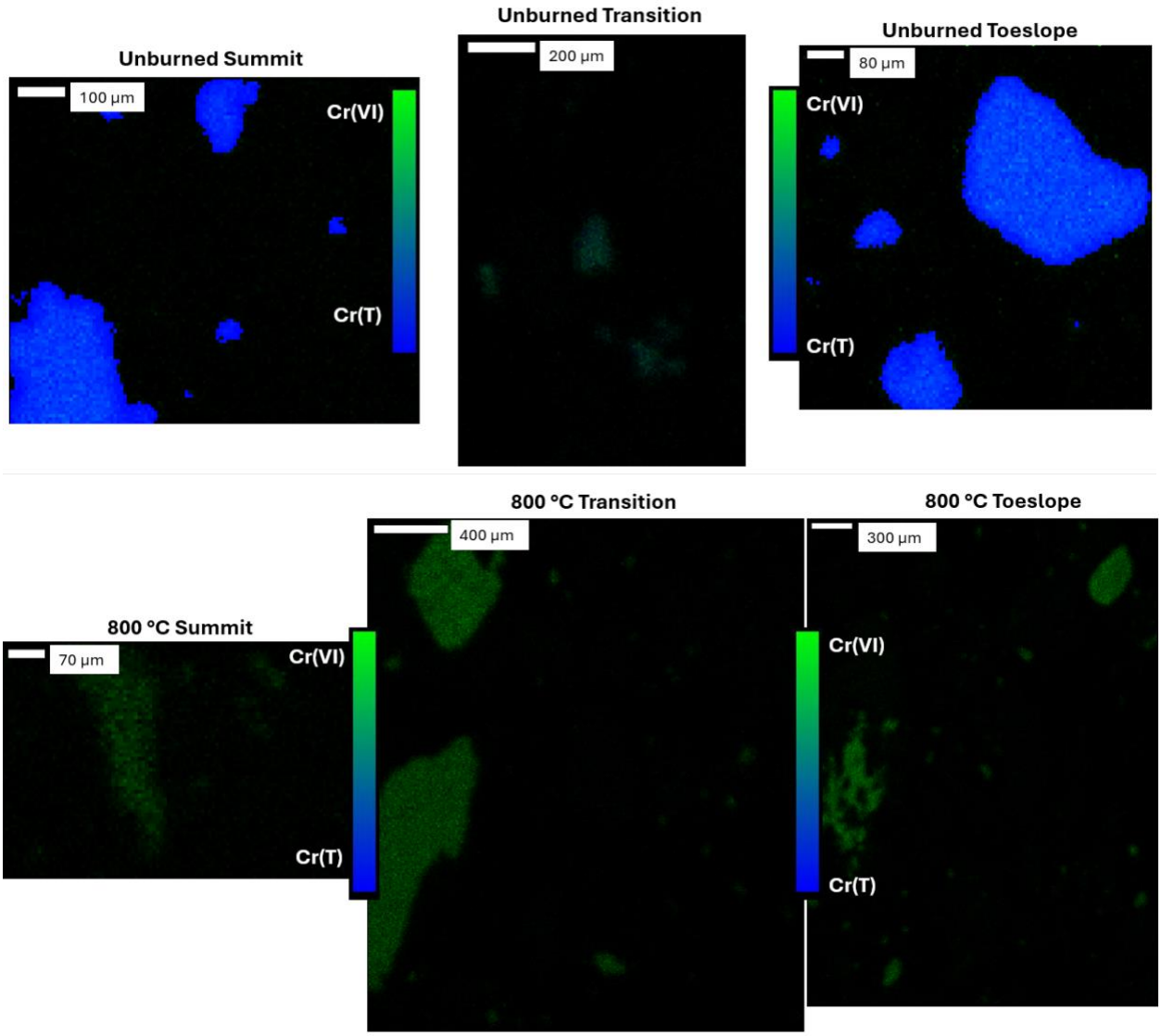

SI Figure 3.2. Multi-energy μ-XRF maps of unburned (top row) and burned (800 °C) serpentine soils from the summit, transition, and toeslope positions (left to right). Maps show the relative intensity of Cr(VI) (green) and total Cr (blue). Multi-energy maps were collected for Cr(VI) at 5989 eV, the Cr(III) inflection point at 6003 eV, and the total Cr white line at 6010 eV.

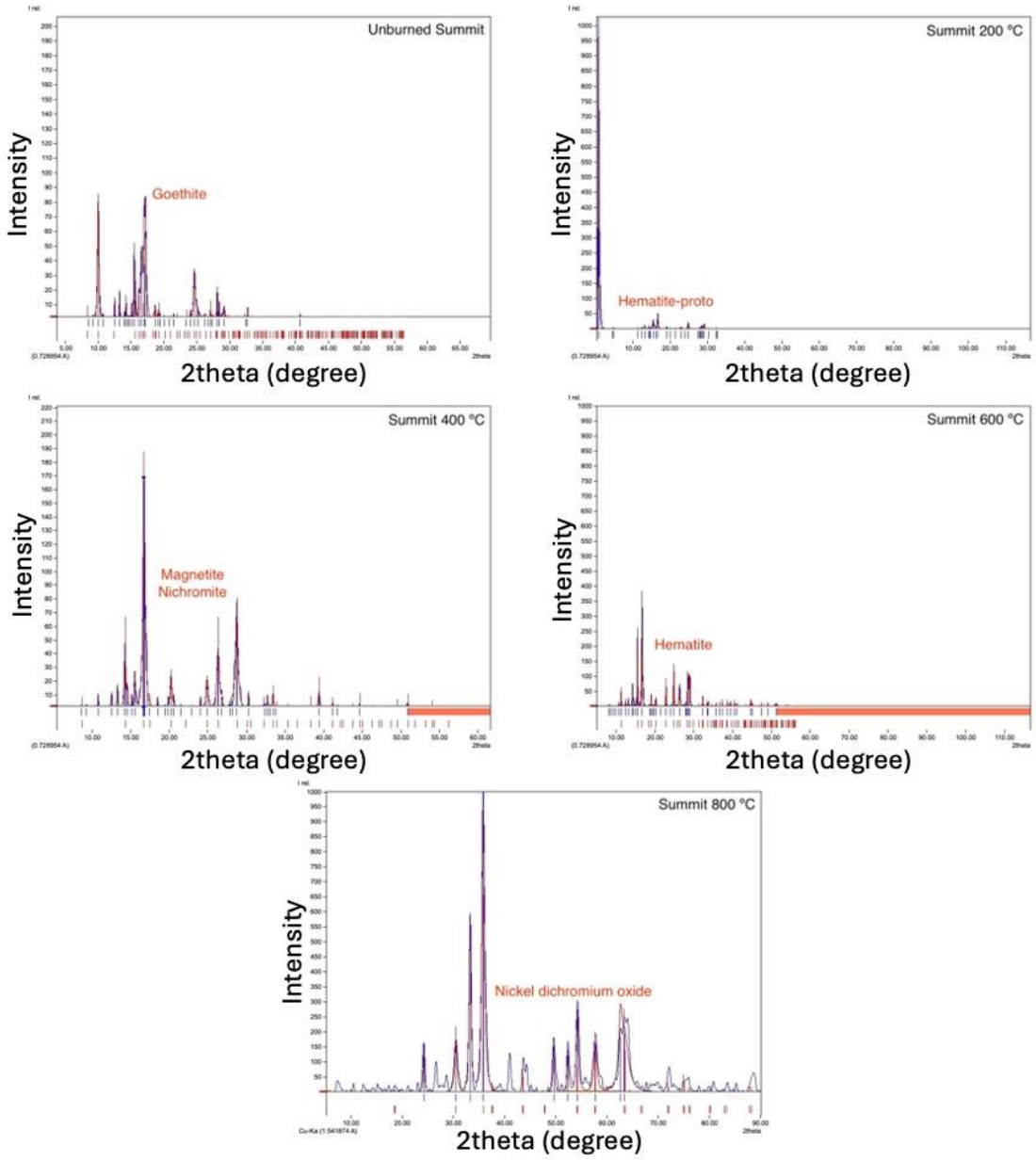

SI Figure 3.3. Powder synchrotron X-ray diffraction was used to examine summit soils from the unburned (top left), 200 ºC (top right), 400 ºC (middle left), 600 ºC (middle right), and 800 ºC (bottom) treatments. The resulting spectra were background-corrected and smoothed, then compared to reference spectra, where the best fits were used. The analysis was carried out on Match!.

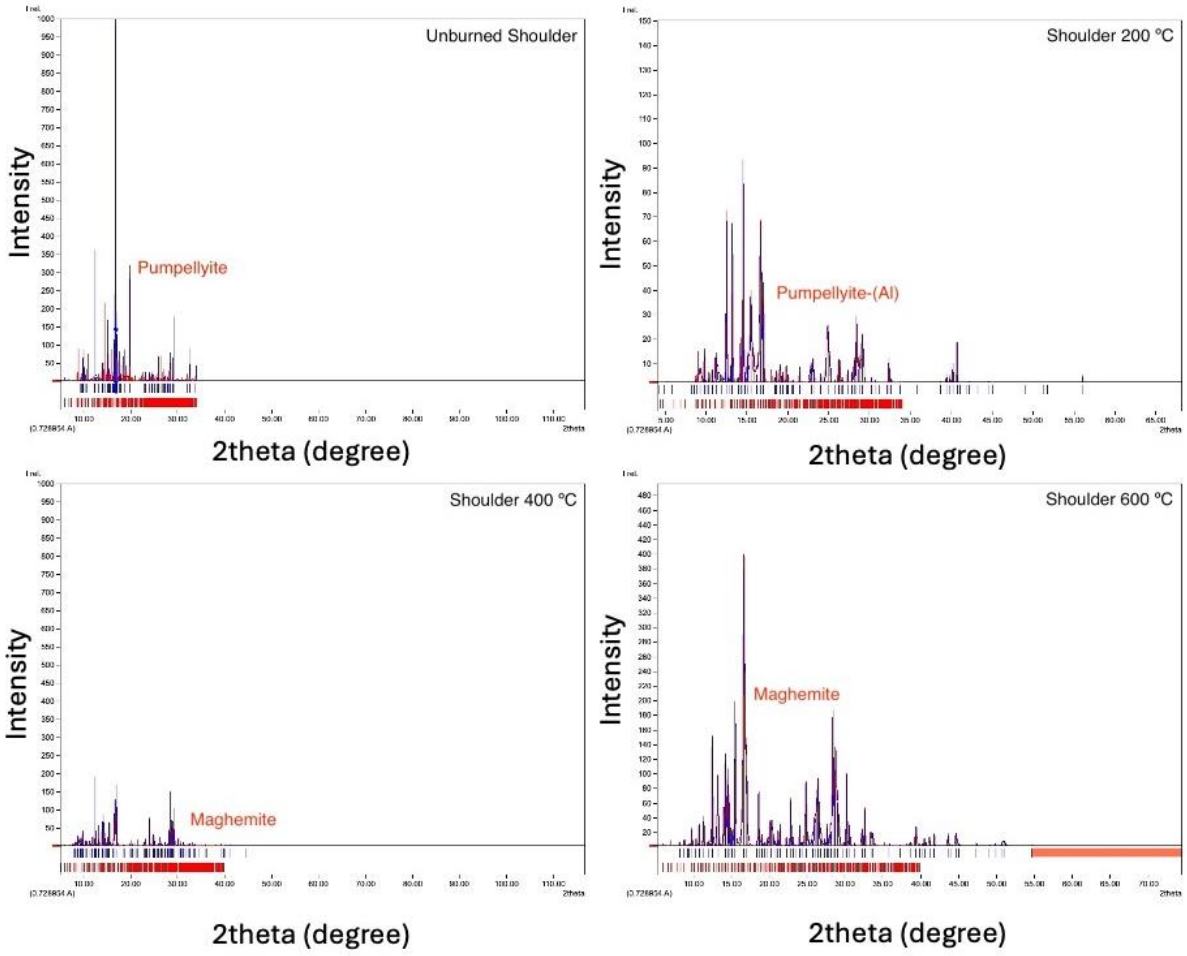

SI Figure 3.4. Powder synchrotron X-ray diffraction was used to examine shoulder slope soils from the unburned (top left), 200 ºC (top right), 400 ºC (bottom left), and 600 ºC (bottom right) treatments. The resulting spectra were background-corrected and smoothed, then compared to reference spectra, where the best fits were used. The analysis was carried out on Match!.

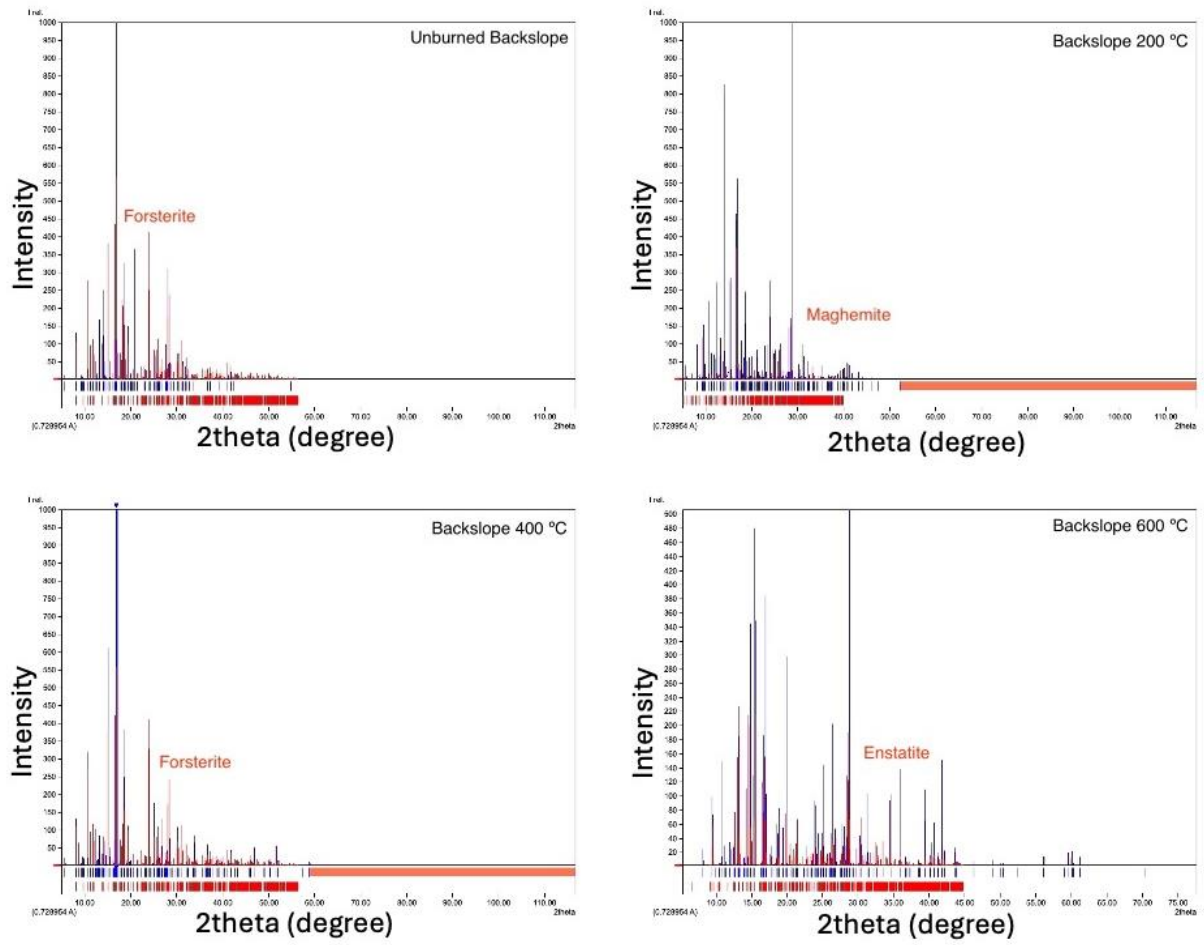

SI Figure 3.5. Powder synchrotron X-ray diffraction was used to examine backslope soils from the unburned (top left), 200 ºC (top right), 400 ºC (bottom left), and 600 ºC (bottom right) treatments. The resulting spectra were background-corrected and smoothed, then compared to reference spectra, where the best fits were used. The analysis was carried out on Match!.

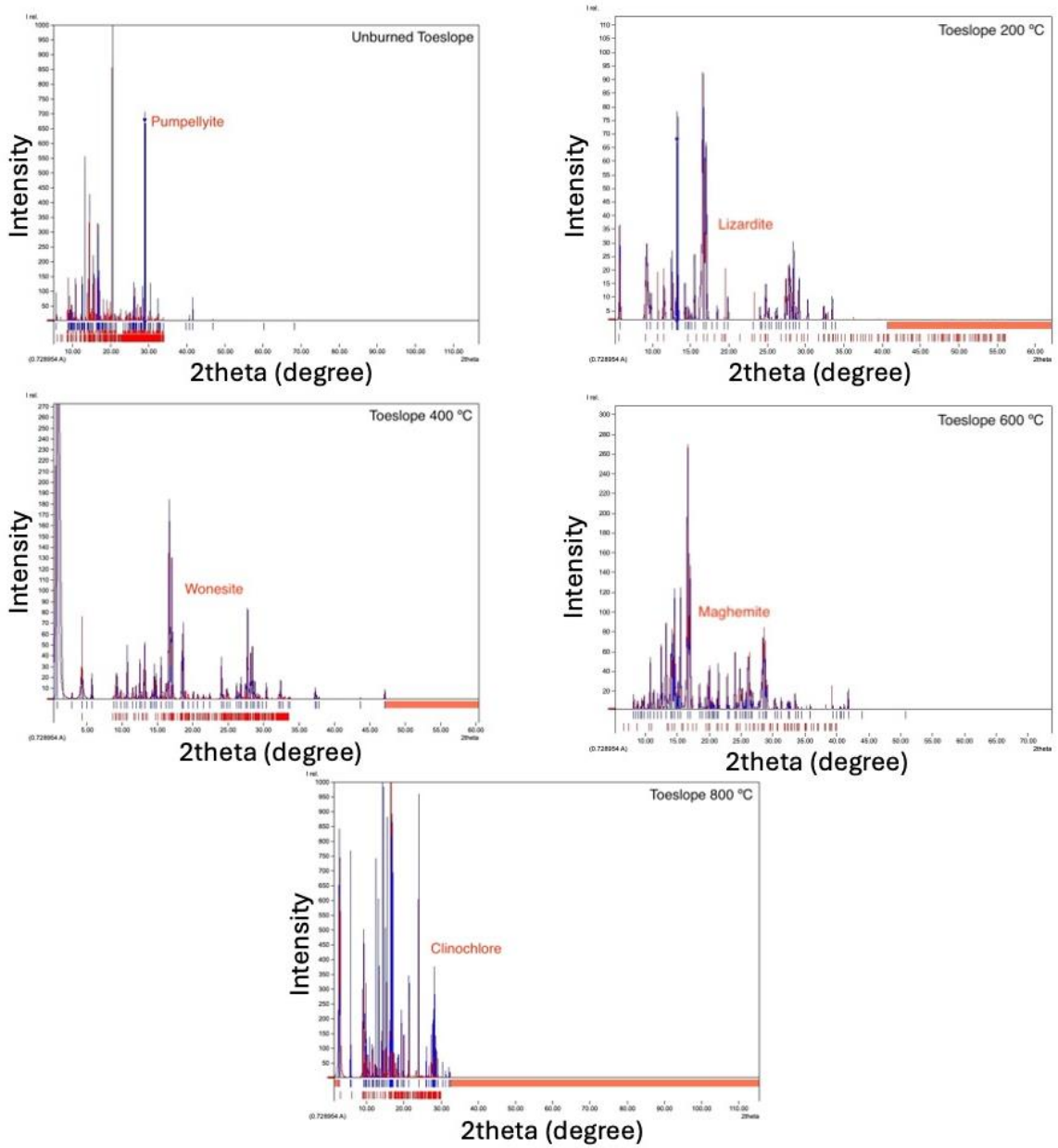

SI Figure 3.6. Powder synchrotron X-ray diffraction was used to examine toeslope soils from the unburned (top left), 200 ºC (top right), 400 ºC (middle left), 600 ºC (middle right), and 800 ºC (bottom) treatments. The resulting spectra were background-corrected and smoothed, then compared to reference spectra, where the best fits were used. The analysis was carried out on Match!

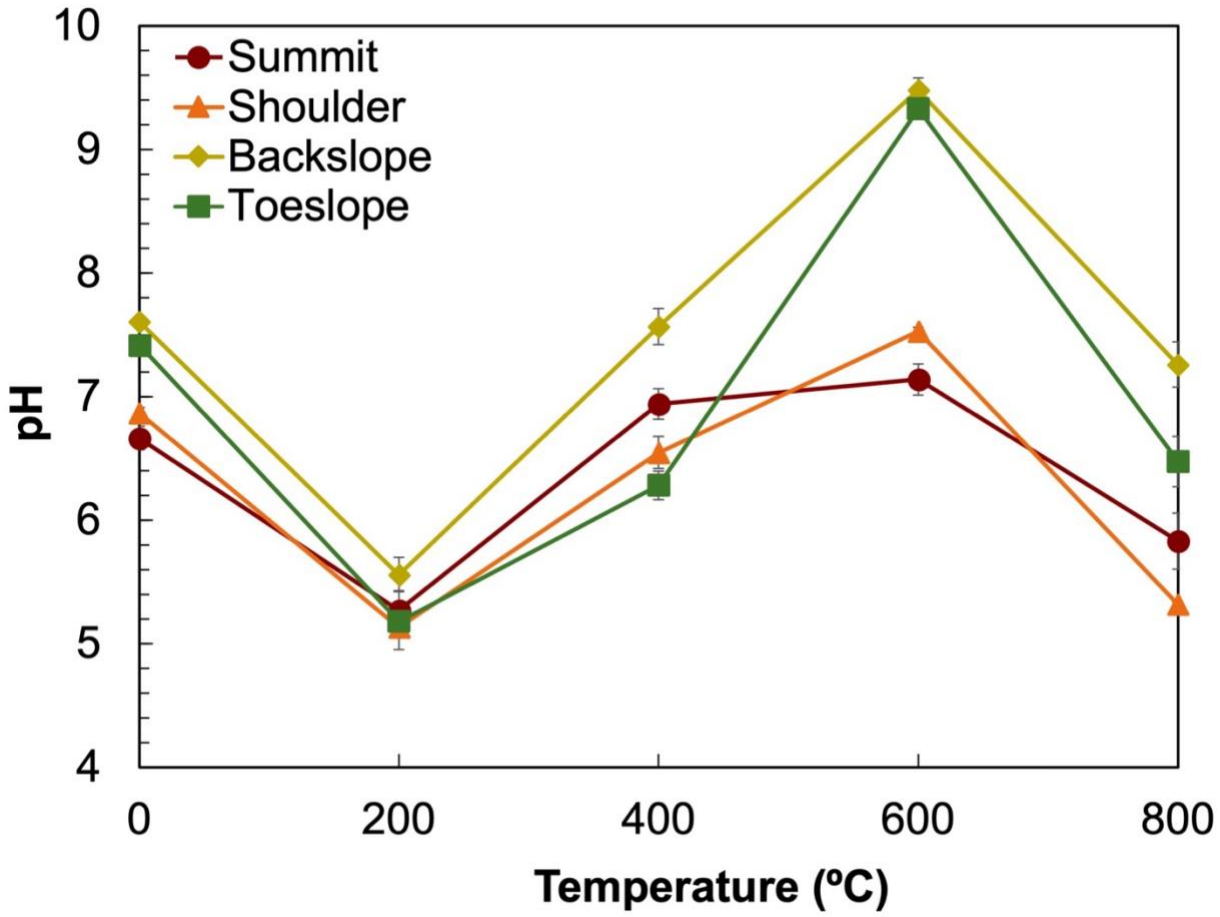

SI Figure 3.7. Soil pH is presented for each hillslope position and burn intensity, that were analyzed from the serpentine toposequence studied. Symbols represent the summit (red circles), shoulder (orange triangles), backslope (yellow squares), and toeslope (green diamonds) soils. Experimental data is averaged from triplicate samples analyzed on the ICP-OES. Error bars represent standard error of triplicate measurements; in some cases, error bars are smaller than symbols.

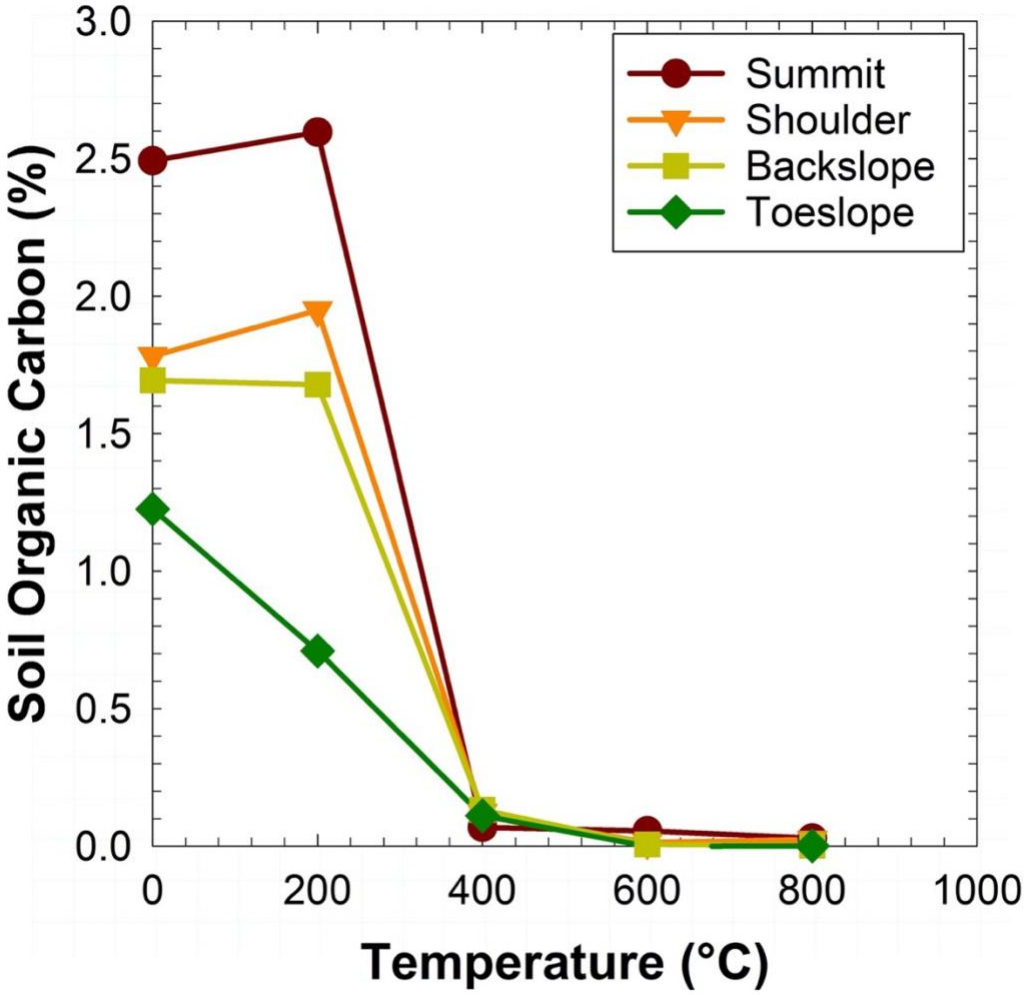

SI Figure 3.8. Soil organic carbon is presented for each hillslope position and burn intensity, which were analyzed from the serpentine toposequence studied. Symbols represent the summit (red circles), shoulder (orange triangles), backslope (yellow squares), and toeslope (green diamonds) soils. Experimental data is averaged from duplicate samples analyzed on the FlashSmart.

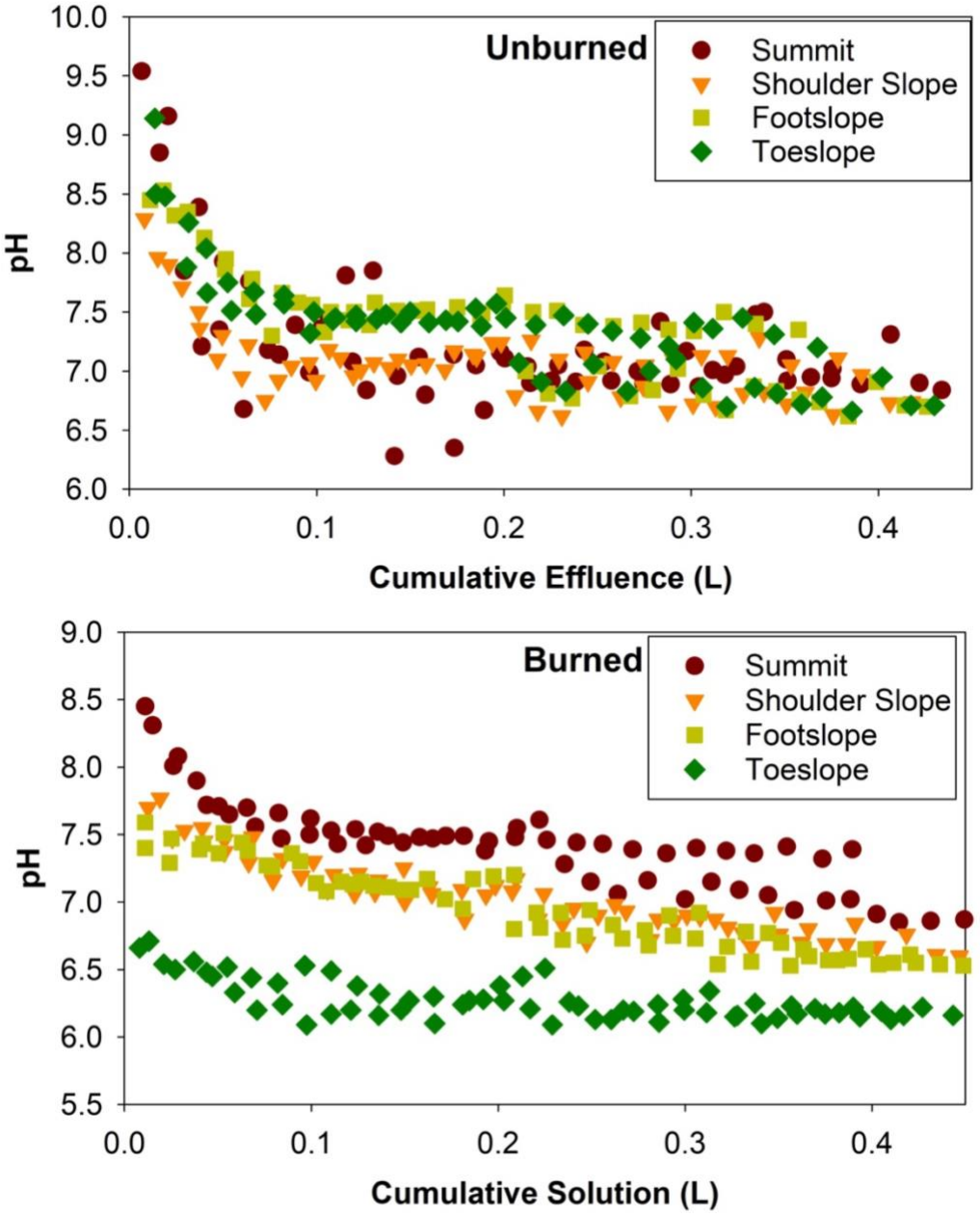

Figure 3.9. The effluence pH from soil column transport experiments is presented. Unburned (top) and burned (bottom) columns were measured in duplicate every 4 hours for the duration of the experiment. Soil columns were from each hillslope position, summit (red circles), shoulder (orange triangles), backslope (yellow squares), and toeslope (green diamonds).

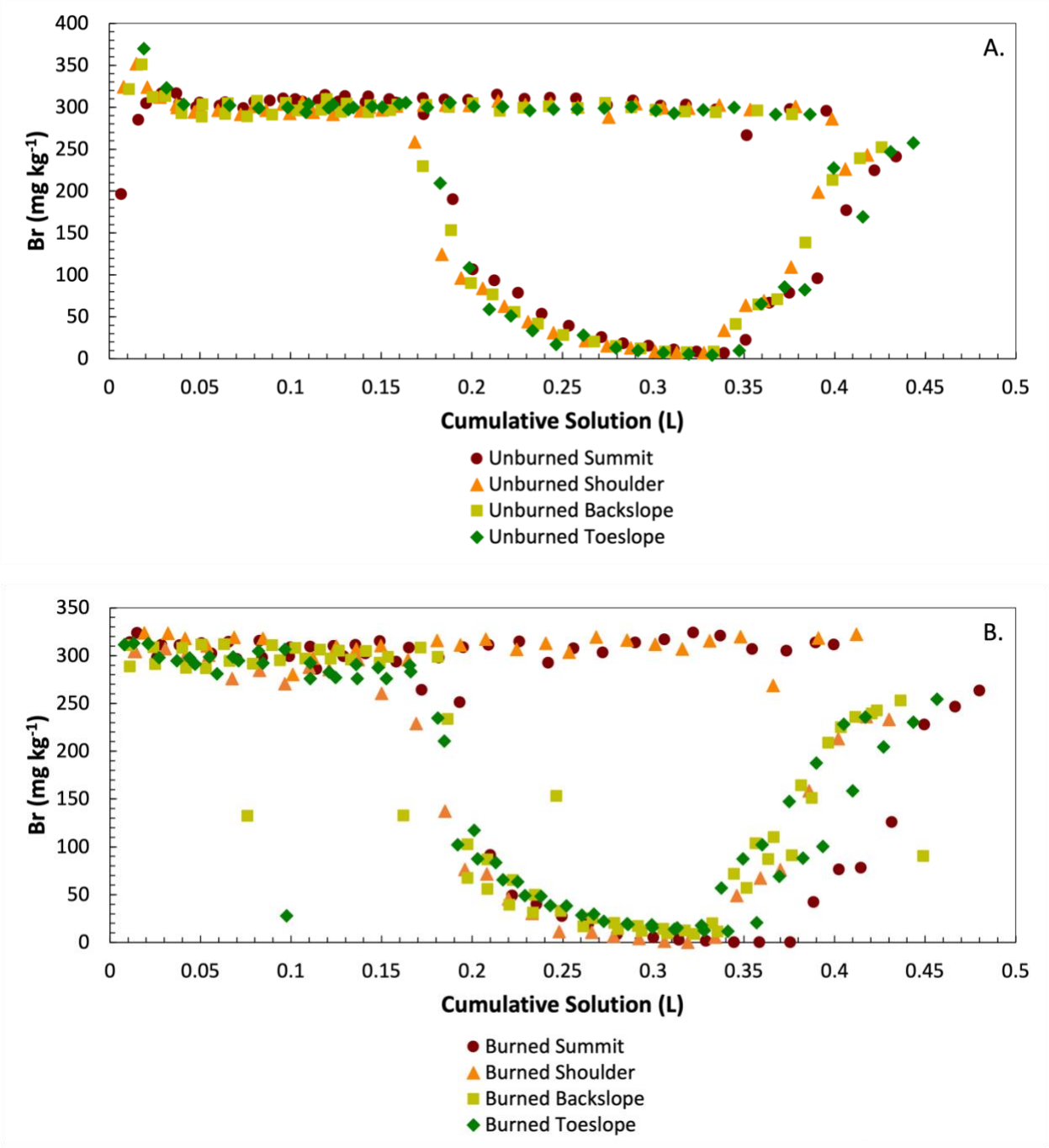

SI Figure 3.10. The concentration of Br was measured in soil effluence from each hillslope position from unburned (A.) and burned (B.) columns. Symbols represent the summit (red circles), shoulder (orange triangles), backslope (green diamonds), and toeslope (blue squares) soils. As a conservative tracer, Br was added to rainwater solutions that were run through soil columns. The input concentrations were the same as effluence solutions. However, Br was not added to one rainwater batch, hence the dip in Br concentrations for unburned and burned soils. Br was analyzed via ICP-OES.

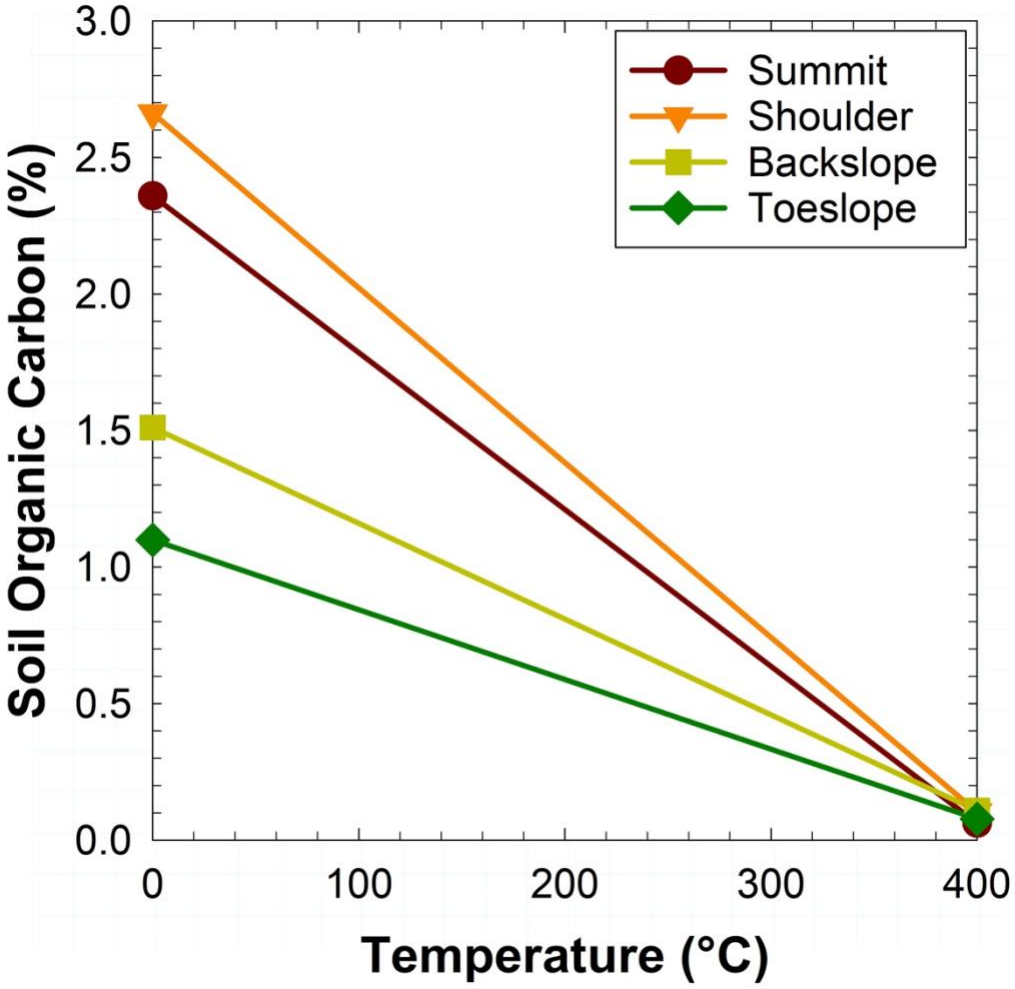

SI Figure 3.11. Soil organic carbon in unburned and burned soils after column flow experimentation. Red circles are from the summit position (red circles), shoulder slope (orange triangles), backslope (yellow squares), and toeslope (green diamonds). Samples were run in duplicate and averaged.

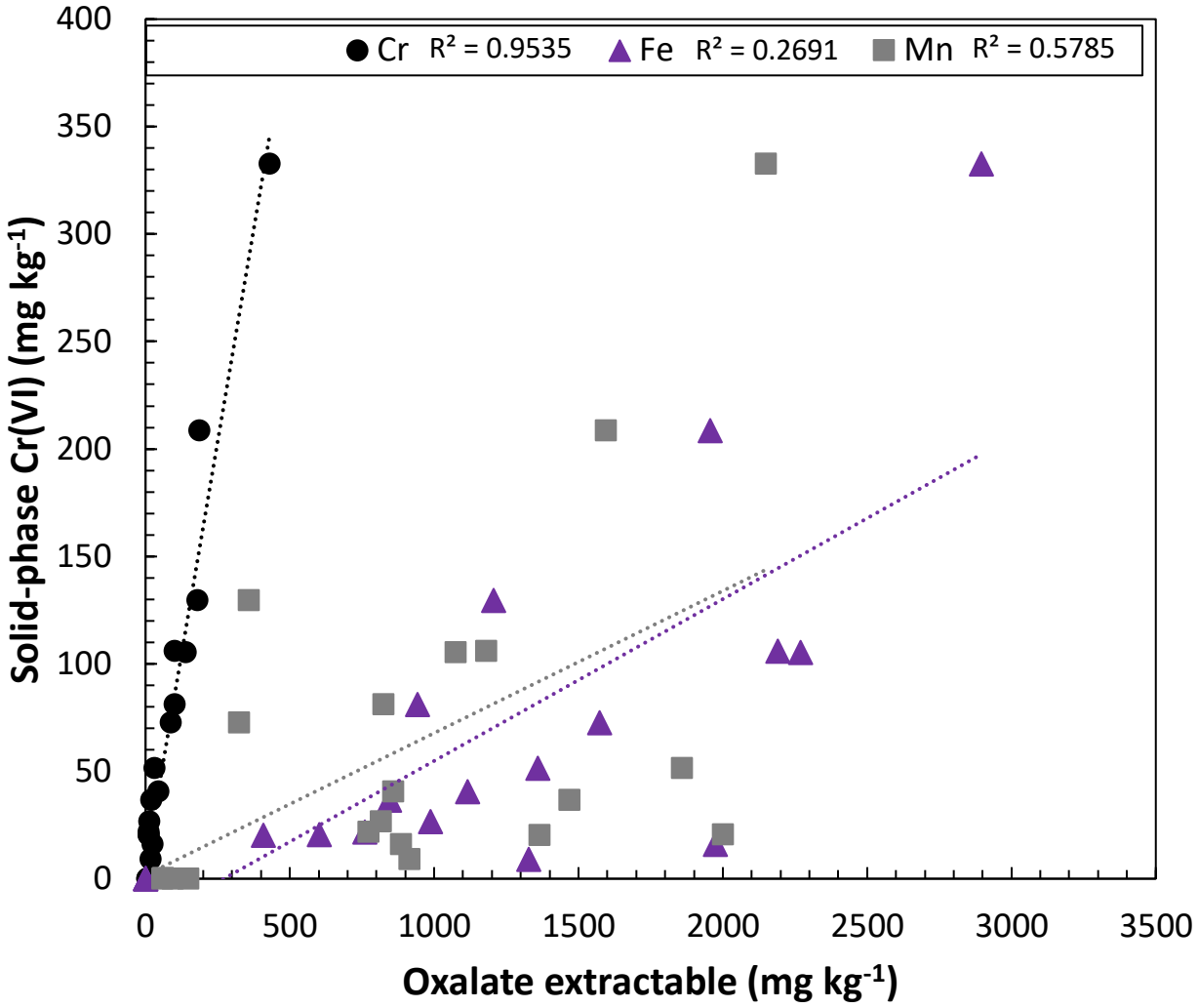

Figure 3.12. Correlation of Solid-phase Cr(VI) and oxalate-extractable Fe (purple triangles), Mn (grey squares), and Cr (black circles) in serpentine soils. All hillslope positions (summit, shoulder, backslope, and toeslope) and burn temperatures are included for each element. Oxalate extractions were analyzed on the ICP-OES and solid-phase Cr(VI) was analyzed on the UV-VIS.

SI Figure 3.13. Burned (800 ºC) soils from the summit position demonstrate enhanced magnetism of soils with increased burn intensity (soil is attached to a stir bar).

REFERENCES

Abraham, J., Dowling, K., & Florentine, S. (2017). Risk of post-fire metal mobilization into surface water resources: A review. In *Science of the Total Environment* (Vols. 599–600, pp. 1740–1755). Elsevier B.V. https://doi.org/10.1016/j.scitotenv.2017.05.096

Alexakis, D. E. (2020). Contaminated land by wildfire effect on ultramafic soil and associated human health and ecological risk. *Land*, *9*(11), 1–16. https://doi.org/10.3390/land9110409

Alexander, E., Ellis, C., & Burke, R. (2007). A chronosequence of soils and vegetation on serpentine terraces in the Klamath Mountains, USA. *Soil Science*, *172*(7).

Allin, D., Stone, M., Silins, U., Emelko, M. B., Collins, A. L., Wolf, B. R. E., Morman, S. a, Plumlee, G. S., Hageman, P. L., Adams, M., Survey, U. S. G., Bladon, K. D., Silins, U., Wagner, M. J., Stone, M., Emelko, M. B., Mendoza, C. A., Devito, K. J., Boon, S., … Walsh, R. P. D. (2008). Release of Hexavalent Chromium by Ash and Soils in Wildfire-Impacted Areas. *Hydrological Processes*, *10*(1), 189–197. http://dx.doi.org/10.1016/j.jhydrol.2013.01.037%0Ahttp://dx.doi.org/10.1016/j.watres.2010.08.051%0A

Bartlett, R. J., & James, B. R. (1996a). *Chapter 25 Chromium*.

Bartlett, R. J., & James, B. R. (1996b). *Methods of Soil Analysis Part 3 Chemical Methods: Vol. Chapter 25*.

Baumeister, J. L., Hausrath, E. M., Olsen, A. A., Tschauner, O., Adcock, C. T., & Metcalf, R. V. (2015). Biogeochemical weathering of serpentinites: An examination of incipient dissolution affecting serpentine soil formation. *Applied Geochemistry*, *54*, 74–84. https://doi.org/10.1016/j.apgeochem.2015.01.002

Bowman, D. M. J. S., Balch, J. K., Artaxo, P., Bond, W. J., Carlson, J. M., Cochrane, M. A., D'Antonio, C. M., DeFries, R. S., Doyle, J. C., Harrison, S. P., Johnston, F. H., Keeley, J. E., Krawchuk, M. A., Kull, C. A., Marston, J. B., Moritz, M. A., Prentice, I. C., Roos, C. I., Scott, A. C., … Pyne, S. J. (2009). Fire in the earth system. *Science*, *324*(5926), 481–484. https://doi.org/10.1126/science.1163886

Bullard, V. (2005). *Weathering of Serpentine Minerals across a Climate Gradient and Toposequence*.

Buol, S. W., Southard, R. J., Graham, R. C., & P.A., M. (2011). *Soil Genesis and Classification* (Sixth). Wiley-Blackwell.

Burton, C. A., Hoefen, T. M., Plumlee, G. S., Baumberger, K. L., Backlin, A. R., Gallegos, E., & Fisher, R. N. (2016). Trace Elements in Stormflow, Ash, and Burned Soil following the 2009 Station Fire in Southern California. *PLOS ONE*, *11*(5), e0153372. https://doi.org/10.1371/journal.pone.0153372

Burton, E. D., Choppala, G., Karimian, N., & Johnston, S. G. (2019a). A new pathway for hexavalent chromium formation in soil: Fire-induced alteration of iron oxides. *Environmental Pollution*, *247*, 618–625. https://doi.org/10.1016/j.envpol.2019.01.094

Burton, E. D., Choppala, G., Karimian, N., & Johnston, S. G. (2019b). A new pathway for hexavalent chromium formation in soil: Fire-induced alteration of iron oxides. *Environmental Pollution*, *247*, 618–625. https://doi.org/10.1016/j.envpol.2019.01.094

Burton, E. D., Choppala, G., Vithana, C. L., Karimian, N., Hockmann, K., & Johnston, S. G. (2019). Chromium(VI) formation via heating of Cr(III)-Fe(III)-(oxy)hydroxides: A pathway for fire-induced soil pollution. *Chemosphere*, *222*, 440–444. https://doi.org/10.1016/j.chemosphere.2019.01.172

Campos, I., Abrantes, N., Keizer, J. J., Vale, C., & Pereira, P. (2016). Major and trace elements in soils and ashes of eucalypt and pine forest plantations in Portugal following a wildfire. *Science of the Total Environment*, *572*, 1363–1376. https://doi.org/10.1016/j.scitotenv.2016.01.190

Cheng, C.-H., Jien, S.-H., Iizuka, Y., Tsai, H., Chang, Y.-H., & Hseu, Z.-Y. (2011). Pedogenic Chromium and Nickel Partitioning in Serpentine Soils along a Toposequence. *Soil Science Society of America Journal*, *75*(2), 659–668. https://doi.org/10.2136/sssaj2010.0007

Chrysochoou, M., Theologou, E., Bompoti, N., Dermatas, D., & Panagiotakis, I. (2016). Occurrence, Origin and Transformation Processes of Geogenic Chromium in Soils and Sediments. In *Current Pollution Reports* (Vol. 2, Issue 4, pp. 224–235). Springer. https://doi.org/10.1007/s40726-016-0044-2

Costa, M. R., Calvão, A. R., & Aranha, J. (2014). Linking wildfire effects on soil and water chemistry of the Marão River watershed, Portugal, and biomass changes detected from Landsat imagery. *Applied Geochemistry*, *44*, 93–102. https://doi.org/10.1016/j.apgeochem.2013.09.009

Crystal Impact. (1997). *Match! Phase Analysis using Powder Diffraction*.

Ellis, A. S., Johnson, T. M., & Bullen, T. D. (2002). Chromium isotopes and the fate of hexavalent chromium in the environment. *Science*, *295*(5562), 2060–2062. https://doi.org/10.1126/science.1068368

Environmental Protection Agency, U. (1992). *Method 7196A*.

Environmental Protection Agency, U. (1996). *METHOD 3050B ACID DIGESTION OF SEDIMENTS, SLUDGES, AND SOILS 1.0 SCOPE AND APPLICATION*.

Halofsky, J. E., Peterson, D. L., & Harvey, B. J. (2020). Changing wildfire, changing forests: the effects of climate change on fire regimes and vegetation in the Pacific Northwest, USA. In *Fire Ecology* (Vol. 16, Issue 1). Springer. https://doi.org/10.1186/s42408-019-0062-8

Harper, G. (1984). The Josephine ophiolite, northwestern California. *Geological Society of America Bulletin*, *95*(9), 1009. https://doi.org/10.1130/0016-7606(1984)95<1009:TJONC>2.0.CO;2

Hotz, P. E. (1964). *NICKELIFEROUS LATERITES IN SOUTHWESTERN OREGON AND NORTHWESTERN CALIFORNIA* •.

Jardine, P. M., Mehlhorn, T. L., Bailey, W. B., Brooks, S. C., Fendorf, S., Gentry, R. W., Phelps, T. J., & Saiers, J. E. (2011). Geochemical Processes Governing the Fate and Transport of Chromium(III) and Chromium(VI) in Soils. *Vadose Zone Journal*, *10*(3), 1058–1070. https://doi.org/10.2136/vzj2010.0102

John-Paul Oze, C. (2003). *CHROMIUM GEOCHEMISTRY OF SERPENTINITES AND SERPENTINE SOILS*.

Johnston, S. G., Karimian, N., & Burton, E. D. (2019). Fire promotes arsenic mobilization and rapid arsenic(III) formation in soil via thermal alteration of arsenic-bearing iron oxides. *Frontiers in Earth Science*, *7*(May), 1–18. https://doi.org/10.3389/feart.2019.00139

Jordanova, N., Jordanova, D., & Barrón, V. (2019). Wildfire severity: Environmental effects revealed by soil magnetic properties. *Land Degradation and Development*, *30*(18), 2226–2242. https://doi.org/10.1002/ldr.3411

Keon, N. E., Swartz, C. H., Brabander, D. J., Harvey, C., & Hemond, H. F. (2001). Validation of an arsenic sequential extraction method for evaluating mobility in sediments. *Environmental Science and Technology*, *35*(13), 2778–2784. https://doi.org/10.1021/es001511o

Ketterings, Q. M., Bigham, J. M., & Laperche, V. (2000). Changes in soil mineralogy and texture caused by slash-and-burn fires in Sumatra, Indonesia. *Soil Science Society of America Journal*, *64*(3), 1108–1117.

Kim, J. G., & Dixon, J. B. (2002). Oxidation and fate of chromium in soils. *Soil Science and Plant Nutrition*, *48*(4), 483–490. https://doi.org/10.1080/00380768.2002.10409230

Kožuh, N., Štupar, J., & Gorenc, B. (2000). Reduction and oxidation processes of chromium in soils. *Environmental Science and Technology*, *34*(1), 112–119. https://doi.org/10.1021/es981162m

Kumamoto, K. M., Warren, J. M., & Hauri, E. H. (2019). Evolution of the Josephine Peridotite Shear Zones: 1. Compositional Variation and Shear Initiation. *Geochemistry, Geophysics, Geosystems*, *20*(12), 5765–5785. https://doi.org/10.1029/2019GC008399

Landrot, G., Ginder-Vogel, M., & Sparks, D. L. (2010). Kinetics of chromium(III) oxidation by manganese(IV) oxides using quick scanning X-ray absorption fine structure spectroscopy (Q-XAFS). *Environmental Science and Technology*, *44*(1), 143–149. https://doi.org/10.1021/es901759w

Landrot, G., Tappero, R., Webb, S. M., & Sparks, D. L. (2012). Arsenic and chromium speciation in an urban contaminated soil. *Chemosphere*, *88*(10), 1196–1201. https://doi.org/10.1016/j.chemosphere.2012.03.069

Liu, P., Ptacek, C. J., Blowes, D. W., Finfrock, Y. Z., Steinepreis, M., & Budimir, F. (2019). A Method for Redox Mapping by Confocal Micro-X-ray Fluorescence Imaging: Using Chromium Species in a Biochar Particle as an Example. *Analytical Chemistry*, *91*(8), 5142–5149. https://doi.org/10.1021/acs.analchem.8b05718

Lopez, A. M., Pacheco, J. L., & Fendorf, S. (2023). Metal toxin threat in wildland fires determined by geology and fire severity. *Nature Communications*, *14*(1). https://doi.org/10.1038/s41467-023-43101-9

Mehra, O. P., & Jackson, M. L. (1958). Iron Oxide Removal from Soils and Clays by a Dithionite-Citrate System Buffered with Sodium Bicarbonate. *Clays and Clay Minerals*, *7*(1), 317–327. https://doi.org/10.1346/ccmn.1958.0070122

Norouzi, M., & Ramezanpour, H. (2013). Effect of Fire on Chemical Forms of Iron and Manganese in Forest Soils of Iran. *Environmental Forensics*, *14*(2), 169–177. https://doi.org/10.1080/15275922.2013.781077

Obeidy, C. S., & Polizzotto, M. L. (2024). Understanding the influence of soil development on contaminant reactivity along a fluvial chronosequence in the Oregon Coast Range. *Geoderma*, *442*. https://doi.org/10.1016/j.geoderma.2024.116784

Oze, C., Fendorf, S., Bird, D. K., & Coleman, R. G. (2004). Chromium geochemistry of serpentine soils. *International Geology Review*, *46*(2), 97–126. https://doi.org/10.2747/0020-6814.46.2.97

Panichev, N., Mabasa, W., Ngobeni, P., Mandiwana, K., & Panicheva, S. (2008). The oxidation of Cr(III) to Cr(VI) in the environment by atmospheric oxygen during the bush fires. *Journal of Hazardous Materials*, *153*(3), 937–941. https://doi.org/10.1016/j.jhazmat.2007.09.044

Peel, H. R., Balogun, F. O., Bowers, C. A., Miller, C. T., Obeidy, C. S., Polizzotto, M. L., Tashnia, S. U., Vinson, D. S., & Duckworth, O. W. (2022). Towards Understanding Factors Affecting Arsenic, Chromium, and Vanadium Mobility in the Subsurface. *Water (Switzerland)*, *14*(22), 1–36. https://doi.org/10.3390/w14223687

Pereira, P., & Úbeda, X. (2010). Spatial distribution of heavy metals released from ashes after a wildfire. *Journal of Environmental Engineering and Landscape Management*, *18*(1), 13–22. https://doi.org/10.3846/jeelm.2010.02

Plumlee, G. S., Martin, D. A., Hoefen, T., Kokaly, R., Hageman, P., Eckberg, A., Meeker, G. P., Adams, M., Anthony, M., & Lamothe, P. J. (2007). *Preliminary Analytical Results for Ash and Burned Soils from the October 2007 Southern California Wildfires*. http://www.usgs.gov/pubprod

Ravel, B., & Newville, M. (2005). *ATHENA, ARTEMIS, HEPHAESTUS: data analysis for X-ray absorption spectroscopy using IFEFFIT* (pp. 537–541). Journal of Synchrotron Radiation.

Roshan, A., & Biswas, A. (2023). Fire-induced geochemical changes in soil: Implication for the element cycling. In *Science of the Total Environment* (Vol. 868). Elsevier B.V. https://doi.org/10.1016/j.scitotenv.2023.161714

Stankov Jovanovic, V. P., Ilic, M. D., Markovic, M. S., Mitic, V. D., Nikolic Mandic, S. D., & Stojanovic, G. S. (2011). Wild fire impact on copper, zinc, lead and cadmium distribution in soil and relation with abundance in selected plants of Lamiaceae family from Vidlic Mountain (Serbia). *Chemosphere*, *84*(11), 1584–1591. https://doi.org/10.1016/j.chemosphere.2011.05.048

United States Environmental Protection Agency. (1996). *Method 3060A.*

Webb, S. (2011). *The MicroAnalysis Toolkit: X-ray Fluorescence Image Processing Software*. Amer. Inst. Phys. Conf. Proc. 1365196-199.

CHAPTER IV: HEAT-INDUCED METAL REACTIVITY ALONG A SERPENTINE SOIL TOPOSEQUENCE IN SOUTHWESTERN OREGON

Chelsea S. Obeidy, Markus W. Koeneke, and Matthew L. Polizzotto

Reproduced with permission from Obeidy, C.S., Koeneke, M.W., Polizzotto, M. L.

INTRODUCTION

Wildfires are the most widespread ecosystem disturbance and pose a worldwide threat to human and environmental health (Abatzoglou & Williams, 2016; Williams et al., 2019). In California and Southern Oregon, climate change is expected to increase wildfire frequency and extent and decrease precipitation and snowpack (Dube, 2009). Such environmental changes threaten the security and quality of drinking water and soil resources for millions of people.

Serpentine landscapes that occur throughout California and Southern Oregon have naturally high concentrations of Cr, V, Ni, Co, and Mn in soils (Baumeister et al., 2015; Oze, 2003; Oze et al., 2004). Serpentine soils are derived from the weathering of ultramafic and serpentine bedrocks (Baumeister et al., 2015), and since weathering products vary across a landscape, serpentine toposequences have been utilized to capture differences in pedogenic variations (Bani et al., 2014; Bullard, 2005; Cheng et al., 2011). In California, along a serpentine toposequence, weathering and primary mineral alteration were greatest at the summit position and decreased with the hillslope position (Bullard, 2005). Furthermore, Ni availability was greater in upslope soils enriched in iron oxides compared to soils found down-slope, where secondary smectites increased (Bani et al., 2014). In a Taiwanese serpentine toposequence, landscape position was the most important factor in controlling the abundance of Cr and Ni, which accumulated at the footslope position and, to a lesser degree, at the shoulder and backslope position (Cheng et al., 2011). Differences in weathering across serpentine landscapes govern the distributions, phases, and availability of Cr, V, Ni, Co, and Mn, which wildfire can further transform (Caillaud et al., 2009; Kumar & Maiti, 2013).

Contaminants (Co, Mn, Ni, and V) that are naturally enriched in serpentine soils pose a risk to human and environmental health, and the availability of several of these contaminants is increased by wildfires and wildfire ash (Abraham et al., 2017; Lopez et al., 2023; Roshan & Biswas, 2023). For example, Mn concentrations in soil water are generally increased in post-fire

landscapes by the addition of ash, and it is present in a more mobile and easily reducible form than prior to the fire (Alexakis, 2020; Campos et al., 2016). Nickel has also been detected in post-fire soils and ash (Alexakis, 2020; Campos et al., 2016). Recently, post-fire transformations of Cr, Mn, and Ni towards more mobile and toxic forms in serpentine soils have been observed, with concentrations that exceeded health standards (Alexakis, 2020). However, despite these observations, it remains unclear how fire-induced changes to contaminants may vary within and across landscapes, limiting the ability to make predictions about long-term threats to environmental quality and assess post-fire remediation needs.

This research seeks to expand our understanding of heat-induced contaminant transformations and transport from serpentine soils as a function of hillslope position. We specifically hypothesized that soil Co, Mn, Ni, and V would be transformed into more mobile forms with increased burn intensity. Due to the in-situ weathering of contaminant-rich parent materials, we expected summit soils to have the most available metals. To test these hypotheses, we utilized a serpentine soil toposequence in the Josephine ophiolite in southwestern Oregon with naturally high concentrations of Co, Mn, Ni, and V to constrain the influence of hillslope position on soil contaminant reactivity after flame-induction. We sought to (1) quantify the effect of hillslope position on Co, Mn, Ni, and V mineral phase associations with variable burn intensities and (2) evaluate the transport of Co, Mn, Ni, and V from burned (400 ºC) serpentine soils. Our results reveal that weathering across a hillslope influenced the initial concentrations of contaminants and the impacts of burn intensity on contaminant availability and mineral phase associations. Available contaminants were greatest in summit soils and were associated with amorphous and crystalline minerals, which generally decreased with increased burn intensity. Our results also reveal that Ni and Mn may be transported from burned soils at dissolved concentrations that exceed drinking water standards, regardless of hillslope position. This work expands our understanding of heat-induced contaminant transport and quantifies the potential risks that burned soils can pose to a serpentine landscape that regularly experiences fire.

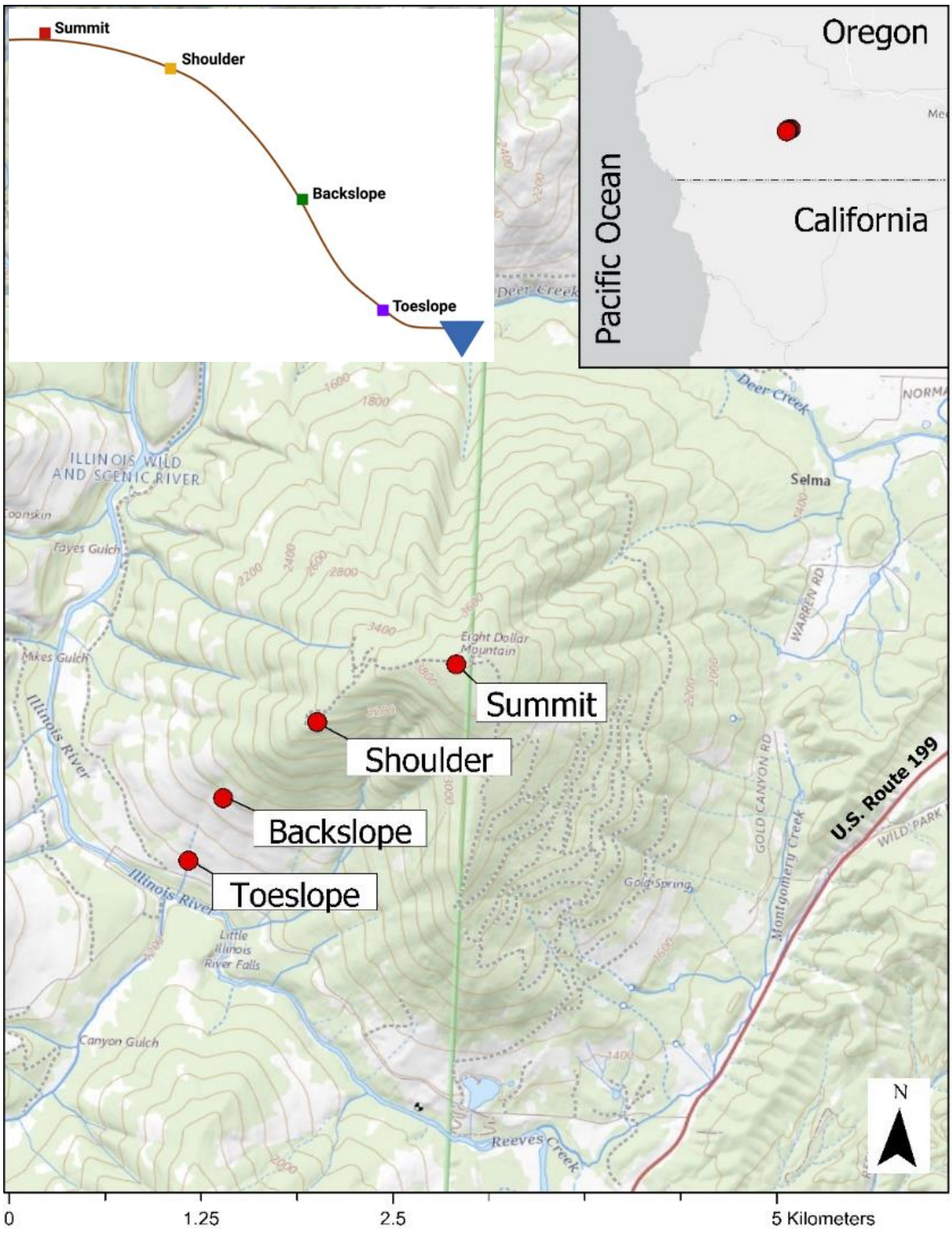

Figure 4.1. The location of the serpentine toposequence analyzed along the Illinois River in the Rogue River Siskiyou National Forest in southwestern Oregon, USA. Triplicate soil samples were collected from each hillslope position: summit, shoulder, backslope, and toeslope.

MATERIALS AND METHODS

Study Site and Soil Samples

Soils from a toposequence in the Josephine ophiolite deposit were used to elucidate the influence of flame-induced Cr transformations as a function of temperature and hillslope position (Figure 4.1). A detailed description of the study site and sampling regime is provided in Chapter 3.

Heating experiment

Soils from different hillslope positions were heated in a muffle furnace to simulate fire-induced thermal alteration. Soils were sieved using a brass 2-mm sieve and 10 g was then placed in 10-mL ceramic crucibles for incineration. Soils were heated in a Thermoscientific Thermolyne muffle furnace for 2 h at 200, 400, 600, and 800 ºC, simulating fires of different burn intensities and a time that can be experienced in burning landscapes (Burton et al., 2019a; Burton et al., 2019). Soils were cooled at room temperature before being subjected to chemical and spectral analyses.

Extraction of Co, Mn, Ni and V associated with amorphous oxide phases in soil

Ammonium oxalate/oxalic acid extractions were conducted to target amorphous phases that served as the host phase for Co, Mn, Ni and V after burn experiments. Ammonium oxalate and oxalic acid extracts target elements sorbed to and coprecipitated with amorphous Fe and Al (oxy)hydroxides (Keon et al., 2001). All extractions were conducted in triplicate on soils, using 0.4 g of unburned or burned soils and 40 mL of a 0.2 M ammonium oxalate/oxalic acid solution in 50-mL HDPE centrifuge tubes. Samples were vortexed then shaken in the dark on an Orbital Shaker SYC-2102A at room temperature for 2 h. After the 2 h incubation period, samples were centrifuged at 2,000 rpm for 15 min. Solutions were then filtered through 1-µm Whatman filter paper, acidified, and stored in the refrigerator. Samples were then diluted 100-fold in 2% HNO_3 and analyzed for Co, Mn, Ni and V on a Spectro-Arcos ICP-OES. The detection limit for Co, Mn, Ni, and V via ICP-OES are 0.68 µg L^{-1}, 0.65 µg L^{-1}, 0.08 µg L^{-1}, and 1.2 µg L^{-1}, respectively.

Extraction of Co, Mn, Ni and V associated with crystalline oxide phases in soil

Citrate-bicarbonate-dithionite (CBD) extractions were conducted to target trace-element contaminants associated with crystalline Fe-(oxy)hydroxides (Mehra & Jackson, 1958). Extractions were conducted on soils from each hillslope position and each temperature previously described. For each sample, 0.4 g of dosed soils were placed into 50 mL HDPE centrifuge tubes along with 20 mL of 0.3 M sodium citrate and 2.5 mL of 1 M sodium bicarbonate. Samples were heated in a hot water bath to 80 °C, and then 0.5 g of sodium dithionite was added. Samples were in the hot water bath for 30 min and shaken intermittently, after which soils were removed and centrifuged at 2,000 rpm for 15 min. Solutions were filtered using 1-μm Whatman filter paper, preserved with concentrated HNO_3, and stored in the refrigerator until analysis. Samples were diluted 100-fold in 2% HNO_3 and analyzed for Co, Ni, Mn, and V via ICP-OES. All analyses were conducted in triplicate.

Environmentally available Co, Mn, Ni, and V in soils

Strong-acid digestions were conducted to quantify "environmentally available" Co, Mn, Ni and V in burned and unburned soils across the serpentine toposequence. The strong-acid digestion, EPA 3050B, is used to extract most of the environmentally available elements from a soil sample (Environmental Protection Agency, 1996). In a 50 mL DigiPREP test tube, 0.5 g of soil, 2.5 mL of 18.2 MW water, and 2.5 mL of 15.8 M nitric acid (HNO_3) were vortexed and left for 16 h with a watch glass. After the 16 h incubation, samples were placed into the DigiPREP digestion block at 95 °C for 15 min, removed, and then cooled for 10 min. After cooling, 2.5 mL of 15.8 M HNO_3 was added, and then samples were vortexed and placed back into the digestion block for 30 min at 95 °C; this step was repeated. After the repetition, samples in the digestion block were heated for 2 h at 95 °C. Once samples were removed and cooled, 1.5 mL of 18.2 MW water and 1 mL of 30% hydrogen peroxide were added to the samples. Samples were then put back into the digestion block with watch glasses and heated to 95 °C, adding 1 mL of 30% hydrogen peroxide when the effervescence stopped from the previous addition. This was done until 5 mL total of 30% hydrogen peroxide was added to each sample. Once the effervescence of the 5 mL of 30% hydrogen peroxide stopped, samples were vortexed and heated uncovered for 2 h at 95 °C. After 2 h, samples were removed, and cooled, and 2.5 mL of 12 M hydrochloric acid

(HCl) was added, and then samples were reheated to 95 °C for 45 min in the digestion block. Afterward, samples were cooled and filtered through 1-µm Whatman paper into 50 mL centrifuge tubes and stored in the refrigerator. Samples were analyzed for Co, Ni, Mn, and V via ICP-OES. All analyses were conducted in triplicate.

Soil column-flow experiments

Soil column experiments were conducted on unburned and burned (400 ° C) soils from each hillslope position (summit, shoulder, backslope, toeslope) to quantify the transport of Co, Mn, Ni, and V under flow conditions. Dried soils were weighed out and packed into columns in duplicate with regular tapping to ensure settling. Experimentation lasted a week, with ~0.4 L of rainwater solution flowing through columns, a volume intended to replicate more than half of the annual precipitation for the field area (annual precipitation ~150 cm; NOAA), given the cross-sectional area of the column soils. After flow experiments were terminated, soils were removed, air-dried, and subjected to solid-phase analyses.

Column experiments were conducted using borosilicate-glass chromatography columns (2.5 x 10 cm Econon-Column BIORAD) fitted with polypropylene and polyethylene tubing. A fixed porous polymer filter was located at the bottom of each column. Each column also had 5 mm of glass wool, 5 mm of sand, and 5 mm of glass wool at each end to ensure an even distribution flow. Column connections were glued to reduce increasing pressure, which ruptured columns during a pilot experiment. A peristaltic pump (Watson Marlow, 323) was used to pump rainwater solution through soil columns, and Watson-Marlow manifold tubing (internal width of 0.25 mm) was used to transport the solution into columns. Column experiments were conducted in duplicate.

The rainwater solution used throughout the column experiment was designed to replicate the atmospheric water of western Oregon. The composition of the rainwater was chosen based on the atmospheric analysis of water in a nearby region (Bormann et al., 1989). The rainwater solution consisted of 1.75 mg L^{-1} of NaCl, 0.8 mg L^{-1} of $MgSO_4^{2-}$, and 0.44 g L^{-1} of KBr, the last of which was added as a conservative tracer. The pH of the rainwater solution was then adjusted to 4.88 before experimentation began.

Soil column effluent was collected throughout the experiment in order to quantify metal transport from unburned and burned (400 °C) soil columns. Effluent was collected every 4 h for

168 h. The collected solutions were filtered through a 1-µm Whatman filter paper, pH was measured (Orion STAR). The solution from each sampling time was acidified and refrigerated until analysis via ICP-OES (as described above). Samples were analyzed for Br, Co, Ni, Mn, and V with a blank every 25 samples to ensure quality control. All samples were analyzed in triplicate.

Soil organic carbon

Soil organic carbon was analyzed for each hillslope position and burn intensity. Soil organic carbon was analyzed using a Fisher Scientific FlashSmart Elemental Analyzer. Sample preparation was conducted by encapsulating 30 mg of soil into tin capsules (4 x 7 mm). A soil reference was analyzed every 10 samples, and a standard was run every 20 samples for quality control and to monitor instrumental drift. All samples were analyzed in duplicate, and the variability in C concentration between replicates was less than < 0.5%.

RESULTS

Cobalt

Chemical extractions of Co from each hillslope position and temperature treatment is presented in the left column of Figure 4.2. Oxalate-extractable Co in unburned soils across the hillslope ranged from 73.4 – 157.5 mg kg^{-1} and was greatest in soils from the summit position and decreased with hillslope position until the toeslope, where there was a slight increase in oxalate-extractable Co (Figure 4.2A and SI Table 4.1). Unburned summit soils had the greatest concentration of oxalate-extractable Co (157.5 mg kg^{-1}), and burned soils had the greatest concentration of oxalate-extractable Co in soils from the 400 ºC summit position (209.5 mg kg^{-1}). Regardless of hillslope position, oxalate-extractable Co decreased in soils heated above 400 ºC. The lowest concentrations of oxalate-extractable Co was in soils from the 800 °C treatment, where oxalate-extractable Co ranged from 11-1.9 mg kg^{-1}. Backslope and toeslope soils had similar concentrations of oxalate-extractable Co with increasing burn intensity.

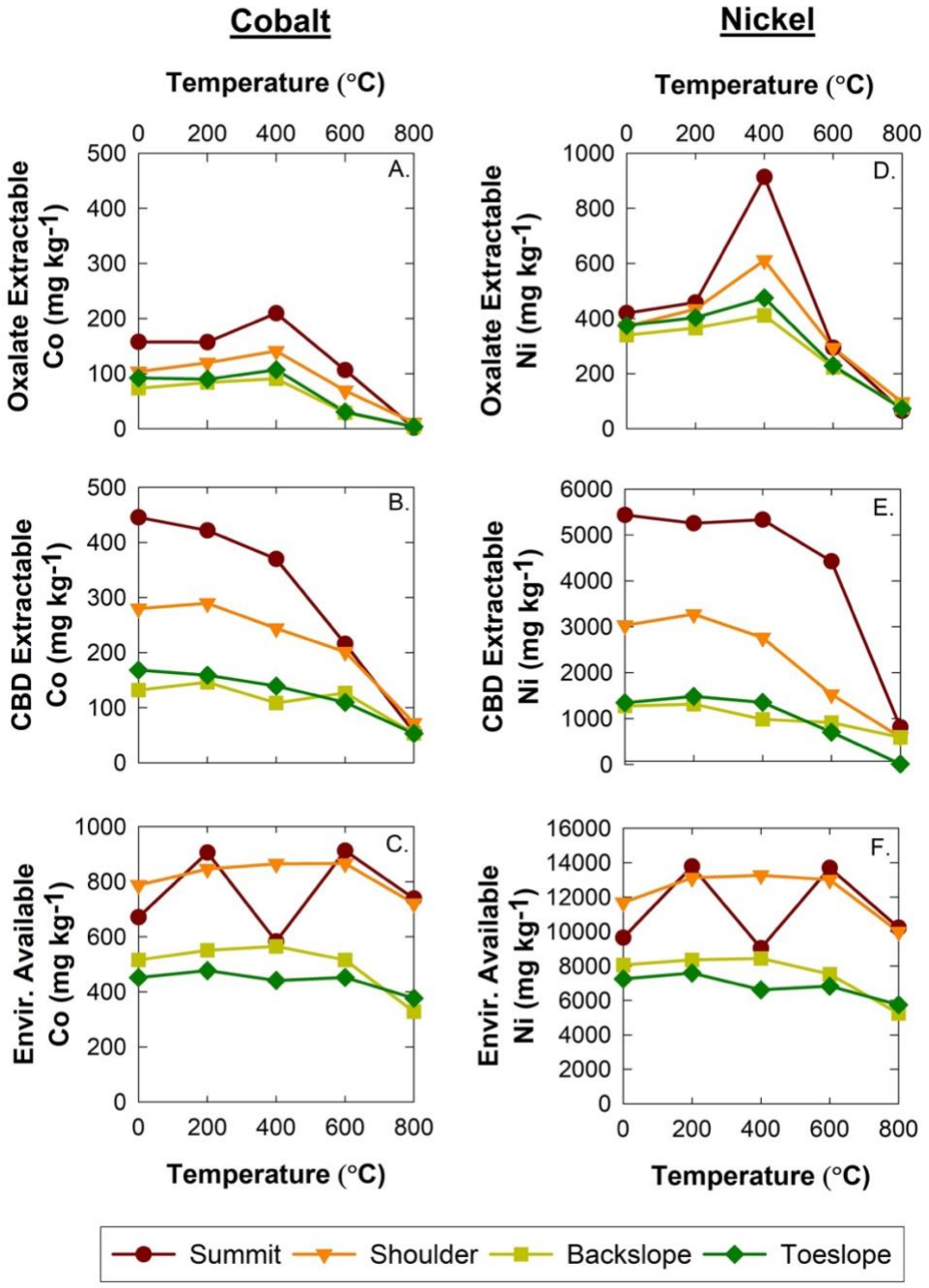

Figure 4.2. Concentrations of cobalt (left column) and nickel (right column) extracted from burned serpentine soils from different positions across a toposequence [summit (red circles), shoulder (orange triangles), backslope (yellow squares), toeslope (green diamonds)]. (top row) Oxalate-extractable Co and Ni; (middle row) CBD-extractable Co and Ni; (bottom row) Co and Ni concentrations after strong-acid digestions. Data points represent averages from experimental triplicate samples. Error bars represent standard error of triplicate measurements; in some cases, error bars are smaller than symbols.

CBD-extractable Co as a function of hillslope position and treatment temperature is presented in Figure 4.2B and SI Table 4.2. In unburned soils, CBD-extractable Co ranged from 131.9 – 445.6 mg kg^{-1}). Burned soils decreased the concentrations of CBD-extractable Co and ranged in concentration (421.89 – 53.02 mg kg^{-1}). Of the burned treatments, summit soils from the 200 ºC treatment had the greatest concentrations of CBD-extractable Co. With increased burn intensity, CBD-extractable Co decreased and was lowest in soils from the 800 ºC treatment and ranged in concentration from 55.02 – 72.15 mg kg^{-1}. Regardless of unburned concentrations, CBD-extractable Co reached similar concentrations in the 800 ºC treatment.

Environmentally available Co from each hillslope position and heating treatment is presented in Figure 4.2C and SI Table 4.3. Unburned soils from the summit position had the greatest concentration of environmentally available Co, followed by the summit, backslope, and then toeslope positions. Environmentally available Co was greatest in soils from the summit position in the 200 °C (905.4 mg kg^{-1}) and 400 °C treatment (582.9 mg kg^{-1}). All soils decreased in environmentally available Co in soils from the 800 °C treatment, and in most cases, soils had less than in the unburned soils, except for the summit position.

Nickel

Chemical extractions of Ni from each hillslope position and temperature treatment are presented in the right column of Figure 4.2. The highest concentration of oxalate-extractable Ni was in summit soils from the 400 °C treatment (913 mg kg^{-1}), followed by the shoulder slope position from the 400 °C treatment (611 mg kg^{-1}) (Figure 4.2D and SI Table 4.1). Aside from 400 °C soils, oxalate-extractable Ni didn't vary greatly among hillslope positions and generally trended towards decreased concentrations as a function of treatment temperature. 800 °C soils had the least oxalate-extractable Ni, ranging from 64 – 96 mg kg^{-1}, regardless of hillslope position.

CBD-extractable nickel from each hillslope position and temperature treatment is presented in Figure 4.2E and SI Table 4.2. Hillslope position influenced the degree of CBD-extractable Ni across the hillslope, with summit soils (5,437 mg kg^{-1}) having the greatest concentration, followed by the shoulder slope. The 400 °C treatment (5,333 mg kg^{-1}) had the highest CBD-extractable Ni in burned soils. Nickel associated with crystalline phases generally decreased with treatment temperature, with the lowest concentrations present in 800 °C soils.

The lowest CBD-extractable Ni concentrations in soils from the 800 ºC-treatment were in the toeslope soils (10 mg kg^{-1}), while the other hillslope positions remained between 810 – 589 mg kg^{-1} of Ni.

Environmentally available Ni from each hillslope position and heating treatment is presented in Figure 4.2F and SI Table 4.3. Unburned soils from the summit position had the greatest concentration of environmentally available Ni, followed by the summit, backslope, and then toeslope positions. Environmentally available Ni was greatest in soils from the summit position from the 200 °C (13,784.5 mg kg^{-1}) and 400 °C treatment (13,275.8 mg kg^{-1}). For all burned soils, environmentally available Ni was least in soils from the 800 °C treatment, with all 800 °C treated soils but those from the summit having less measured for the unburned soils.

Manganese

Chemical extractions of Mn are presented in the right column of Figure 4.3. Oxalate-extractable Mn in unburned soils decreased with hillslope position until the toeslope, which slightly increased (Figure 4.3A and SI Table 4.1). Amorphous-oxide-associated Mn increased from unburned soils to the 400 ºC treatment and thereafter decreased until the 800 ºC treatment. For each hillslope position, the 400 °C treatment had the highest concentration of oxalate-extractable Mn, and the 800 °C treatment had no negligible concentrations of oxalate-extractable Mn.

CBD-extractable Mn from each hillslope position and burn intensity is presented in Figure 4.3B and SI Table 4.2. In unburned soils, crystalline-oxide-associated Mn varied with hillslope position and was greatest in summit soils. In general, burned soils decreased in CBD-extractable Mn that were burned >400 ºC. The highest concentration of CBD-extractable Mn was present in 400 °C soils from the summit position (4,707 mg kg^{-1}), and the second highest concentration was in the unburned summit soils (4,418 mg kg^{-1}). Shoulder slope and toeslope soils decreased in CBD-extractable Mn as a function of increasing temperature treatment; however, toeslope soils had no detectable CBD-extractable Mn in the 800 ºC-soils.

Environmentally available Mn for each hillslope position and burn intensity is presented in Figure 4.3C and SI Table 4.3. In unburned soils, shoulder slope soils had the greatest environmentally available Mn, followed by the summit, backslope, then toeslope. Environmentally available Mn was highest in soils from the shoulder slope position, followed by

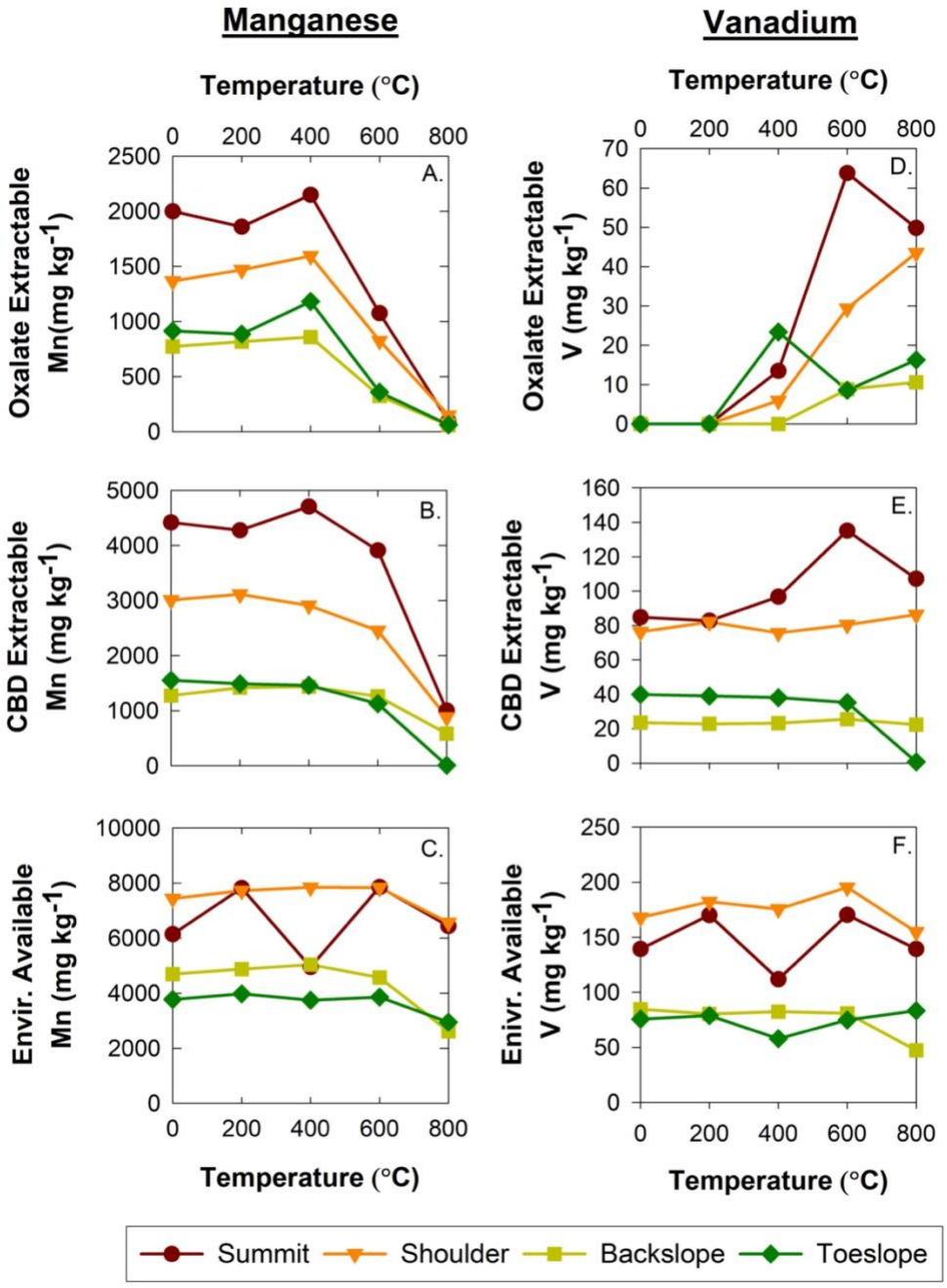

Figure 4.3. Concentrations of manganese (left column) and vanadium (right column) extracted from burned serpentine soils from different positions across a toposequence [summit (red circles), shoulder (orange triangles), backslope (yellow squares), toeslope (green diamonds)]. (top row) Oxalate-extractable Mn and V; (middle row) CBD-extractable Mn and V; (bottom row) Mn and V concentrations after strong-acid digestions. Data points represent averages from experimental triplicate samples. Error bars represent standard error of triplicate measurements; in some cases, error bars are smaller than symbols.

the summit, backslope, and toeslope positions. Summit soils were most influenced by burn intensity and had environmentally available Mn concentrations that substantially decreased in the 400 °C treatment. Regardless of the hillslope position, environmentally available Mn decreased in soils from the 800 °C treatment, with all soils but the summit position having less Mn than the unburned soils.

Vanadium

Chemical extractions of V is presented in the right column of Figure 4.3. Oxalate-extractable vanadium was not detected in the unburned- and 200 °C soils regardless of hillslope position (Figure 4.3D and SI Table 4.1). The highest concentration of oxalate-extractable V was in summit soils from the 600 °C treatment (63.7 mg kg^{-1}) followed by the summit soil from the 800 °C treatment (49.8 mg kg^{-1}). Shoulder-slope soils increased in oxalate-extractable V in the 200 °C treatment and was highest in the 800 °C treatment (43.5 mg kg^{-1}). Soils from the backslope position only had oxalate-extractable V in the 600 °C and 800 °C treatment, 8.8 mg kg^{-1} and 10.6 mg $kg^{-1,}$ respectively. Soils from the toeslope position had a maximum oxalate-extractable V concentration in the 400 °C treatment (23.3 mg kg^{-1}).

CBD-extractable V from each hillslope position and heating treatment is presented in Figure 4.3E and SI Table 4.2. CBD-extractable V was detected in all unburned soils and ranged in concentration from, 84.9 to 23.4 mg kg^{-1} in decreasing order: summit > shoulder > toeslope > backslope. CBD-extractable V was highest in 600 °C soils from the summit position (135.1 mg kg^{-1}), thereafter decreasing in the 800 °C treatment. Concentrations of CBD-extractable V from shoulder and backslope soils varied minimally as a function of treatment temperature. The toeslope position varied minimally in crystalline-oxide-associated V until the 800 °C treatment, where no V was detected.

Environmentally available V concentrations as a function of hillslope position varied with burn intensity (Figure 4.3F and SI Table 4.3). In unburned soils, the shoulder slope position had the greatest concentration of V (167.9 mg kg^{-1}), followed by the summit (139.2 mg kg^{-1}), backslope (84.5 mg kg^{-1}), and lastly, toeslope (75.6 mg kg^{-1}). Soils from the 200 °C treatment had a similar relationship with the hillslope position, where the shoulder slope had the greatest available V, and the toeslope and backslope positions had a similar concentration of environmentally available V. In the 400 ºC treatment, environmentally available V substantially

decreased in soils from the summit position and toeslope positions. Environmentally available V in soils from the 600 ºC treatment increased in soils from the 400 ºC treatment. Thereafter, soils from the 800 ºC treatment slightly decreased in environmentally available V, except for the toeslope, which increased slightly.

Transport of contaminants from burned soils

Cobalt, Mn, Ni, and V released and transported from unburned serpentine soils as a function of hillslope position are presented in Figure 4.4 and Table 4.1. Contaminants transported from unburned soils lacked a clear relationship with hillslope position (left column of Figure 4.4). Cobalt and V were present at low concentrations in effluent of unburned soils and resulted in 0.01 - 0.09 mg kg^{-1} of Co and 0 – 2.65 mg kg^{-1} of V being released. Mn was released from unburned soils at concentrations that ranged from 0.49-5 mg kg^{-1}. Unburned soils from the hillslope positions analyzed lost between 9.59 – 1.67 mg kg^{-1} Ni in the column experiments, with the most Ni released from the shoulder slope soils.

Cobalt, Mn, Ni, and V released from burned (400 ºC) serpentine soils as a function of hillslope position are presented in Figure 4.4 (right column) and Table 4.1. Burned soils released higher amounts of Ni than did unburned soils. The average cumulative concentration of Ni released from burned soils ranged from 7.92 – 19.42 mg kg^{-1}, with the greatest Ni loss from the toeslope soils. Manganese concentrations varied from unburned to burned soils; Mn release was greater from unburned soils than those for burned soils for summit and backslope samples but was greater in burned soils from the shoulder and toeslope positions. Cumulative concentrations of Co released from burned soils were greater than those for unburned soils, ranging from 0.08 – 0.56 mg kg^{-1}. Finally, V concentrations in effluent from burned soils were undetectable regardless of hillslope position.

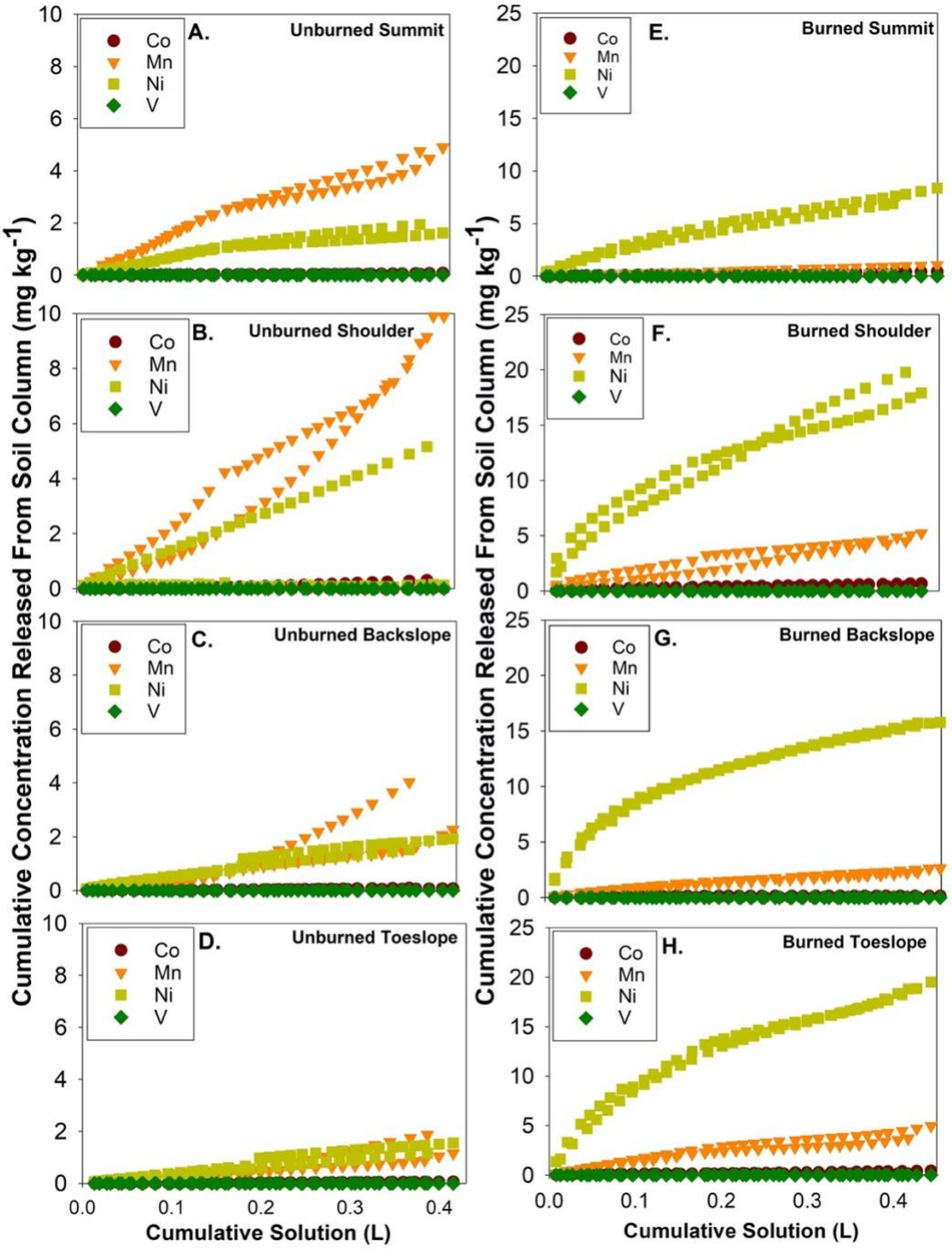

Figure 4.4. Cumulative concentrations of Co (red circles), Mn (orange upside-down triangle), Ni (yellow square), and V (green diamond) from unburned (left column) and 400 °C (right column). Serpentine soil columns from different positions across a toposequence in duplicate. Rainwater solutions consisted of 1.75 mg L^{-1} of NaCl, 0.8 mg L^{-1} of $MgSO_4^{2-}$, and 0.44 g L^{-1} of KBr (conservative tracer SI Figure 3.10). Packed soil columns had a flow rate of 4 mL hr^{-1}, and a total of 0.4 L solution was flushed through each column.

Table 4.1. Cumulative (total) Co, Mn, Ni, and V concentrations from unburned and 400 ºC burned soils released from column experiments. Concentrations were measured via ICP-OES.

Samples name	Tot. Co ($mg\ kg^{-1}$)	Tot. Mn ($mg\ kg^{-1}$)	Tot. Ni ($mg\ kg^{-1}$)	Tot. V ($mg\ kg^{-1}$)
Unburned Summit	0.06	5.00	1.80	0
Unburned Shoulder	0.01	0.49	9.59	0
Unburned Backslope	0.09	3.14	1.72	0
Unburned Toeslope	0.00	2.01	1.67	0
400 °C Summit	0.30	0.72	7.92	0
400 °C Shoulder	0.56	4.87	18.86	0
400 °C Backslope	0.08	3.00	17.27	0
400 °C Toeslope	0.28	4.44	19.42	0

DISCUSSION

Role of hillslope position and burn intensity on serpentine soil metal availability

Soil weathering across the hillslope governed the forms and distributions of contaminants found in unburned soils (Figure 4.2; 4.3). Hillslope position drove the abundance of amorphous- and crystalline-oxide-associated Co, Mn, Ni and V, along with the environmentally available concentrations. In unburned soils, contaminants associated with amorphous-mineral phases decreased with hillslope position until the toeslope, where there was a slight increase in amorphous-associated contaminants (amorphous-associated V was not detected in unburned soils regardless of hillslope position). A similar relationship with hillslope position was also observed with crystalline-oxide-associated contaminants. In unburned soils, environmentally available concentrations of contaminants were greatest in the shoulder slope position, followed by the summit, backslope, then toeslope.

Concentrations of amorphous- and crystalline-oxide-associated Co, Mn, Ni, and V across the hillslope varied with burn intensity. Across the suite of contaminants investigated, 400 ºC burned soils had the highest concentrations of amorphous-associated contaminants, thereafter decreasing to negligible concentrations. The percentage of contaminants found with crystalline-

oxide forms progressively decreased with higher burn intensities (>600 ºC), even as overall concentrations of environmentally available contaminants generally stayed the same (except 400 ºC summit soils). The exception was amorphous- and crystalline-oxide-associated V, which was highest in the 600 ºC treatment from the summit position. Transformations observed with burn intensity highlight the solid-host phase repartitioning of minerals and new mineral development with burn intensity, as previously discussed in Chapter 3 and as is discussed for individual contaminants below.

Cobalt

Burn intensity decreased amorphous and crystalline-oxide-associated Co in soils, and minimal concentrations were leached from burned soils (Figure 4.2; 4.4). Amorphous and crystalline-oxide-associated Co decreased with burn intensity >400 ºC, possibly due to the Fe-mineral transformations with fire. In soils, Co is often co-precipitated with iron hydroxides and structurally substituted into Fe (oxyhydr)oxides and clay minerals (Ziwa et al., 2020). Our data illustrate that Fe-mineral hosts (amorphous or crystalline) transform with burn intensity (>600 ºC) towards spinel-group minerals (Ch 3; Table 3.1), which can incorporate Co into forms that are not targeted by the techniques employed (CBD and strong-acid extractions). Co concentrations exceeded the residential and industrial soil quality guidelines set by the USEPA, 23 mg kg^{-1} and 300 mg kg^{-1}, respectively (Strawn and USEPA 2013, Ziwa et al., 2020), and across the suite of soils investigated, ranged from 327 to 905 mg kg^{-1} of Co. However, transport experiments revealed that only trace amounts of Co were released from burned soils (0.08 – 0.56 mg kg^{-1} of cumulative Co), suggesting a relatively low mobility of Co, after burning, indicating that Co may be less of a concern for water quality than for soil quality.

Wildfires can influence Co reactivity, and Co has been detected in post-fire soils and ash. One study conducted in post-fire soils in Portugal found that there was no variation in Co concentration in burned uncontaminated soils (Campos et al., 2016), while another study found Co associated with large soil particles and enriched from unburned soils after a fire in the wildland-urban interface (Magliozzi et al., 2024). Additionally, Co has been detected in wildfire ash, which could increase Co concentrations in soils after deposition (Costa et al., 2014). Although results vary from field studies, if Co concentrations are high or within the windblown fraction of soil and ash, it could threaten soil, water, and air quality. Furthermore, Co fate may

differ after fire in areas next to industrial sites where Co concentrations can be high and sorbed to different mineral phases than geogenic contaminated soils (Ziwa et al., 2020).

Nickel

Nickel reactivity associated with pedogenic minerals generally decreased with increasing burn intensity, except for 400 ºC soils. Amorphous associated Ni was generated at the 400 ºC burn intensity, thereafter crystalline and amorphous associated Ni decreased with increasing burn intensity (>400 ºC). Nickel-bearing minerals in serpentine soils are generally spinel group minerals, clay minerals (mainly of the smectite group), and Fe and Mn (oxy)hydroxides (Caillaud et al., 2009; Chardot et al., 2007; Kierczak et al., 2016; Quantin et al., 2008); Ni distribution and mobility in soils are further influenced by organic matter however, organic matter was low in 400 ºC-burned soils (SI Figure 3.8) (Kabata-Pendias & Pendias, 2011). Other studies have also highlighted the affinity of Ni with Fe and Mn amorphous minerals in soils, which decreases with the increasing crystallinity of minerals (i.e., high affinity for goethite and lower affinity for hematite) (Bani et al., 2014; Echevarria, 2018). Our data further show that environmentally available Ni concentrations were high, with concentrations ranging from 5,242 to 13,784 mg kg^{-1} across the suite of temperatures and hillslope positions, values that are well above the soil quality index for Ni (50 to 600 mg kg^{-1} USEPA (Directive, 2007)).

In addition to soil contamination with Ni, Ni was released and transported from all burned soils at concentrations exceeding drinking water standards. Burned soils released Ni into soil pore water at concentrations that exceeded drinking water standards for the duration of the experiment (MCL is 0.1 mg L^{-1}). Cumulative concentrations of Ni released from burned columns were highest in soils in the following order: toeslope, shoulder, backslope, and summit position. Transport of Ni from unburned serpentine soils is generally attributed to release during Fe and Mn (hydr)oxide mineral transformations (Morrison et al., 2015); we speculate that as these mineral phases transform with burn intensity, Ni sorption decreases, increasing Ni mobility. Thereafter, with increasing burn intensity (>400 ºC), Ni is incorporated into new minerals such as nichromite at 800 ºC (Chapter 3).

Our results do not include ash, and we speculate that Ni accumulating plant species endemic to serpentine soils could increase Ni concentrations and mobility. In fact, Ni enrichment in ash has been detected in burned nonserpentine-landscape (Abraham et al., 2017; Kumar &

Maiti, 2013; Mandal & Sengupta, 2006; Roshan & Biswas, 2023) Additionally, Ni enrichment in soil and ash across post-fire landscapes has been detected (Bogacz et al., 2011; Mandal & Sengupta, 2006; Plumlee et al., 2007; Stankov Jovanovic et al., 2011). These studies suggest that Ni remobilization and subsequent deposition can contaminate soils after fire in areas with high concentrations of Ni (anthropogenic and geogenic) and in environments that are not contaminated. Although Ni concentrations were relatively low in these studies compared to our data, discrepancies can likely be attributed to elevated concentrations found in unburned serpentine soils, which are driven by the weathering of nickeliferous parent materials.

Manganese

Our data reveal that pedogenic secondary oxide minerals associated with Mn decrease as the burn intensity increases. Decreased associations of Mn with secondary minerals were observed regardless of the hillslope position, and the lowest amounts of Mn associated with amorphous and crystalline phases were recorded in the 800 ºC treatment. In serpentine soils, Mn is typically associated with oxides and (oxy)hydroxides, which are transformed with burn intensity. Previous studies have shown that secondary mineral-associated Mn decreases with increasing burn intensity, suggesting that it transforms into more crystalline phases, such as Mn-oxides (Gonzalez Parraa et al., 1996; Norouzi & Ramezanpour, 2013; Rajapaksha et al., 2012; Roshan & Biswas, 2023). Pyrogenic Mn minerals have also been shown to be rather reactive, which agrees with our findings.

Regardless of the hillslope position, Mn was released from burned soils to create porewater concentrations that exceed drinking water standards. Using the U.S. Environmental Protection Agency SMCL, our data reveal that unburned and burned soils released high concentrations of Mn for the duration of the column experiments. Transported Mn was greatest in unburned soils from the summit position and for burned soils, was greatest in the shoulder slope position. In burned soils, Mn was released from highest to lowest in the following order: shoulder slope, toeslope, backslope, and summit (mass normalized).

Our findings of Mn mobility in burned soils agree with studies that have investigated Mn mobility in post-fire environments. Manganese contamination from burned landscapes has generally been attributed to the addition of Mn-rich ash (Abraham et al., 2018; Campos et al., 2016; Campos et al., 2015; Gonzalez Parraa et al., 1996; Roshan & Biswas, 2023). Our findings

illustrate that burned soils can increase Mn availability without ash and threaten soil pore water. Furthermore, research has observed increased Mn concentrations by 279% in 400 ºC burnt soils within the water-soluble fraction (Chambers & Attiwill, 1994). Additional studies have noted a sharp decline in soil Mn after the first rainfall in post-fire landscapes, which was attributed to the greater mobility and easier desorption by ion exchange (Harrison et al., 1982).

Vanadium

Vanadium reactivity with burn intensity had a different relationship than other contaminants investigated and was not detected in burned soil column effluent. Results highlight the unique relationship between burn intensity and V repartitioning in soils, particularly in the oxalate-extractable fraction, where V increased with burn intensity (>200 ºC). In the 200 ºC treatment, oxalate-extractable V was still minimally generated, possibly due to the presence of organic matter creating reduced conditions and/or pH control (SI Figure 3.7; SI Figure 3.8). Amorphous-associated V was also a substantial portion of the environmentally available V, particularly at the 600 °C treatment. Vanadium in soils is generally associated with Fe and Mn (oxy)hydroxides, which generally decrease with increased burn intensity (Chapter 2). The generation of V associated with amorphous phases with increasing burn intensity may mean that V was released from mineral phases and sorbed onto newly generated secondary minerals. However, V was not released from burned soils, indicating that the amorphous and crystalline associated V that increased with burn intensity was not mobile.

Although understudied in post-fire landscapes (Roshan & Biswas, 2023), V has been detected in post-fire ultramafic soils, and solid-phase concentrations were found to be above the maximum contaminant levels (Alexakis, 2020). Furthermore, fires have been considered in the global cycling of V. Wildfires are a source of V in the atmosphere, estimated between 1.8 × 109 g y^{-1} and 13 × 109 g y^{-1}, where vegetation burning can deposit V onto soils (Schlesinger et al., 2017). Since V repartitioning differed from the other contaminants analyzed in our investigation, the mechanism of V mobility with fire should be further investigated.

Nickel and manganese threats to water quality

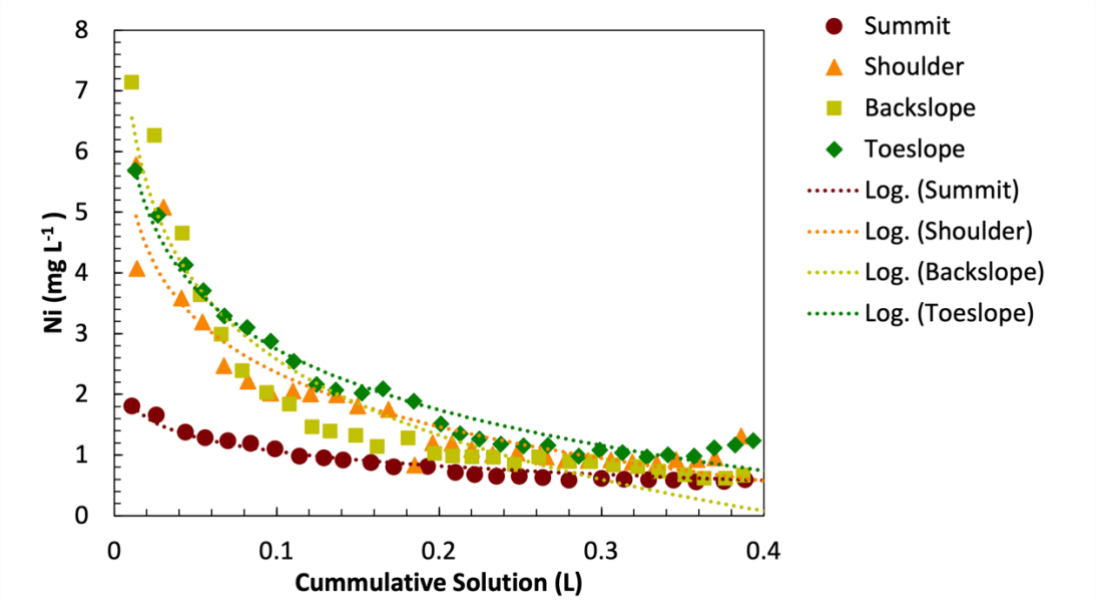

Figure 4.5. Concentrations of Ni in solution (mg L^{-1}) in column effluent for burned (400 ºC) soils from each hillslope position (summit is presented in red circles, shoulder slope in orange triangles, backslope in green diamonds, and toeslope in blue squares). Logarithmic decay equations were used to fit the data and estimate how long effluent Ni concentrations would persist above the USEPA maximum contaminant level (MCL) for Ni (0.1 mg L^{-1}). Equations derived from line of best fit are presented in Table 4.2.

Based on experimental results and fitting effluent concentrations with logarithmic decay curves, we estimated elevated concentrations of Ni and Mn in soil porewater. Nickel and manganese released from 10 cm of soil could persist 0.51 - 2.13 y for Ni and 1.48 – 4.11E+11 y for Mn. The predicted persistence of Ni in the environment depends on landscape position, with 2.13 years for summit soils, 0.76 years for shoulder slope, 0.51 years for backslope, and 0.81 years for toeslope soils. The predicted persistence of Mn in the environment also depends on landscape position, with 4.11E+11 years for summit soils, 1.65 years for shoulder slope, 1.48 years for backslope, and 2.36 years for toeslope soils. Although it is unlikely for Mn to be released for 4.11E+11 y due to solid-phase Mn surely diminishing, these predictions highlight the persistence of Mn that can be released from serpentine soils. However, unburned and burned soils from the summit position release Mn at concentrations exceeding drinking water standards (SI Figure 4.1). Although these predictions are based on experimental results and would probably vary in the environment, they exemplify that the impact of fire on soil and water quality

can be long-lasting. In fact, elevated contaminant concentrations in soil and water resources have been detected at hazardous levels (Abraham et al., 2017; Costa et al., 2014; Magliozzi et al., 2024; Stein et al., 2012).

Our results provide valuable insights into contaminant repartitioning and subsequent transport from burned soils based on burn intensity and hillslope position. Previous studies on this topic have relied on static experiments or limited field measurements after fire (Burton et al., 2019; Burton et al., 2019; Gonzalez Parraa et al., 1996; Lopez et al., 2023; Panichev et al., 2008; Roshan & Biswas, 2023; Sandeep et al., 2019); therefore, we contribute towards our conceptual understanding of the risk posed to soil and water quality across a post-fire landscape. Our data help clarify the environmental threats posed to a watershed where geogenic contamination exists and quantifies the potential persistence after fire, helping us improve our understanding of fire-induced contamination fate and considerations for potential post-fire recovery strategies (discussed in Chapter 2).

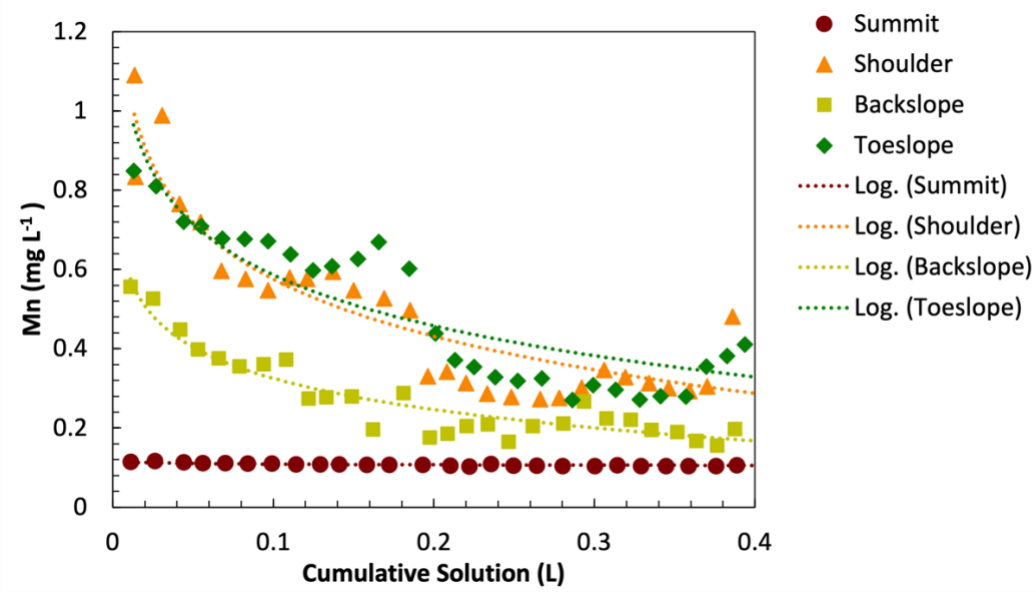

Figure 4.6. Concentrations of Mn in solution (mg L^{-1}) in column effluent for burned (400 ºC) soils from each hillslope position (summit is presented in red circles, shoulder slope in orange triangles, backslope in blue diamonds, and toeslope in blue squares). Logarithmic decay equations were used to fit the data and estimate how long effluent Mn concentrations would persist above the USEPA SMCL for Mn (0.05 mg L^{-1}). Equations derived from line of best fit are presented in Table 4.2.

Table 4.2. Estimated time needed for each hillslope position (summit, shoulder, backslope, and toeslope) to flush Ni and Mn so concentrations drop below the MCL for Ni (0.1 mg L^{-1}) and Mn (0.05 mg L^{-1}). The estimated time (years) needed to reach MCL levels were calculated using logarithmic decay best-fit lines of experimental data (Figures 4.5 and 4.6) and are presented below assuming average annual precipitation of 153.94 cm, and normalizing column inflow volumes to a cross-sectional area of 4.9 cm^2.

Nickel		
Hillslope	**Time (yr)**	**Equation used based on the line of best fit**
Summit	2.13	$y = -0.344\ln(x) + 0.2665$
Shoulder	0.76	$y = -1.286\ln(x) - 0.6013$
Backslope	0.51	$y = -1.801\ln(x) – 1.5718$
Toeslope	0.81	$y = -1.44\ln(x) – 0.5805$
Manganese		
Hillslope	**Time (yr)**	**Equation used based on the line of best fit**
Summit	N/A	$y = -0.002\ln(x) + 0.1034$
Shoulder	1.65	$y = -0.208\ln(x) +0.0968$
Backslope	1.48	$y = -0.114\ln(x) + 0.0635$
Toeslope	2.36	$y = -0.186\ln(x) + 0.1588$

CONCLUSIONS

Wildfire-induced contamination is an important pathway for soil and water degradation. Weathering across a hillslope drives the distribution and mineral associations of Co, Mn, Ni, and V that can be transformed by fire. This study investigated heat-induced contaminant transformations and transport from serpentine soils as a function of hillslope position. Chemical extractions investigating the repartitioning of contaminants across the hillslope and with burn intensity illustrate that Co, Mn and Ni decrease associations with secondary minerals and transform toward more crystalline phases. Furthermore, transport experiments on burned soils illustrate that Mn and Ni can be released into soil pore water at concentrations that exceed drinking water standards with persistence dependent on the hillslope position. Future research could use pyrocosms, prescribed fires, and post-fire monitoring to further investigate contaminant fate in post-fire environments.

Overall, our findings can aid in identifying priority locations for field sampling and confirming and expanding existing knowledge of flame-induced contamination and reactivity

after a wildfire. Moreover, our study can inform the development of strategies for post-fire remediation efforts, such as erosion prevention across a watershed. Specifically, we recommend prioritizing erosion prevention in soils from the summit position, which can potentially mobilize Mn and Ni. Employing erosion control measures like mulching, direct seeding, and site stabilization can help reduce the potential risk to water sources. Furthermore, these measures may introduce additional nutrients to the soil, reducing the presence of contaminants or their physical stabilization through increased organic matter. Lastly, we encourage federal agencies conducting post-fire landscape assessments to include soil contaminants in their assessments to better manage and monitor contaminant fate in the environment.

SOURCES OF FINANCIAL SUPPORT

This work was supported by the National Institute of Health through the National Institute of Environmental Health Sciences under Grant No. NIH-5P42ES031007-02 and the University of Oregon. Use of the Stanford Synchrotron Radiation Lightsource, SLAC National Accelerator Laboratory, is supported by the U.S. Department of Energy, Office of Science, Office of Basic Energy Sciences under Contract No. DE-AC02-76SF00515.

ACKNOWLEDGMENTS

We thank Fatai Balogun and Owen Duckworth for supporting the conceptualization of this work; Sam Webb, Nicholas Strange, and Erik Nelson for helping gather data at the Stanford Synchrotron Radiation Lightsource; Lev Zakharov for XRD support; Emily Huckstead for helping gather carbon data: and Chris Russo and Jesse Muratli at Oregon State University for helping gather ICP-OES data.

SUPPLEMENTAL MATERIALS FOR CHAPTER IV

Supplemental Tables

SI Table 4.1. Results of oxalate extractions that target amorphous-associated contaminants for each hillslope position and burn intensity were analyzed for Co, Mn, Ni, and V via ICP-OES.

Hillslope Position	Burn Intensity (°C)	Co (mg kg^{-1})	Mn (mg kg^{-1})	Ni (mg kg^{-1})	V (mg kg^{-1})
Summit	0	157.6	2000.9	419.7	0.0
Shoulder	0	103.6	1366.8	371.8	0.0
Backslope	0	73.4	773.8	339.8	0.0
Toeslope	0	92.1	915.5	374.7	0.0
Summit	200	157.1	1860.2	458.6	0.0
Shoulder	200	119.6	1468.9	434.0	0.0
Backslope	200	83.9	817.2	365.6	0.0
Toeslope	200	89.6	885.6	403.1	0.0
Summit	400	209.6	2150.8	914.0	13.5
Shoulder	400	141.1	1595.0	611.7	5.9
Backslope	400	90.9	859.8	411.2	0.0
Toeslope	400	107.0	1181.4	475.0	23.4
Summit	600	106.4	1075.8	293.9	63.8
Shoulder	600	69.0	825.9	293.8	29.4
Backslope	600	28.9	323.9	222.8	8.8
Toeslope	600	30.2	359.0	229.3	8.6
Summit	800	1.9	95.5	64.6	49.8
Shoulder	800	11.1	148.7	96.4	43.5
Backslope	800	3.8	59.4	78.1	10.6
Toeslope	800	3.8	62.4	73.1	16.3

SI Table 4.2. Results of citrate-bicarbonate-dithionite extractions that target crystalline-associated contaminants for each hillslope position and burn intensity were analyzed for Co, Mn, Ni, and V via ICP-OES.

Hillslope Position	Burn Intensity (°C)	Co ($mg\ kg^{-1}$)	Mn ($mg\ kg^{-1}$)	Ni ($mg\ kg^{-1}$)	V ($mg\ kg^{-1}$)
Summit	0	445.6	4418.3	5437.4	84.9
Shoulder	0	280.0	3012.1	3032.2	76.4
Backslope	0	132.0	1273.7	1270.4	23.5
Toeslope	0	168.2	1552.0	1342.2	39.9
Summit	200	421.9	4277.2	5257.7	82.8
Shoulder	200	289.7	3113.9	3275.5	82.1
Backslope	200	146.0	1415.9	1314.0	22.8
Toeslope	200	158.7	1487.4	1480.1	39.0
Summit	400	370.1	4707.9	5333.5	96.7
Shoulder	400	244.2	2912.2	2763.5	75.8
Backslope	400	108.3	1436.5	983.6	23.2
Toeslope	400	139.3	1458.0	1351.9	38.1
Summit	600	215.9	3913.3	4428.6	135.2
Shoulder	600	201.3	2454.0	1525.5	80.5
Backslope	600	126.7	1261.6	909.8	25.6
Toeslope	600	109.4	1126.5	702.9	35.2
Summit	800	55.3	1000.4	810.2	107.2
Shoulder	800	72.2	881.2	593.7	86.4
Backslope	800	53.0	582.5	589.7	22.4
Toeslope	800	53.0	8.9	10.4	0.7

SI Table 4.3. Results of strong acid digestions that target environmentally available contaminants for each hillslope position and burn intensity were analyzed for Co, Mn, Ni, and V via ICP-OES.

Hillslope Position	Burn Intensity (°C)	Co (mg kg^{-1})	Mn (mg kg^{-1})	Ni (mg kg^{-1})	V (mg kg^{-1})
Summit	0	670.8	6141.3	9644.1	139.3
Shoulder	0	787.3	7433.8	11683.9	167.9
Backslope	0	515.8	4689.7	8058.2	84.6
Toeslope	0	451.8	3772.7	7251.2	75.6
Summit	200	905.4	7817.6	13784.8	170.1
Shoulder	200	846.1	7721.1	13124.5	182.3
Backslope	200	550.8	4873.0	8350.2	80.3
Toeslope	200	477.2	3977.7	7590.7	78.9
Summit	400	663.3	5327.8	9584.8	134.9
Shoulder	400	864.7	7841.9	13275.8	175.5
Backslope	400	565.2	5034.5	8434.4	82.4
Toeslope	400	441.1	3742.8	6613.8	57.8
Summit	600	912.2	7852.6	13701.6	170.3
Shoulder	600	866.1	7830.3	13011.1	195.3
Backslope	600	515.8	4568.0	7529.2	80.9
Toeslope	600	452.4	3857.4	6830.3	74.8
Summit	800	738.8	6439.8	10221.4	139.2
Shoulder	800	720.8	6560.5	9989.5	154.7
Backslope	800	327.9	2617.3	5243.0	47.3
Toeslope	800	376.8	2943.3	5740.4	83.3

Supplemental Figures

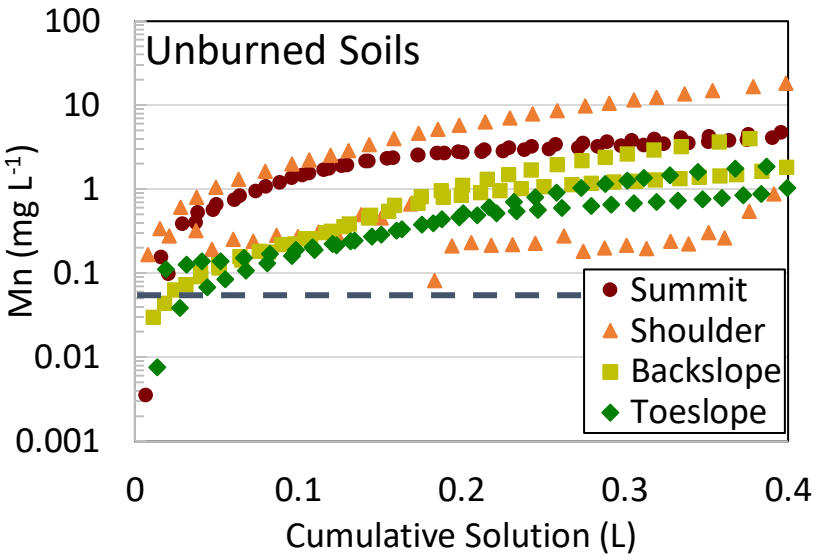

SI Figure 4.1. Concentrations of Mn in solution (mg L^{-1}) in column effluent for unburned soils from each hillslope position (summit is presented in red circles, shoulder slope in orange triangles, backslope in green diamonds, and toeslope in blue squares). The blue line represents the USEPA SMCL for Mn (0.05 mg L^{-1}).

REFERENCES

Abatzoglou, J. T., & Williams, A. P. (2016). Impact of anthropogenic climate change on wildfire across western US forests. *Proceedings of the National Academy of Sciences of the United States of America*, *113*(42), 11770–11775. https://doi.org/10.1073/pnas.1607171113

Abraham, J., Dowling, K., & Florentine, S. (2017). Risk of post-fire metal mobilization into surface water resources: A review. In *Science of the Total Environment* (Vols. 599–600, pp. 1740–1755). Elsevier B.V. https://doi.org/10.1016/j.scitotenv.2017.05.096

Abraham, J., Dowling, K., & Florentine, S. (2018). Influence of controlled burning on the mobility and temporal variations of potentially toxic metals (PTMs) in the soils of a legacy gold mine site in Central Victoria, Australia. *Geoderma*, *331*, 1–14. https://doi.org/10.1016/j.geoderma.2018.06.010

Alexakis, D. E. (2020). Contaminated land by wildfire effect on ultramafic soil and associated human health and ecological risk. *Land*, *9*(11), 1–16. https://doi.org/10.3390/land9110409

Bani, A., Echevarria, G., Montargès-Pelletier, E., Gjoka, F., Sulçe, S., & Morel, J. L. (2014). Pedogenesis and nickel biogeochemistry in a typical Albanian ultramafic toposequence. *Environmental Monitoring and Assessment*, *186*(7), 4431–4442. https://doi.org/10.1007/s10661-014-3709-6

Baumeister, J. L., Hausrath, E. M., Olsen, A. A., Tschauner, O., Adcock, C. T., & Metcalf, R. V. (2015). Biogeochemical weathering of serpentinites: An examination of incipient dissolution affecting serpentine soil formation. *Applied Geochemistry*, *54*, 74–84. https://doi.org/10.1016/j.apgeochem.2015.01.002

Bogacz, A., Woźniczka, P., & Łabaz, B. (2011). Concentration and pools of heavy metals in organic soils in post-fire areas used as forests and meadows. *Journal of Elementology*, *16*(4), 515–524. https://doi.org/10.5601/jelem.2011.16.4.01

Bullard, V. (2005). *Weathering of Serpentine Minerals across a Climate Gradient and Toposequence*.

Burton, E. D., Choppala, G., Karimian, N., & Johnston, S. G. (2019). A new pathway for hexavalent chromium formation in soil: Fire-induced alteration of iron oxides. *Environmental Pollution*, *247*, 618–625. https://doi.org/10.1016/j.envpol.2019.01.094

Burton, E. D., Choppala, G., Vithana, C. L., Karimian, N., Hockmann, K., & Johnston, S. G. (2019). Chromium(VI) formation via heating of Cr(III)-Fe(III)-(oxy)hydroxides: A pathway for fire-induced soil pollution. *Chemosphere*, *222*, 440–444. https://doi.org/10.1016/j.chemosphere.2019.01.172

Caillaud, J., Proust, D., Philippe, S., Fontaine, C., & Fialin, M. (2009). Trace metals distribution from a serpentinite weathering at the scales of the weathering profile and its related weathering microsystems and clay minerals. *Geoderma*, *149*(3–4), 199–208. https://doi.org/10.1016/j.geoderma.2008.11.031

Campos, I., Abrantes, N., Keizer, J. J., Vale, C., & Pereira, P. (2016). Major and trace elements in soils and ashes of eucalypt and pine forest plantations in Portugal following a wildfire. *Science of the Total Environment*, *572*, 1363–1376. https://doi.org/10.1016/j.scitotenv.2016.01.190

Campos, I., Vale, C., Abrantes, N., Keizer, J. J., & Pereira, P. (2015). Effects of wildfire on mercury mobilisation in eucalypt and pine forests. *Catena*, *131*, 149–159. https://doi.org/10.1016/j.catena.2015.02.024

Chambers, D. P., & Attiwill, P. M. (1994). The Ash-bed Effect in Eucalyptus Forest: Chemical, Physical and Microbiological Changes in Soil after Heating or Partial Sterilisation. *Australian Journal of Botany*, *42*, 739–749.

Chardot, V., Echevarria, G., Gury, M., Massoura, S., & Morel, J. L. (2007). Nickel bioavailability in an ultramafic toposequence in the Vosges Mountains (France). *Plant and Soil*, *293*(1–2), 7–21. https://doi.org/10.1007/s11104-007-9261-1

Cheng, C.-H., Jien, S.-H., Iizuka, Y., Tsai, H., Chang, Y.-H., & Hseu, Z.-Y. (2011). Pedogenic Chromium and Nickel Partitioning in Serpentine Soils along a Toposequence. *Soil Science Society of America Journal*, *75*(2), 659–668. https://doi.org/10.2136/sssaj2010.0007

Costa, M. R., Calvão, A. R., & Aranha, J. (2014). Linking wildfire effects on soil and water chemistry of the Marão River watershed, Portugal, and biomass changes detected from Landsat imagery. *Applied Geochemistry*, *44*, 93–102. https://doi.org/10.1016/j.apgeochem.2013.09.009

Directive, O. (2007). *Ecological Soil Screening Levels for Nickel Interim Final*.

Dube, O. P. (2009). Linking fire and climate: interactions with land use, vegetation, and soil. *Current Opinion in Environmental Sustainability*, *1*(2), 161–169. https://doi.org/10.1016/j.cosust.2009.10.008

Echevarria, G. (2018). *Genesis and Behaviour of Ultramafic Soils and Consequences for Nickel Biogeochemistry* (pp. 135–156). https://doi.org/10.1007/978-3-319-61899-9_8

Environmental Protection Agency, U. (1996). *METHOD 3050B ACID DIGESTION OF SEDIMENTS, SLUDGES, AND SOILS 1.0 SCOPE AND APPLICATION*.

Gonzalez Parraa, J., Rivero, V. C., & Lopeza, T. I. (1996). Forms of Mn in soils affected by a forest fire. In *The Science of the Total Environment* (Vol. 181).

Harper, G. (1984). The Josephine ophiolite, northwestern California. *Geological Society of America Bulletin*, *95*(9), 1009. https://doi.org/10.1130/0016-7606(1984)95<1009:TJONC>2.0.CO;2

Harrison, H., Larson, T. V, & Monkman, C. S. (1982). Aqueous phase oxidation of sulfites by ozone in the presence of iron and manganese. *Atmospheric Environment*, *16*(5), 1039–1041.

Hotz, P. E. (1964). *NICKELIFEROUS LATERITES IN SOUTHWESTERN OREGON AND NORTHWESTERN CALIFORNIA* •.

John-Paul Oze, C. (2003). *CHROMIUM GEOCHEMISTRY OF SERPENTINITES AND SERPENTINE SOILS*.

Kabata-Pendias, A., & Pendias, H. (2011). *Trace Elements in Soils and Plants*. CRC Press, Inc.

Keon, N. E., Swartz, C. H., Brabander, D. J., Harvey, C., & Hemond, H. F. (2001). Validation of an arsenic sequential extraction method for evaluating mobility in sediments. *Environmental Science and Technology*, *35*(13), 2778–2784. https://doi.org/10.1021/es001511o

Kierczak, J., Pedziwiatr, A., Waroszewski, J., & Modelska, M. (2016). Mobility of Ni, Cr and Co in serpentine soils derived on various ultrabasic bedrocks under temperate climate. *Geoderma*, *268*, 78–91. https://doi.org/10.1016/j.geoderma.2016.01.025

Kumamoto, K. M., Warren, J. M., & Hauri, E. H. (2019). Evolution of the Josephine Peridotite Shear Zones: 1. Compositional Variation and Shear Initiation. *Geochemistry, Geophysics, Geosystems*, *20*(12), 5765–5785. https://doi.org/10.1029/2019GC008399

Kumar, A., & Maiti, S. K. (2013). Availability of Chromium, Nickel and Other Associated Heavy Metals of Ultramafic and Serpentine Soil /Rock and in Plants. *International Journal of Emerging Technology and Advanced Engineering Website: Www.Ijetae.Com ISO Certified Journal*, *3*(2), 256–268. http://citeseerx.ist.psu.edu/viewdoc/download?doi=10.1.1.413.6755&rep=rep1&type=pdf

Lopez, A. M., Pacheco, J. L., & Fendorf, S. (2023). Metal toxin threat in wildland fires determined by geology and fire severity. *Nature Communications*, *14*(1). https://doi.org/10.1038/s41467-023-43101-9

Magliozzi, L. J., Matiasek, S. J., Alpers, C. N., Korak, J. A., McKnight, D., Foster, A. L., Ryan, J. N., Roth, D. A., Ku, P., Tsui, M. T.-K., Chow, A. T., & Webster, J. P. (2024). Wildland–urban interface wildfire increases metal contributions to stormwater runoff in Paradise, California. *Environmental Science: Processes & Impacts*, *26*(4), 667–685. https://doi.org/10.1039/D3EM00298E

Mandal, A., & Sengupta, D. (2006). An assessment of soil contamination due to heavy metals around a coal-fired thermal power plant in India. *Environmental Earth Sciences*, *51*(3), 409–420.

Mehra, O. P., & Jackson, M. L. (1958). Iron Oxide Removal from Soils and Clays by a Dithionite-Citrate System Buffered with Sodium Bicarbonate. *Clays and Clay Minerals*, *7*(1), 317–327. https://doi.org/10.1346/ccmn.1958.0070122

Morrison, J. M., Goldhaber, M. B., Mills, C. T., Breit, G. N., Hooper, R. L., Holloway, J. A. M., Diehl, S. F., & Ranville, J. F. (2015). Weathering and transport of chromium and nickel from serpentinite in the Coast Range ophiolite to the Sacramento Valley, California, USA. *Applied Geochemistry*, *61*, 72–86. https://doi.org/10.1016/j.apgeochem.2015.05.018

Norouzi, M., & Ramezanpour, H. (2013). Effect of Fire on Chemical Forms of Iron and Manganese in Forest Soils of Iran. *Environmental Forensics*, *14*(2), 169–177. https://doi.org/10.1080/15275922.2013.781077

Oze, C. (2003). Chromium Geochemistry of Serpentinites and Serpentine Soils. In *Department of Geological & Environmental Sciences, Stanford University: Vol. Dissertati* (Issue August). https://doi.org/10.16309/j.cnki.issn.1007-1776.2003.03.004

Oze, C., Fendorf, S., Bird, D. K., & Coleman, R. G. (2004). Chromium geochemistry in serpentinized ultramafic rocks and serpentine soils from the Franciscan complex of California. *American Journal of Science*, *304*(1), 67–101. https://doi.org/10.2475/ajs.304.1.67

Panichev, N., Mabasa, W., Ngobeni, P., Mandiwana, K., & Panicheva, S. (2008). The oxidation of Cr(III) to Cr(VI) in the environment by atmospheric oxygen during the bush fires. *Journal of Hazardous Materials*, *153*(3), 937–941. https://doi.org/10.1016/j.jhazmat.2007.09.044

Plumlee, G. S., Martin, D. A., Hoefen, T., Kokaly, R., Hageman, P., Eckberg, A., Meeker, G. P., Adams, M., Anthony, M., & Lamothe, P. J. (2007). *Preliminary Analytical Results for Ash and Burned Soils from the October 2007 Southern California Wildfires*. http://www.usgs.gov/pubprod

Quantin, C., Ettler, V., Garnier, J., & Šebek, O. (2008). Sources and extractibility of chromium and nickel in soil profiles developed on Czech serpentinites. *Comptes Rendus - Geoscience*, *340*(12), 872–882. https://doi.org/10.1016/j.crte.2008.07.013

Rajapaksha, A. U., Vithanage, M., Oze, C., Bandara, W. M. A. T., & Weerasooriya, R. (2012). Nickel and manganese release in serpentine soil from the Ussangoda Ultramafic Complex, Sri Lanka. *Geoderma*, *189–190*, 1–9. https://doi.org/10.1016/j.geoderma.2012.04.019

Roshan, A., & Biswas, A. (2023). Fire-induced geochemical changes in soil: Implication for the element cycling. In *Science of the Total Environment* (Vol. 868). Elsevier B.V. https://doi.org/10.1016/j.scitotenv.2023.161714

Sandeep, S., Ninu, J. M., & Sreejith, K. A. (2019). Mineralogical transformations under fire in the montane grassland systems of the southern Western Ghats, India. *Current Science*, *116*(6), 966–971. https://doi.org/10.18520/cs/v116/i6/966-971

Schlesinger, W. H., Klein, E. M., & Vengosh, A. (2017). Global biogeochemical cycle of vanadium. *Proceedings of the National Academy of Sciences of the United States of America*, *114*(52), E11092–E11100. https://doi.org/10.1073/pnas.1715500114

Stankov Jovanovic, V. P., Ilic, M. D., Markovic, M. S., Mitic, V. D., Nikolic Mandic, S. D., & Stojanovic, G. S. (2011). Wild fire impact on copper, zinc, lead and cadmium distribution in soil and relation with abundance in selected plants of Lamiaceae family from Vidlic Mountain (Serbia). *Chemosphere*, *84*(11), 1584–1591. https://doi.org/10.1016/j.chemosphere.2011.05.048

Stein, E., Brown, J., Hogue, T., Burke, M., & Kinoshita, A. (2012). Stormwater contaminant loading following southern California wildfires. *Environ Toxicol Chem.*, *31*(11), 2625–2638.

Williams, A. P., Abatzoglou, J. T., Gershunov, A., Guzman-Morales, J., Bishop, D. A., Balch, J. K., & Lettenmaier, D. P. (2019). Observed Impacts of Anthropogenic Climate Change on Wildfire in California. *Earth's Future*, *7*(8), 892–910. https://doi.org/10.1029/2019ef001210

Ziwa, G., Crane, R., & Hudson-Edwards, K. A. (2020). *minerals Geochemistry, Mineralogy and Microbiology of Cobalt in Mining-Affected Environments*. https://doi.org/10.3390/min

CHAPTER V: DISSERTATION CONCLUSION

The spatial and temporal heterogeneity of weathering complicates projections of contaminant cycling onto our understanding of water and soil resource sustainability. A significant challenge is upscaling molecular scale variations onto a landscape due to spatial and temporal scales. These complexities across a landscape pose challenges for making predictions and managing environmental contaminant reactivity. Much work has been directed toward understanding: what drives contaminant reactivity across a landscape? How do these variations influence the generation and transport of contaminants? However, our mechanistic understanding of the landscape controls that govern contaminant fate and transport still needs to be clarified in order to safeguard soil and water resources. Furthermore, wildfires have recently been shown to influence contaminant cycling in soils, and the distribution of geogenic contaminants that can be mobilized by fire is linked to weathering. Therefore, my dissertation aimed to understand the influence of soil weathering on contaminant reactivity and then assess how weathering products and landscape positions influence the generation and transport of contaminants under different burn intensities. The objectives of this dissertation were to 1) gain an understanding of how soil weathering governs contaminant fate in the environment; 2) understand how fire and landscape position drives the generation and availability of Cr; and 3) determine how multiple contaminants (Co, Mn, Ni, and V) are impacted and transported from burned soils across a landscape.

In Chapter II, we explored how soil minerals that govern contaminant fate are influenced by soil weathering across an Oregon chronosequence. More specifically, we employed As sorption experiments on different aged soils as a proxy for contaminant reactivity. Our initial hypothesis was that increased soil weathering, which generates the preponderance of secondary crystalline minerals in soils, would have the greatest influence on As sorption. My hypothesis was incorrect, and data revealed that amorphous phases driven by soil weathering had the greatest affinity for and control on As sorption. Chemical extractions revealed that amorphous (oxy)hydroxides were the dominant mineral phases governing As sorption, even in the presence of abundant crystalline oxides. Micro-X-ray fluorescence (μ-XRF) spectroscopy revealed a strong spatial correlation between As and Fe in reacted soils. The data collected allowed for the determination of pedogenic controls maintained by weathering on the fate of contaminants.

Future directions for this work include expanding this understanding to different environmental factors, such as lithologic and climatic differences, that likely influence soil weathering and subsequently impact contaminant reactivity across a landscape.

Chapter III investigates how soil weathering across a serpentine hillslope influences the degree of contaminants found throughout a landscape that can be subsequently mobilized by fire. This chapter focused on flame-induced Cr(VI) generation and quantified the Cr-associated mineral transformations with burn intensity across a hillslope. I hypothesized that summit soils would generate the most Cr(VI) from flame induction due to higher concentrations of Cr released into soil due to in-situ weathering of Cr-rich parent materials. Results from Cr(VI) chemical extractions revealed that summit soils from the 400 ºC and 600 ºC treatments generated highly exchangeable Cr(VI) before transforming and being included into new minerals at 800 ºC. Micro-X-ray fluorescence (μ-XRF) analyses of burned soils revealed that Cr(VI) was generated around chromite (Cr(III)-rich particles) and was detected throughout the mineral matrix. Chemical extractions and synchrotron X-ray diffraction exposed that Cr-reactive minerals and Fe(oxy)hydroxides were generated and subsequently transformed into new crystalline minerals with increased burn intensity, which varied across the hillslope due to weathering's control on Fe-mineral phases. Lastly, soil transport experiments revealed that regardless of hillslope position, Cr(VI) was leached from burned soils at concentrations that exceed drinking water standards, indicating a potential threat to human health and the environment, and the degree of Cr(VI) transported from burned soils was greatest from the summit soils. These results quantify the potential risk fire can pose to water and soil quality across a landscape and observe contaminant reactive minerals transformed by fire. Further research should focus on field observations and post-fire monitoring across a landscape to develop better predictions and restoration efforts to decrease contaminants released and mobilized by fire.

Chapter IV expands our understanding of soil weathering and fire-induced contaminant reactivity across a landscape to other geogenic contaminants found within serpentine soils (Co, Mn, Ni, and V). After establishing that soil weathering is critical in determining the fate of contaminants and fire-induced transformations, we anticipated analogous outcomes with burn intensity and hillslope position for Co, Mn, Ni, and V, as observed in Chapter 3. Our data reveal that Co, Mn, and Ni and their dominant-host phases transformed towards more crystalline phases with burn intensity. Furthermore, transport experiments highlight that hazardous concentrations

of Ni and Mn could be released and transported from burned soils and that the degree of contamination depends on hillslope position. These findings partially support our hypothesis that summit soils generated the greatest concentrations of contaminants; however, all burned soils across the hillslope could threaten soil and water quality, specifically due to Mn and Ni efflux. This work aids in comprehending the intricate dynamics of soil weathering on contaminant distributions along a hillslope and how fire can lead to subsequent influences on soil and water quality that persist well beyond the fire period.

Previous work has contributed to our mechanistic understanding of how soil weathering drives soil and water contamination. However, many unknowns remain due to heterogeneity at various scales, particularly regarding wildfire-induced transformation. There are several significant findings of this dissertation, (1) amorphous phases driven by the stage of soil weathering influence contaminant reactivity across a landscape; (2) soil weathering and burn intensity across a landscape influence the generation and availability of Cr(VI); and (3) burned soils can release Cr(VI), Mn, and Ni at concentrations that exceed drinking water standards for over a year post-fire, depending on hillslope position. These contributions to understanding environmental contaminant fate are essential, particularly in post-fire systems. Since wildfires are increasing in burned area, intensity, and reoccurrence, it is critical to understand the landscape controls that govern contaminant fate in the environment.